

Dissertation  
submitted to the  
Combined Faculties for the Natural Sciences and for Mathematics  
of the Ruperto-Carola University of Heidelberg, Germany  
for the degree of  
Doctor of Natural Sciences

presented by  
Diplom-Physiker Marc R. Stockmeier  
born in Ludwigshafen am Rhein

Oral examination: 11th July, 2002



# Pion Production in Relativistic Heavy Ion Collisions

Referees: Prof. Dr. Norbert Herrmann  
Prof. Dr. Johanna Stachel



Für  
Lea, Jan  
und  
Silke



## Pion Production in Relativistic Heavy Ion Collisions

In this thesis, a systematic study of the pion production of various colliding systems ( $Ca + Ca$ ,  $Ru + Ru$ ,  $Zr + Zr$ , and  $Au + Au$ ) at three different incident energies (400, 1000, and 1500 AMeV) is presented. The experiments were performed with the **FOPI** detector located at the Schwerionen Synchrotron (SIS) at the Gesellschaft für Schwerionenforschung (GSI), Darmstadt. The pion production is studied in terms of the mean number of pions  $\langle n_\pi \rangle$  per mean number of participants  $\langle A_{part} \rangle$ . This quantity is deduced by counting charged pions that are identified with the Central Drift Chamber (CDC) and determining the number of participating nucleons with different charged particle multiplicity spectra. The detector response is studied with a detailed Monte Carlo simulation. A correction is deduced from these detector simulation using an iQMD event generator. The pion production spans from  $\frac{\langle n_\pi \rangle}{\langle A_{part} \rangle} = 1.5 \cdot 10^{-2}$  to  $3.5 \cdot 10^{-1}$  depending on the colliding system and the incident energy. A pion suppression on the order of 35% is observed for all energies with increasing system mass. The charged pion ratio  $R_\pi = \frac{n_{\pi^-}}{n_{\pi^+}}$  is found to be sensitive to the initial isospin ratio  $\frac{N}{Z}$  but not to the system mass and covers values from 1.0 to 2.25. The experimental results are compared to different theoretical models. The transport models describe the data reasonable. The temperature and the baryo-chemical potential are deduced from a thermal model. The upgrade program for this experimental device concerning the data acquisition is described in the first part of this thesis.

## Pionenproduktion in relativistischen Schwerionenkollisionen

In der vorliegenden Arbeit wird die Pionenproduktion verschiedener Systeme ( $Ca + Ca$ ,  $Ru + Ru$ ,  $Zr + Zr$  und  $Au + Au$ ) bei drei verschiedenen Strahlenergien (400, 1000 und 1500 AMeV) untersucht. Die Experimente wurden mit dem **FOPI** Detektor am Schwerionen Synchrotron (SIS) der Gesellschaft für Schwerionenforschung (GSI) in Darmstadt durchgeführt. Die Pionenproduktion wird durch die mittlere Zahl der Pionen  $\langle n_\pi \rangle$  pro mittlerer Zahl der teilnehmenden Nukleonen  $\langle A_{part} \rangle$  beschrieben. Diese Größe wird durch Zählen der in der Zentralen Driftkammer (CDC) identifizierten Pionen und Bestimmung der partizipierenden Nukleonen durch verschiedene Multiplizitätsspektren ermittelt. Mit Hilfe von detaillierten Monte-Carlo-Simulationen wird die Detektorantwort untersucht. Basierend auf der Detektorsimulation mit iQMD-Ereignissen werden Korrekturen eingeführt. Die Pionenproduktion reicht abhängig vom betrachteten System und der Strahlenergie von  $\frac{\langle n_\pi \rangle}{\langle A_{part} \rangle} = 1,5 \cdot 10^{-2}$  bis  $3,5 \cdot 10^{-1}$ . Mit steigender Systemmasse wird bei allen Strahlenergien eine Unterdrückung der Pionenproduktion um etwa 35% beobachtet. Das Verhältnis der geladenen Pionen  $R_\pi = \frac{n_{\pi^-}}{n_{\pi^+}}$ , das von 1,0 bis 2,25 reicht, ist dagegen nur vom Isospinverhältnis  $\frac{N}{Z}$ , jedoch nicht von der Systemmasse abhängig. Die experimentellen Daten werden mit verschiedenen theoretischen Modellen verglichen. Die Transportmodelle beschreiben die experimentellen Daten zufriedenstellend. Ein thermisches Modell wird zur Bestimmung der Temperatur und des baryo-chemischen Potentials verwendet. Das Upgrade-Programm bezüglich des Datenaufnahmesystems wird im ersten Teil dieser Arbeit behandelt.



---

# Contents

<b>1</b>	<b>Introduction</b>	<b>1</b>
1.1	Global Features of Heavy Ion Collisions . . . . .	2
1.2	Pion Production in Heavy Ion Reactions . . . . .	4
1.3	Experimental Data . . . . .	6
<b>2</b>	<b>The FOPI-Detector</b>	<b>9</b>
2.1	<b>FOPI</b> - A Detector for Charged Particles . . . . .	9
2.2	The Central Drift-Chamber CDC . . . . .	14
2.3	Beam Detectors and Target . . . . .	16
<b>3</b>	<b>The FOPI-Upgrade Program</b>	<b>19</b>
3.1	The Data Acquisition System . . . . .	19
3.2	Readout of the Drift Chambers . . . . .	20
3.2.1	The Scanning Sampling Module . . . . .	21
3.2.2	The SAM and Data Reduction . . . . .	23
3.2.3	VME Data Transfer Test . . . . .	25
3.3	Status of the Readout Project . . . . .	27
3.4	A Second Level Trigger . . . . .	27
3.5	Changes and Future Enhancements of <b>FOPI</b> . . . . .	31
<b>4</b>	<b>Analysis of Experimental Data</b>	<b>33</b>
4.1	The Experiments . . . . .	33
4.2	Event Selection . . . . .	34
4.3	Background Determination . . . . .	36
4.4	Determination of the Impact Parameter $b$ . . . . .	36
4.5	Determination of $A_{part}$ . . . . .	39
4.6	Multiplicity Spectra . . . . .	39
4.7	Pion Identification . . . . .	43
4.7.1	Distance to Vertex . . . . .	44
4.8	Pion Acceptance and Pion Counting . . . . .	49
4.8.1	Pion Background . . . . .	51

---

4.9	Pion Efficiency, Corrections . . . . .	53
4.9.1	Monte Carlo Simulation of the Detector . . . . .	53
4.9.2	Global Correction Function with Respect to $A_{part}$ . . . . .	56
4.9.3	Correction Function According to Multiplicity . . . . .	61
4.10	Different Treatment of Zr . . . . .	66
4.11	Pion Yield Determination . . . . .	67
4.12	Error Estimations . . . . .	67
<b>5</b>	<b>Experimental Results</b>	<b>71</b>
5.1	The Total Pion Yield . . . . .	71
5.2	Pion Ratios . . . . .	73
5.3	Comparison with Experiments . . . . .	76
5.4	Comparison to <b>FOPI</b> Data . . . . .	77
5.4.1	Interpretation of $m_{\perp}$ -Spectra . . . . .	79
<b>6</b>	<b>Comparison to Theory</b>	<b>81</b>
6.1	The Thermal Model . . . . .	81
6.2	The iQMD Model . . . . .	85
6.2.1	iQMD and Pions . . . . .	86
6.3	The BUU Model . . . . .	91
6.4	Different BUU Realisations . . . . .	91
6.5	The BEM Model . . . . .	92
<b>7</b>	<b>Conclusion and Outlook</b>	<b>95</b>
<b>A</b>	<b>Isospin Considerations</b>	<b>97</b>
<b>B</b>	<b>Experiments</b>	<b>99</b>
<b>C</b>	<b><math>d_0</math> Fit-Parameters</b>	<b>101</b>
<b>D</b>	<b>Pion Production</b>	<b>105</b>

# List of Figures

1.1	A sketch of a heavy ion collision at intermediate energies . . . . .	3
1.2	A sketch of the EOS of nuclear matter . . . . .	5
1.3	Pion production at 1.0 AGeV . . . . .	7
2.1	The <b>FOPI</b> -Detector setup . . . . .	10
2.2	CDC event display . . . . .	13
2.3	The phase-space coverage of <b>FOPI</b> . . . . .	14
2.4	Schematic view of a CDC sector . . . . .	15
2.5	Sketch of the beam detector system . . . . .	16
3.1	Scheme of a drift-chamber hit . . . . .	22
3.2	FADC dump and SSM hitlet . . . . .	23
3.3	SAM3 technical sketch . . . . .	24
3.4	Heidelberg DAQ test system . . . . .	26
3.5	The future DAQ-System of the <b>FOPI</b> -detector . . . . .	28
3.6	Two dimensional matrix: momentum $p$ versus velocity $v$ . . . . .	29
3.7	CDC event display with noise . . . . .	30
4.1	Vertex distribution . . . . .	35
4.2	Reaction geometry of two colliding nuclei . . . . .	37
4.3	Integration of multiplicity spectrum . . . . .	38
4.4	The number of participating nucleons $A_{part}$ as a function of impact parameter $b$ . . . . .	40
4.5	Charged particle multiplicity distributions . . . . .	41
4.6	Correlation between multiplicity and $A_{part}$ . . . . .	42
4.7	$\langle dE/dx \rangle$ as a function of momentum over charge $\frac{p}{q}$ . . . . .	43
4.8	Mass distribution of the CDC . . . . .	44
4.9	Definition of the $d0$ parameter . . . . .	45
4.10	Distance to vertex distribution . . . . .	46
4.11	Distance to vertex $d0$ for $\pi^-$ mesons as a function of $p_{\perp}$ . . . . .	47
4.12	Acceptance of the CDC for pions . . . . .	50
4.13	Pion multiplicity as a function of $m_{cbp}$ . . . . .	51

---

4.14	Pion multiplicity as a function of different particle multiplicity observables . . . . .	52
4.15	Hit distribution of different particle track . . . . .	55
4.16	Determination of the corrections according to $A_{part}$ . . . . .	57
4.17	Consistency check of the determined functional dependence of the considered corrections on $A_{part}$ . . . . .	58
4.18	Corrected pion multiplicity spectra according to the direct $A_{part}$ correction . . . . .	59
4.19	1, 3, 5 $\sigma$ -cut detected pion pion multiplicities . . . . .	60
4.20	Determination of the correction according to multiplicity . . . . .	63
4.21	Determination of the correction according to multiplicity . . . . .	65
4.22	CDC track multiplicity versus PLAWA multiplicity . . . . .	66
5.1	Pion production . . . . .	72
5.2	Pion production excitation function . . . . .	73
5.3	Pion ratios . . . . .	74
5.4	Charged pion ratios versus the initial isospin ratios . . . . .	76
5.5	Pion production at 1 AGeV . . . . .	77
5.6	Comparison to <b>FOPI</b> -data . . . . .	78
5.7	$p_{\perp}$ distribution of the $\pi^{-}$ meson . . . . .	80
6.1	Pion ratios as a function of temperature . . . . .	83
6.2	Pion yields determined from the thermal model . . . . .	84
6.3	Elementary reaction cross section used in iQMD . . . . .	88
6.4	Comparison to the iQMD Model . . . . .	89
6.5	Pion ratios compared to the iQMD model . . . . .	90
6.6	BUU Calculations by P. Danielewicz . . . . .	93
A.1	Clebsch-Gordan coefficients . . . . .	98

# List of Tables

2.1	The polar angular coverage of the <b>FOPI</b> sub-detectors. . . . .	12
4.1	Experimental conditions . . . . .	34
4.2	Distance to vertex parameter $Au + Au$ @ 1.0 AGeV . . . . .	48
4.3	Variation of the slopes . . . . .	68
4.4	Reconstruction errors within the GEANT analysis . . . . .	69
5.1	Pion ratios, predictions from the isobar model . . . . .	75
5.2	Pion ratios from the isobar model ( $I_3 = \frac{1}{2}$ ) . . . . .	75
6.1	Extracted baryo-chemical potentials . . . . .	83
6.2	Extracted Temperatures . . . . .	85
6.3	Radii and geometrical cross sections, $\sigma_{geo}$ , for the simulated reactions. . . . .	86
B.1	Summary of analysed dst generations and run numbers. . . . .	99
B.2	Available events per experiment for the $MB + BARREL$ trigger. . .	100
C.1	d0 parameters used for the d2v cut definition Au+Au. . . . .	101
C.2	d0 parameters used for the d2v cut definition Ru+Ru. . . . .	102
C.3	d0 parameters used for the d2v cut definition Zr+Zr. . . . .	102
C.4	d0 parameters used for the d2v cut definition Ca+Ca. . . . .	103
D.1	Pion production per $A_{part}$ of the reaction $Au + Au$ . . . . .	106
D.2	Pion production per $A_{part}$ of the reaction $Ru + Ru$ . . . . .	107
D.3	Pion production per $A_{part}$ of the reaction $Zr + Zr$ . . . . .	108
D.4	Pion production per $A_{part}$ of the reaction $Ca + Ca$ . . . . .	109



# Chapter 1

## Introduction

In comparing the theory outlined in this paper with the experimental results, it has been supposed that the atom consists of a central charge supposed concentrated at a point, and that the large deflexions of the  $a$  and  $b$  particle are mainly due to their passage through the strong central field. [Rutherford, 1911]

It is that central charge, mentioned in the motto, and nowadays identified with the nucleus, that is the field of interest of nuclear physics. Since its discovery, the properties of nuclear matter in general are under continuous investigations. The finite nuclei are studied in great detail with different experimental techniques, like low energy scattering experiments with  $\alpha$  particles or electron scattering devoted to determination of the charge distribution of a nucleus or  $\gamma$  spectroscopy studies concerned with the shell structure of the nucleus. The ongoing investigations lead, among others, to the liquid drop model [von Weizsäcker, 1935] and to the nuclear shell model, which celebrated its 50 anniversary in Heidelberg [Hüfner and Weidenmüller, 1999] two years ago.

Answers to the question of the properties of compressed nuclear matter became accessible with the development of accelerators with energies beyond the threshold energies for the production of new particles, and the capability to accelerate Heavy Ions (HI), which enable the creation of large volumes of hot and dense nuclear matter. With increasing incident beam energy, new phenomena can be observed, e.g., the production of particles not present in the entrance channel or the collective properties of the reaction products.

Densities reached in the collision of two heavy nuclei are considered to be close to those present in the interior of stellar objects, like neutron stars. Therefore, HI reactions are a unique tool to create and study hot and dense nuclear matter in the laboratory.

The concept of an equation of state (EOS) [Stöcker and Greiner, 1986] intro-

duces the thermodynamic relations of pressure, temperature and density to infinitely expanded nuclear matter. The extraction of the EOS of nuclear matter from HI collisions is one pending problem of HI physics at intermediate energies. First experiments to derive the EOS, discussed later in this chapter, were trying to connect directly the pion production with the EOS. The pion production is also the subject of this thesis.

Like 1911 the experimental data have to be compared to theoretical predictions and explanations, especially in a many particle system that represents a collision of two nuclei. The properties of the nuclear matter are not observed directly in experiments, but have to be inferred from the measurements by means of comparison with theoretical model predictions. This is a consequence of the fact that in HI collisions one is confronted with a limited number of particles (finite size effect) which interact in a limited time interval (finite time effect).

## 1.1 Global Features of Heavy Ion Collisions

Heavy ion reactions at energies above 100 A MeV can be described in terms of the so called participant spectator model [Nagamiya et al., 1981]. At this energy the de Broglie wavelength,  $\lambda = \frac{\hbar}{p}$ , is in the order of the mean distance of two nucleons ( $d = 1.8$  fm). This implies that the projectile nucleons "see" only the nucleons, if they are located in the geometrical overlap region of the two colliding nuclei, and do not probe the nucleus as a single object. That means that only the nucleons in the overlap region react with each other. The number of nucleons participating in the reaction,  $A_{part}$ , is not directly measurable. The extraction of this quantity is described later. The collision is dominated by nucleon-nucleon scattering due to the small de Broglie wavelength. The presence of all other nucleons can be summed into the mean field. Figure 1.1 illustrates this behaviour. The overlap region, which rests in the centre of mass system, is called fireball. This fireball is the object of interest. In the overlap region the nuclear matter will be compressed and heated. The kinetic energy from the entrance channel is dissipated by subsequent Nucleus-Nucleus collisions ( $NN$ -collisions). Besides heating the system by increasing the random motion of the constituents, part of the energy can be stored in the mean field of the dense system. The compressional energy can be transferred to collective motion; in this context, a number of ejectiles exhibit a common property (e.g. the emission of many particles of the same kind or the emission of many ejectiles with a common velocity field or into a common direction) [Herrmann et al., 1999]. Collective motion, e.g, flow in its various characteristics are studied in great detail. The different flow phenomena are investigated at

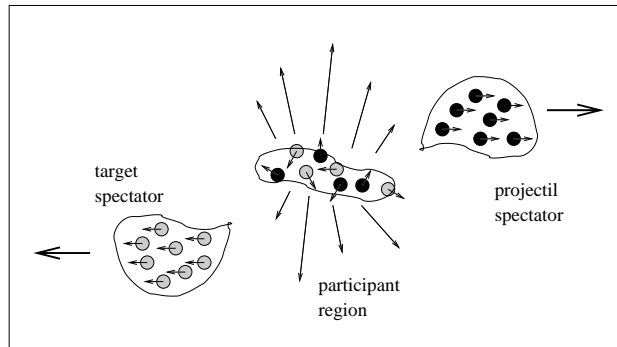


**Figure 1.1:** A sketch of a heavy ion collision at intermediate energies. The hot and dense nuclear matter, the fireball is created by the nucleons in the overlap region. Nucleons which do not participate in the reaction are called spectators.

energies from the BEVALAC to SPS<sup>1</sup> in the reviews [Reisdorf and Ritter, 1997] and [Herrmann et al., 1999]. The radial flow characterises the motion of particles in a spherical velocity field. Longitudinal and transverse flow (i.e., along the incoming beam and in the plane perpendicular to the beam axis, respectively) are observed in HI reactions as well.

Production of particles from  $NN$ -collisions probes the thermal distribution and thus the temperature. The channel with the lowest threshold is the production of pions – the lightest mesons. For a review of the particle production at SIS energies refer to [Senger and Stroebele, 1999].

The question of pion production will be the main subject of this thesis.

The production of strangeness at energies below and at the production threshold of kaons became a very hot topic over the last years. Density-dependent in-medium changes of the mass of the  $K$ -meson are discussed. All theoretical predictions agree that the  $K^+$  meson mass rises slightly with increasing density whereas the  $K^-$  meson mass drops drastically (at  $\rho/\rho_0 = 3.0$  the mass-drop is about 50%  $m_{3\rho_0}^{K^-} = 0.5 * m_0^{K^-}$ ) [Schaffner et al., 1997].

For negatively charged pions a mass change in the nuclear medium is observed experimentally [Gillitzer, 2001]. A deuteron beam of about 600MeV is used to initiate the transfer reaction  $^{206}\text{Pb}(d, ^3\text{He})$  to create pionic atoms. The  $(1s)_\pi$  state is used to conclude a mass drop of 26MeV for the  $\pi^-$  in the Lead nucleus [Geissel et al., 2000]. This measurement is of course performed at  $\rho/\rho_0 = 1$ . A density dependent change of the pion mass is till now not observed.

In [Wiśniewski et al., 2000], measurements of the  $K^-$  to  $K^+$  ratio performed with the **FOPI**-detector are reported, and found to be rather high in terms of the

<sup>1</sup>The energy ranges named by the accelerator which provides the HI-beam.

expected ratio. The data are explained by RBUU<sup>2</sup> calculations which have included the in-medium modifications of the kaons in a linear dependence of kaon mass with the baryon density [Cassing et al., 1997]. The KaoS collaboration finds the same observation [Laue et al., 1999].

However, there are a number of problems remaining, that are not solved yet. A source of uncertainty for the  $K^-$  yield is the possible underestimation of the strangeness exchange reaction  $\Lambda + \pi \rightarrow N + K^-$ . In some of the transport model calculations, this production channel of kaons amounts to about 10% of the total production cross section [Cassing and Bratkovskaya, 1999]. On the other hand, in the framework of iQMD it was found that almost all  $K^-$  are produced by the pionic channel  $\Lambda + \pi \rightarrow N + K^-$  [Hartnack et al., 2001]. This strong variation from one model to another has to be investigated in future. In the determination of this production channel a precise knowledge of pion yield is necessary. As a prerequisite for the final conclusion of the strangeness production mechanism the theoretical models must be able to describe the production of pions quantitatively. This leads to the central theme of this thesis, too.

## 1.2 Pion Production in Heavy Ion Reactions

Pions with masses  $m_{\pi^\pm} = 139.57\text{MeV}$  and  $m_{\pi^0} = 134.98\text{MeV}$ <sup>3</sup> are the lightest particles produced in HI collisions. The threshold energy for pion production in a  $NN$ -collision is  $290\text{MeV}$  ( $280\text{MeV}$ ) for charged pions (neutral pions) in laboratory energy [Braun-Munzinger and Stachel, 1987]. All reactions investigated in this work are above the  $NN$  pion production threshold. Therefore, pions are the most abundant produced particle. Pions subthreshold production is seen even at energies of  $35\text{A MeV}$  in the reactions  $^{14}\text{N} + \text{Al}, \text{Ni}, \text{W} \rightarrow \pi^0 + X$  [Braun-Munzinger et al., 1984]. A two step process is necessary to create a pion. In a  $NN$ -collision a  $\Delta$ -resonance is created and decays later on to produce a pion:  $NN \rightarrow N\Delta \rightarrow NN\pi$ . The  $\Delta$ -resonance may be described as a  $NN\pi$  p-wave state.

Pion multiplicity measurements at the BEVALAC were used to derive information on the nuclear matter equation of state [Harris et al., 1985], [Stock, 1986]. The basic idea is to use the pions as a thermometer and the incident energy as a measure of the pressure. Figure 1.2 shows the internal energy per baryon of nuclear matter as a function of normalised density  $\rho/\rho_0$ .  $\rho_0$  denotes the ground state density of  $0.16\text{nucleons}/\text{fm}^3$ . This function,  $W(\rho/\rho_0, T = 0)$ , is commonly referred to as the EOS. The thermodynamical relation between pressure and density which is normally called equation of state is given by the derivative of  $W$

<sup>2</sup>The BUU model is described briefly in chapter 5. “R” stands for relativistic.

<sup>3</sup> [Groom et al., 2000]

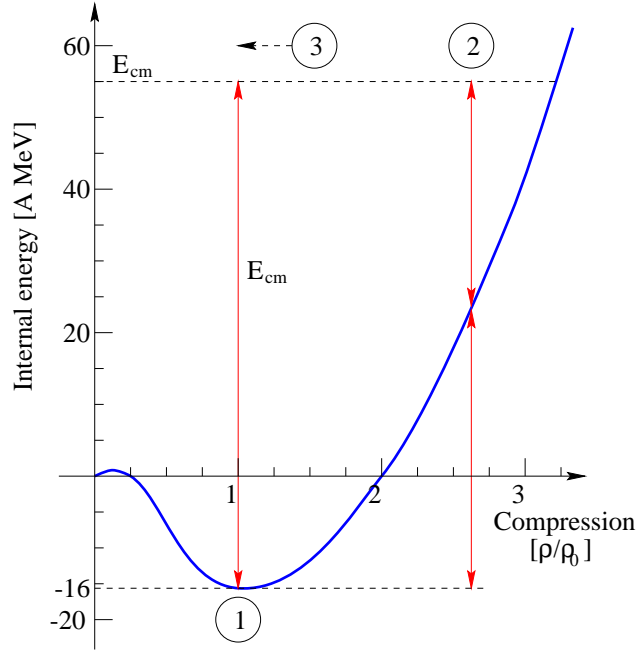


**Figure 1.2:** A sketch of the EOS of nuclear matter. The internal energy is related to the density of the nuclear matter. ①, ②, and ③ indicate different stages in a HI reaction. (Explanation see text.)

with respect to  $\rho$ . During a HI collision the different stages of energy and density of the system, ① - ③, are reached. The ground state, in figure 1.2 referred to by ①, is the starting point of the collision. Stage ② denotes the point of the maximum compression. At this point the total energy is shared between thermal and compressional energy. At stage ③ the expansion towards freeze out takes place. According to Cascade model calculations, the  $\langle \pi + \Delta \rangle$  abundances do not change after reaching the high compression phase of the reaction. The Cascade model treats a HI collision as independent free  $NN$ -collisions. With this in mind the conclusion is given in [Stock, 1986] that the number of pions<sup>4</sup> is a primordial observable of the high compression phase. The density reached in the collision is calculated using the relativistic Hugoniot-Rankine shock compression model:

$$\rho/\rho_0 = \gamma_{cm} \left[ 1 - \frac{\rho_0 E^{Lab}}{2P} \right]^{-1} \quad (1.1)$$

with  $\gamma_{cm}$  the Lorentz factor,  $E^{Lab}$  the energy of the projectile and  $P$  the pressure. The pressure,  $P$ , itself is connected to EOS (the function  $W$ ) with the following

<sup>4</sup>The  $\Delta$ s are decaying into pions.

relation:

$$P = \rho^2 \left. \frac{\partial W(\rho, T)}{\partial \rho} \right|_{S=const} \quad (1.2)$$

Thus, after an iterative procedure,  $W(\rho/\rho_0, T = 0)$  can be determined.

The compressional energy in this framework is derived from the difference between the model calculation (cascade) and the data, i.e., the model predicts a higher pion multiplicity than what is seen in the data for a given centre of mass energy  $E_{cm}$ . The amount of energy needed to shift the measured pion multiplicity to the predicted ones is interpreted as being the compression energy.

However, the direct measurement of the EOS as described above turned out to be not correct. New phenomena were found and included to the model descriptions. To determine the pressure, the model used relies on hydrodynamical assumptions that an instantaneous local equilibrium is reached. The derivation of the temperature based on the assumption of thermodynamical equilibrated nuclear matter triggered a general discussion about how the equilibration takes place. The momentum dependence of interaction was not included, which is now consistently introduced to the models.

Nevertheless, the basic idea that pions are connected to the EOS could still be valid. Therefore, it is worth to reexamine the pion production with improved methods and to investigate the connection between pion multiplicities and the nuclear matter EOS with improved model calculations.

### 1.3 Experimental Data

The available experimental data on the pion production in HI collisions at an incident energy of 1 AGeV are collected in figure 1.3. The measured pion yields are shown in terms of the mean number of pions per mean number of participants,  $\frac{\langle n_\pi \rangle}{\langle A_{part} \rangle}$ . That the pion production is reduce-able to a single number was shown already with the Streamer Chamber [Harris et al., 1987], [Harris et al., 1985]. In the experiments  $Ar + KCl$  and  $La + La$  it was shown that the number of pions per participant rises linearly. Moreover at all measured energies no difference was observed for these two reactions. The conclusion was drawn that the pion production is independent on the system size and rises with increasing incident energy. This result is commonly referred to as the Harris systematic.

In the case of the results at 1.0 AGeV, different conclusions can be drawn according to figure 1.3, depending which set of the results is considered. As described above, the Harris systematic shows no system size dependence at all. The **FOPI** data shows a linear decrease with rising system-size indicating that there is no saturation of the pion production. Taps results suggest a saturation, while the KaoS data exhibit a drop when the system-size increases. Within the stated

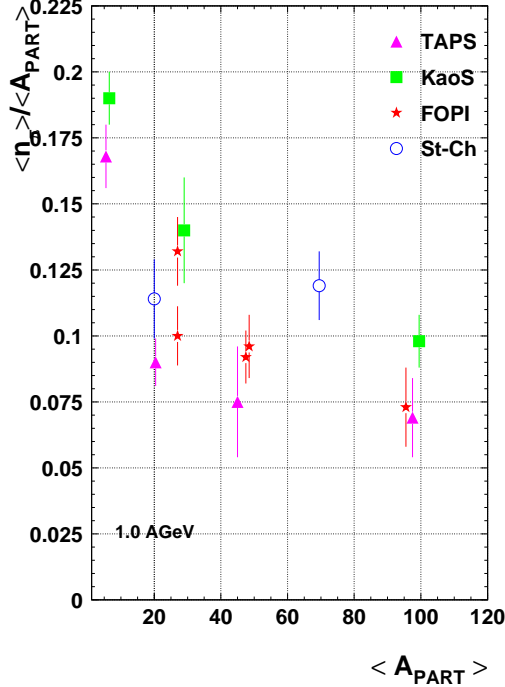


**Figure 1.3:** Pion production at 1.0 AGeV. The Streamer Chamber data are taken from: *Ar + KCl* [Harris et al., 1985], *La + La* [Harris et al., 1987]. **FOPI**-data: *Ni + Ni* [Pelte et al., 1997a], *Au + Au* [Pelte et al., 1997b], *Ru + Ru* [Pelte, 1998]. Taps-data: *C + C* [Averbeck et al., 1997], *Ar + Ca* [Schwalb et al., 1994], [Berg et al., 1994], *Kr + Zr* [Schwalb et al., 1994], [Berg et al., 1994], *Au + Au* [Schwalb et al., 1994], KaoS-data: [Senger and Stroebele, 1999]

error-bars these trends are not in a real contradiction, but a new measurement is needed to resolve the system size dependence. This is important because of the the pion production process. If a thermalization takes place this would suggest that the number of pions per participating nucleon stays constant because of an equilibration in the production and reabsorption process.

It should be mentioned that all data shown in figure 1.3 are extrapolated in somehow different ways. Taps measures only  $\pi^0$  in a limited angular range and adds the unmeasured charged pions yields, while KaoS and FOPI measure charged pions only. KaoS and FOPI differ in the geometrical acceptance and in the method with which pions are identified. The Streamer Chamber measured only  $\pi^-$ . In all cases, the correction due to the unmeasured pion species is calculated using the isobar model (see section 5.1 and reference [Stock, 1986]).

As shown for example in [Eskef et al., 1998] pions originate from the decay of  $\Delta$ s. In this paper the spectral distribution is also extracted from **FOPI** data. This is important since the pions are reabsorbed by nucleons and form another  $\Delta$ . The lifetime of the  $\Delta$  is therefore relevant for the creation and absorption of a pion.

In this thesis, the **FOPI** systematic is completed to all measured incident energies (from 400 AMeV–1500 AMeV). Systematic biases of the analysis are carefully analysed in order to present a consistent set of data. This thesis is organised

as follows. The **FOPI**-device is described briefly in the following chapter. A detailed description can be found in [Ritman, 1995], [Gobbi et al., 1993] and many doctoral and diploma thesis done in the collaboration. An upgrade of the **FOPI**-device on the one hand detector-wise and on the other hand data-acquisition-wise will change the detector. Some of these new developments were part of this thesis and will be described in chapter 3. The readout system of the drift-chambers are changed. The electronic components of these changes will be described there. In addition precursors of future trigger system are discussed. Chapter 4 is principally concerned with the analysis of **FOPI** data with respect to pion analysis, like event identification, pion selection and the introduction of corrections which have to be applied to the data. Chapter 5 collects the pion data extracted from the various experiments. Comparisons to various theoretical approaches are presented in chapter 6. A conclusion and prospect is given in the last chapter 7. In addition a collection of derived parameters is given in an appendix starting at page 99.

## Chapter 2

# The FOPI-Detector

The SchwerIonen Synchrotron (SIS) is a unique accelerator system located at the Gesellschaft für Schwerionenforschung in Darmstadt. It provides Heavy Ion (HI) beams from alpha particles to uranium with energies of about 100 MeV up to 2 GeV per nucleon. One of the detector systems operating on the SIS beam is the **FOPI**-detector of which the functionality and construction is described in the following sections.

### 2.1 FOPI - A Detector for Charged Particles

The **FOPI** detector system is able to detect all charged particles i.e protons, deuterons, tritons, up to Lithium, as well as produced charged particles like pions and kaons. In addition to that it offers the possibility to identify  $\Delta$ -resonances via their charged decay products ( $\pi^{+/-}, p$ ) [Eskef et al., 1998] by means of invariant mass reconstruction, as well as neutral strange particles, in particular  $\Lambda$  ( $p, \pi^-$  (63.9%)),  $K_S^0$  ( $\pi^+, \pi^-$  (68.6%)) [Ritman et al., 1995], [Kutsche, 2000], and even the  $\Phi$  mesons with hidden strangeness  $\Phi$  ( $K^+, K^-$  (49.2%)) [Herrmann, 1997]<sup>1</sup>. Figure 2.1 shows a schematic view of the detector-system. A scale of one meter is given to show the real size of the **FOPI**-system. As usual for fixed-target experiments, the setup is asymmetric in the laboratory frame, with more emphasis put to the forward hemisphere and the near-target regions. In this way, a high polar angular acceptance coverage in the centre of mass frame of the two colliding nuclei is achieved. The detector system is azimuthally symmetric which leads to an almost  $4\pi$  acceptance in the centre of mass frame. Hence the detector is called **FOPI(FOur PI)**.

---

<sup>1</sup>The stated branching ratios are taken from [Groom et al., 2000].

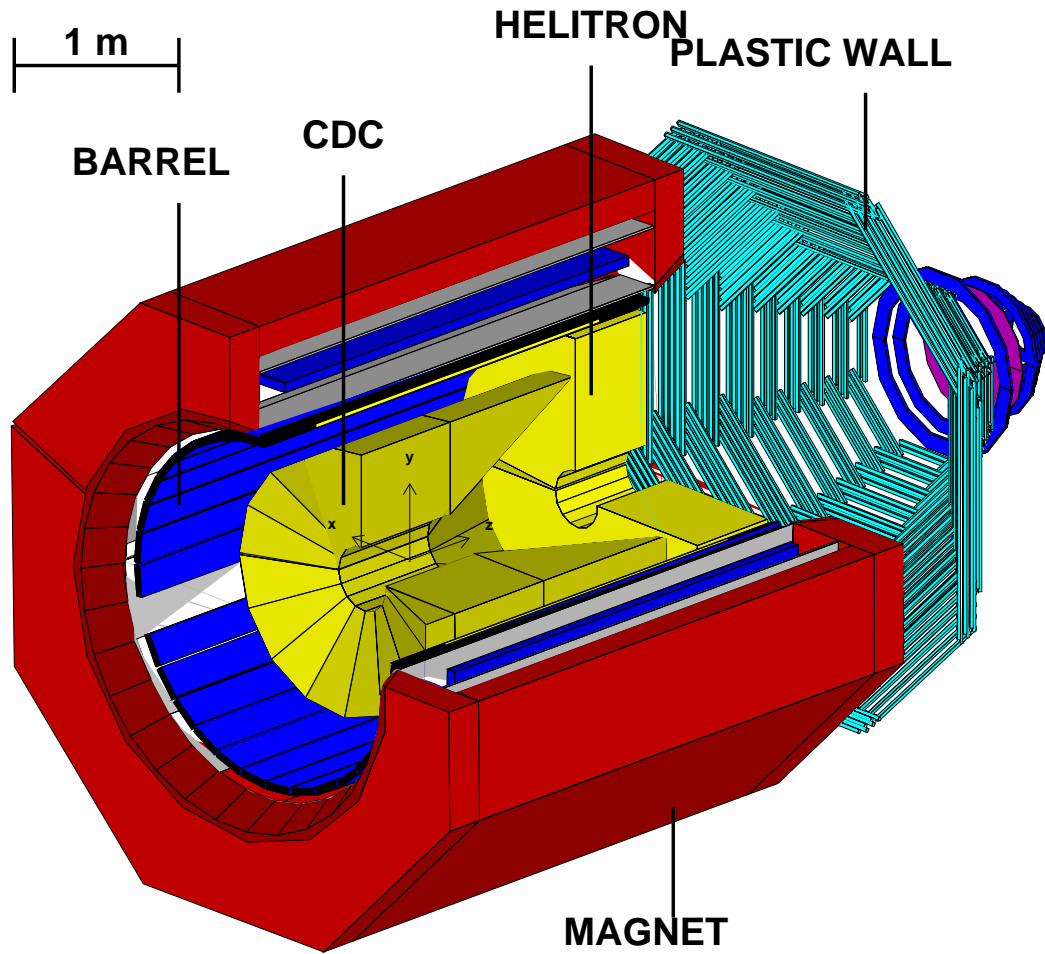


**Figure 2.1:** The FOPI-Detector setup as used in all experiments relevant for this thesis. The drift-chambers CDC and HELITRON (yellow), are surrounded by the superconducting magnet (red). The Barrel (blue) and the Plastic Wall (turquoise) are the ToF systems. See the text for more information.

The detector setup consists of different types of sub-detectors, namely CDC, BARREL, HELITRON, PLAWA, ROSACE, and ZERO DEGREE [Ritman, 1995]. The drift-chambers, CDC and HELITRON, are capable to measure energy loss and the space points of particles passing through their active volume. The other detector components allow determination of ToF and energy loss of charged particles. Later in this chapter, the CDC drift chamber will be described in more detail, as being one of the main subcomponents of the FOPI setup, especially for the measurement of pions.

In order to measure the momentum of a particle, the drift-chambers are placed in a magnetic field  $\vec{B}$  of 0.6 Tesla which is oriented along the beam axis. The field is provided by a superconducting solenoid (red in figure 2.1). The orientation of the field is such that a positively charged particle is bent clockwise<sup>2</sup> and a negatively charged particle is bent counterclockwise<sup>3</sup> as the standard CDC event display is concerned, like shown in figure 2.2. Here, the viewer looks beam upwards. The measurement of the transversal momentum  $p_{\perp}$  (in  $GeV/c$ ) in the CDC is given by the expression [Groom et al., 2000]:

$$\rho = \frac{3.33 p_{\perp}}{B q} \quad (2.1)$$

where  $\rho$  is the radius of the particle track in the xy-plane (in meter), and  $q$  the charge of the particle.

The two drift-chambers, CDC and HELITRON, are placed inside the solenoid. This allows the determination of particle trajectories in their active volume<sup>4</sup>. With the measurement of the energy-loss of every individual particle along the particle track, and the momentum from the curvature of the track it is possible with both drift-chambers to determine the particle species via the Bethe-Bloch formula 2.2

$$-\left\langle \frac{dE}{dx} \right\rangle = 4\pi N_0 r_e^2 m_e c^2 \frac{Z}{M} \rho \frac{1}{\beta^2} z^2 \left[ \ln \left( \frac{2m_e c^2}{I} \beta^2 \gamma^2 \right) - \beta^2 \right]. \quad (2.2)$$

Here  $Z, A$  are the charge and the mass-number of the detector medium,  $N_0 =$  Avogadro number,  $r_e =$  classical electron-radius (2,82 fm),  $z \cdot e =$  charge of the particle,  $I =$  effective ionisation potential ( $I = I_0 \cdot Z$ ,  $I_0 = 12$  eV), and  $\beta, \gamma$  the usual relativistic variables [Blum and Rolandi, 1994].

The above formula describes the mean value of the energy-loss of a given particle per unit of its flight-path in the detector medium. In the matrix of the

---

<sup>2</sup>Most of the detected particles are positively charged, because of the charge of the colliding nuclei.

<sup>3</sup> $\pi^-$  mesons are the most abundant negative particles detected in FOPI; in addition there are a few  $K^-$  mesons detected.

<sup>4</sup>For a detailed description of the working principle of drift chambers see [Blum and Rolandi, 1994].

mean energy-loss per flight-path  $-\langle \frac{dE}{dx} \rangle$  versus momentum, the different particle-species bands can be distinguished, namely pions ( $\pi$ ), protons ( $p$ ), deuterons ( $d$ ), Tritium/Helium 3 ( $t/{}^3He$ ) and alphas ( $\alpha$ ) bands. An illustration of this two dimensional distribution is shown in figure 4.7 on page 43. In order to evaluate the total momentum of a given particle, the polar emission angle  $\Theta$  with respect to the beam axis has to be determined ( $p_{\perp} = p \cos(\Theta)$ ). This measurement is performed with the drift-chambers as explained in the section 2.2.

The central drift-chamber CDC is surrounded by a Time-of-Flight (ToF) plastic scintillator barrel. Matching of CDC tracks with corresponding hits in the scintillator strips is essential a) for identification of rarely produced particles, particularly kaons, and b) for discrimination between fragments with the same masses but different charges (e.g. hydrogen and helium isotopes).

A second ToF array covers the forward hemisphere of the setup. Matching of hits in the scintillator with tracks in the HELITRON yields mass identification in this region of phase space.

The ToF detectors of **FOPI** mainly consist of plastic scintillator stripes which are read out on both ends with photo multipliers. The flight time of a particle is determined from the mean value of the time arrival of the signals, while the position along the strip is deduced from their time difference. ZERO DEGREE and ROSACE are read out only at one side of the strip.

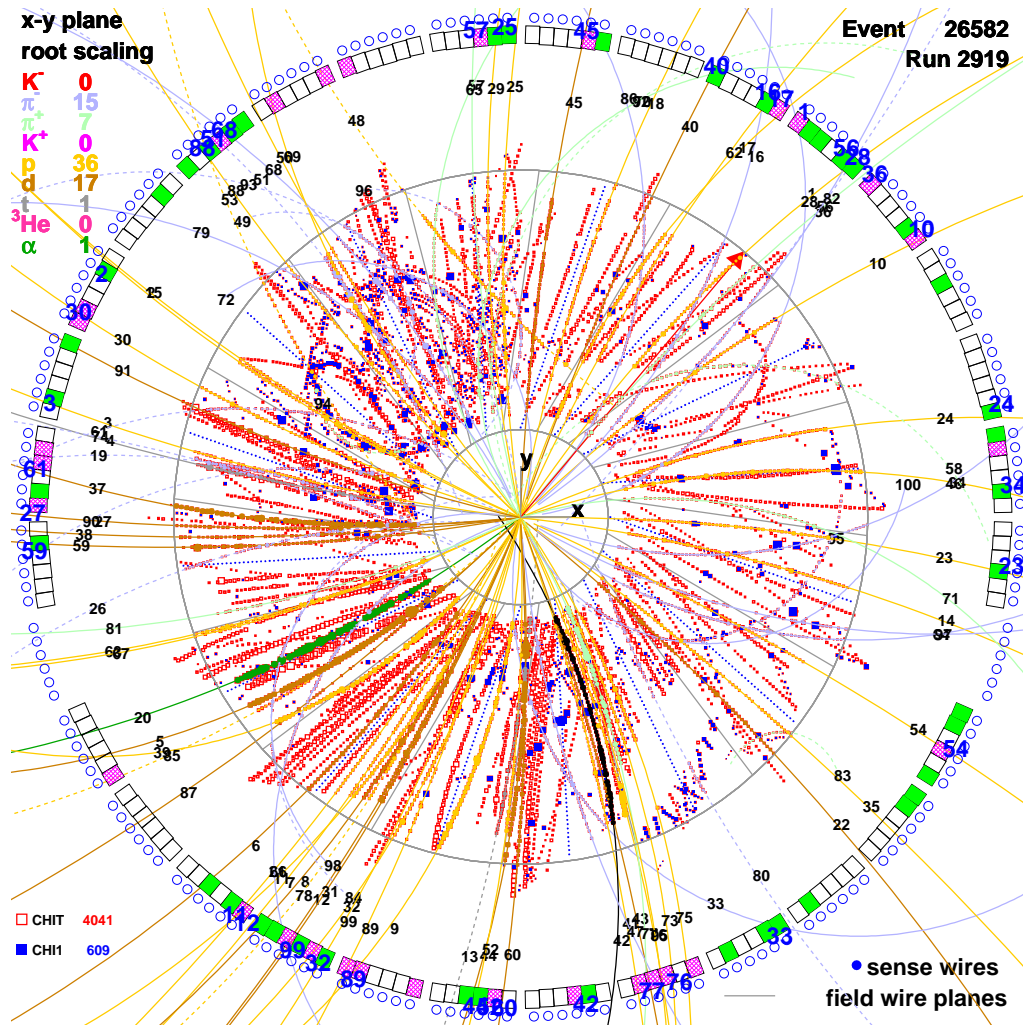
A summary including the angular coverage of the different sub-detector types is given in table 2.1.

detector	type	$\Theta_{lab}$
CDC	drift-chamber	33. - 145.
Plastic BARREL	plastic scintillator	39. - 135.
HELITRON	drift-chamber	8.6 - 27.
PLAWA	plastic scintillator	7. - 30.
ROSACE/ZERO DEGREE	plastic scintillator	1. - 7.

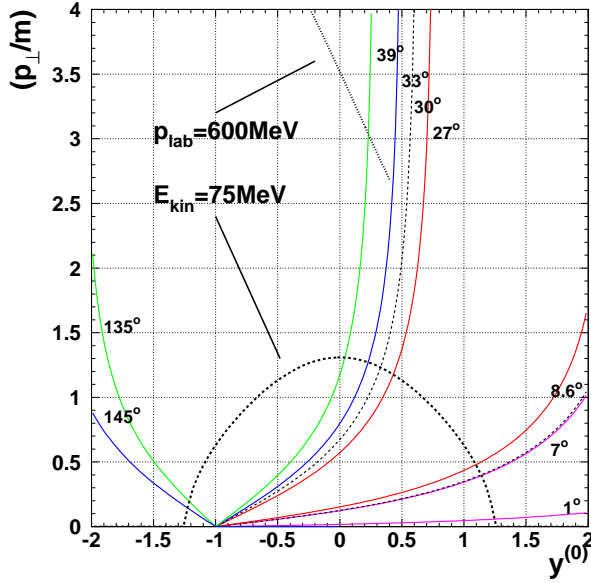
**Table 2.1:** The polar angular coverage of the **FOPI** sub-detectors.

Figure 2.3 shows the phase-space coverage of the complete **FOPI**-detector in terms of transverse momentum and rapidity. The lines indicate the detector borders.  $p_{\perp}$  is Lorentz invariant since it is perpendicular to the direction of motion and therefore unaffected by a Lorentz boost. The rapidity is defined by the following equation:

$$Y = \frac{1}{2} \log \frac{1 + \beta_z}{1 - \beta_z} = \frac{1}{2} \log \frac{E_{tot} + p_z}{E_{tot} - p_z} \quad (2.3)$$



**Figure 2.2:** CDC event display for a Au + Au reaction at 1000A MeV. The red squares denote individual hits. Reconstructed tracks are depicted by full lines, colour codes distinguish between different particle species. The modules of the surrounding plastic scintillator barrel are indicated as well as hits in their strips. The beam points towards the viewer. The trajectories of positively/negatively charged particles are bent clock-/counter-clockwise.



**Figure 2.3:** The phase-space coverage of FOPI. The geometrical acceptance is shown in a representation using  $(p_{\perp}/m)$  and  $y^{(0)}$  ( $m$  the pion mass). The detector borders of the different sub-detectors are drawn. Green: Barrel, blue CDC, red HELITRON, magenta ZERO DEGREE, black dotted line PLAWA.

where  $E_{tot}$  denotes the total energy of a given particle and  $p_z$  the momentum and  $\beta_z$  the velocity along the beam direction.

Throughout this thesis scaled quantities are used: the rapidity is normalised to the centre of mass rapidity and is shifted one unit of scaled rapidity to the left ( $y^{(0)} = \frac{y}{y_{cm}} - 1$ ). Mid-rapidity is located at 0 and the projectile and target rapidities are at  $\pm 1$  respectively.  $p_{\perp}$  is normalised to the mass of the particle ( $p_{\perp}/m$ ). For orientation purposes two additional lines are included in figure 2.3. One labeled with  $E_{kin} = 75 \text{ MeV}$  denotes the position in this acceptance plot of pions with a kinetic energy of 75 MeV. For a temperature of this value the most pions emitted from the reaction zone would appear in this region of phase space. The second line labeled with  $p_{lab} = 600 \text{ MeV}$  denotes a cut for positively charged pions which has to be introduced during the particle identification procedure in order to discriminate pions from protons (see section 4.7).

## 2.2 The Central Drift-Chamber CDC

The active volume of the CDC covers the polar angles,  $\Theta_{lab}$ , between  $33^\circ$  and  $145^\circ$ . The chamber allows the tracking of charged particle trajectories at radial distances between 20 and 80 cm from the target position. The energy loss is measured simultaneously. The CDC is subdivided into 16 sectors in the  $xy$  plane, as seen in the event display shown in figure 2.2. One sector is shown in a cutaway in figure 2.4. The middle of a sector is formed by an anode plane, also called readout

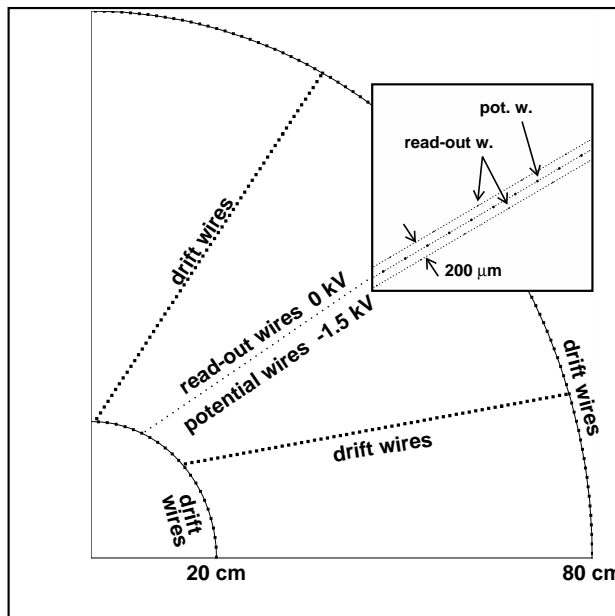


**Figure 2.4:** Schematic view of a CDC sector. The readout plane is centred between two drift planes. The staggering is depicted in the inset.

plane, consisting of 60 grounded readout wires<sup>5</sup>. The electric field, to create the charge amplification in the vicinity of the readout wires, is provided by potential wires spaced between the sense wires. A homogeneous electric field of 750 V/cm, the drift-field, is provided by a field-cage. The field-cage at the inner and outer radius of the CDC consists of the so called drift wires.

A charged particle which passes the active volume of the CDC ionises the counting gas and creates along the flight path ion and electron pairs, which are pulled apart by the drift field. The electrons drift with a velocity of 4.5 cm/ $\mu$ s towards the sense wires. Due to the magnetic field along the beam axis the electron drift direction is tilted against the readout plane. The tilt angle,  $\alpha_L = 33^\circ$ , is called Lorentz angle. The voltage applied to the potential wires of about  $-1.5$  kV leads to a charge amplification of about  $10^4$  with the standard CDC gas-mixture. As counting gas a mixture of Argon, iso-butane, and methane is proportioned 88%, 10%, and 2%, respectively. For the beam-time September 1996 ( $Ru + Ru/Zr + Zr$ ) 3000 ppm  $H_2O$  was added to the gas mixture [Stockmeier, 1996].

The sense wire signals are read out on both ends. The data-acquisition system is described in great detail in chapter 3. However, it is not possible to determine the origin of a hit with respect to the “side” of which the track passed the readout plane. One trajectory produces two tracks: a track belonging to the real trajectory and one mirror track belonging to the mirror hits. To discriminate tracks from mirror tracks the sense wires are placed with a  $200\mu\text{m}$  staggering above and below the plane defined by the potential wires. The inset in figure 2.4 demonstrates this.

<sup>5</sup>Also referred to as sense wires.

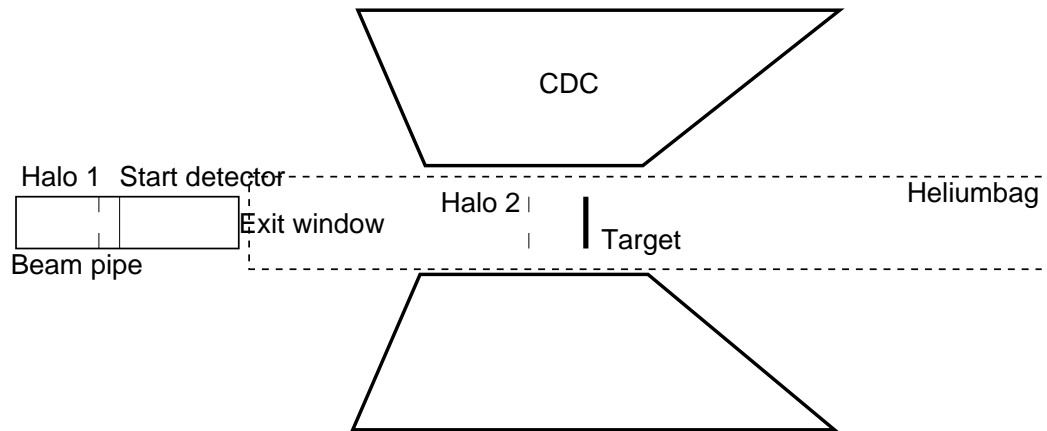


**Figure 2.5:** Sketch of the beam detector system and target of the **FOPI**-setup. Dimensions are not on scale.

Therefore, mirror tracks can be identified as tracks with larger fluctuations in the spacing of hits due to the improper time-offset of the fake hits. In addition to that the CDC-sectors are tilted by  $8^\circ$  with respect to the radial direction. In this environment mirror tracks appear not to stem from the target. Chapter 4 is concerned with the resulting problems of misidentified tracks and therefore misidentified particles.

### 2.3 Beam Detectors and Target

A sketch of the beam detector system and the target is depicted in fig. 2.5. The start detector is placed 2.40 m in front (up-stream) of the target within the beam tube. It consists of a plastic scintillator foil which is read out by two photo-multipliers. The foil is  $50 - 300 \mu\text{m}$  thick depending on the energy and variety of the ion beam. The achieved resolution is typically 50 ps. The start detector serves two purposes. First, counting the incoming beam particles for means of normalisation. Second, yielding a time reference for the ToF detectors. The beam position and beam spot size is defined by an additional Veto-detector, Halo 1.

The beam particles leave the beam tube 140 cm behind the start detector through a capton foil (thickness  $125 \mu\text{m}$ ). To reduce scattering and reactions of the beam with air molecules in the experimental area, a cylindrical bag replenished with helium has been installed. It extends from the exit window of the beam tube, through the whole setup, up to one meter beyond the forward ToF arrays, and fills the inner cylinder of the central drift chamber completely.

The targets are mounted in the helium bag 13 cm upstream from the centre of

the magnet. An additional Veto-detector is installed 9 cm in front of the target. Its purpose is to measure the beam halo and secondary reactions along the beam pipe and the various foils. Its opening ( $\approx 7$  mm) defines the size of the beam spot which has a root mean square radius of typically 3 mm.

The major drawbacks of the detector system described above are the time resolution of the BARREL of  $\sigma \approx 300 - 400$  ps, which restricts the kaon identification capabilities to momenta below 400 MeV/c [Wiśniewski, 2000] and the speed of the data acquisition which limits the event rate to 20 Hz. Solutions to overcome these problems are described in the following chapter.



## Chapter 3

# The FOPI-Upgrade Program

### 3.1 The Data Acquisition System

The Data Acquisition System DAQ system of an experiment is often a factor which limits the extraction of the relevant physics information. Every single event has to pass the data acquisition system in order to be stored on storage devices. The physics information is determined after the experiment, from data which is stored on tape. On this database the offline calibration is performed, and e.g., the particle trajectories of the drift chamber are reconstructed.

The chain of hard- and software pieces from the real detector signals, like pulses on wires of the drift chambers to the list mode data (lmd) files on tape, are called the DA System. Since every single event has to pass this chain, one has to ensure that the system is able to handle the data rate which is produced by the different sub-detectors. One way to transfer the data to the storage device is using fast links between the different DA chains. However, it is not possible and even not necessary to tape every event. Certain criteria are developed to decide whether or not an event is worth to be stored. This allows to reduce the number of events, and hence the volume of the data which is to be transferred per time unit.

The collection of hard- and soft-ware to decide whether or not an event is worth to be stored is called trigger. The more knowledge of the event a trigger uses to make the decision, the higher the so-called trigger level is.

A very basic trigger, and until now the only trigger conditions used in **FOPI**, are triggers on the charged particle multiplicities in the plastic wall, accompanied by beam-detector informations. The multiplicity conditions are chosen in a way that the event samples accepted by the trigger are enriched with central event types. This trigger is called in **FOPI** the first level trigger. In order to trigger on more specific physics observable a more sophisticated trigger is needed, e.g. performing online track reconstruction and momentum reconstruction. For ex-

ample, with the knowledge of momentum and velocities of particles, events with produced kaons could be preferably recorded. Section 3.4 describes how a second level trigger can be introduced in the **FOPI** device. In the following, the readout of the drift-chambers is discussed in some detail. As far as the upgrade of the DAQ of **FOPI** is concerned, the greatest changes are by now undertaken on this part of the system partially based on the proposals developed as part of this work.

## 3.2 Readout of the Drift Chambers

The drift chambers are the slowest sub-components in the **FOPI**-setup, as far as both the readout and the operation are concerned. This is due to the relatively long drift-time of about  $5\mu\text{s}$  and the slow readout of the detector data. The functionality and capabilities of the two drift chambers were described in the previous chapter. The original signals of the drift-chambers are propagated as differential signals via unshielded twisted pair cables to "FADC-crates". They are fed into the FADC-modules through a so-called analog backplane, which is nothing more than an interface to the individual modules. Signal readout is done with a **Flash Analog Digital Converter** system (FADC system), which samples the measured pulse with 100 MHz frequency. This means that the evolution of the pulse height is measured every 10 ns. There are 8 Bits available to store each measured analog value in a digital form. The conversion is not linear, so that the effective pulse height information is on the level of 10 Bit.

By this procedure the analog drift chamber signal is converted to a digitised signal. The signals of both ends of four wires are sampled by one FADC-module (8 channels per module). 24 FADC-modules were located in one FADC-crate and they were read out with one readout module. This was the status of the drift-chamber part of the readout-system until 1997. In the following the changes are described which were attempted in order to enhance the speed of the readout of the drift-chambers by a factor of four.

The first step to enhance the DAQ speed is to divide the backplane into two individual parts. This increases the speed by a factor of two, since now the two parts are read out in parallel. The former combination of a sampling module (which puts the addresses to be filled on the FADC memory) and a scanning module had to be replaced. A new **Scanning Sampling Module** (SSM) was developed. It combines the functionality of the two previously used modules. A detailed description of this SSM is given in section 3.2.1.

Technically the FADC-backplane consists of two backplanes. One of them is the previously mentioned analog backplane. This backplane is divided into two halves due to mechanical reasons as well. However, this is not connected to the readout of the modules and therefore not responsible for a speedup in data

acquisition rate. The second backplane is the digital one, on which the digitised signals are propagated from the FADC-module to the SSM. First tests with the divided backplane and the SSM module were performed within this work. The test setup described in section 3.2.3.

The new SSM can scan the FADC-data with 33 – 40 MHz frequency instead of 16 MHz, with which the old scanning module operated. This leads again to a factor of two improvement of the performance of the readout system as far as its speed is concerned.

### 3.2.1 The Scanning Sampling Module

The Scanning Sampling Module (SSM) is a **F**ield **P**rogrammable **G**ate **A**rray (FPGA) based printed-circuit board (PC-board). The whole functionality is integrated in this programmable chip. The programme is written in the hardware description language VHDL<sup>1</sup>. Once the the program is written, functionality tests are done within VHDL itself. The surrounding PC-board can be simulated in a way that input signals, e.g., FADC-data, are fed into the FPGA-program. The generated output can be compared to the expected output. After the successful functionality tests, the FPGA-program has to be synthesised and routed. With the routed program the timing constraints can be tested again with the now known delays for every signal. The routed "program" is transferred to an **E**lectrically **E**rasable **P**rogrammable **R**ead-**O**nly **M**emory (EEPROM), from which the FPGA loads the program when powered on.

The main purpose of the SSM is a low level hit detection combined with the zero suppression. As mentioned in chapter 2, both ends of one wire are read out. This is done in parallel in a way that the left and right (upstream and downstream) data are available simultaneously. The hit detection can be performed using the information coming from both ends of the wire. At this stage of the data acquisition, a hit is defined via the following condition: one hit starts when two consecutive samples on at least one side of a wire are over a certain threshold, and ends when both ends of the wire are below this threshold. With this definition it is not guaranteed that closely spaced hits are separated. In addition to the detected hit, the scanner can store between 0 and 7 pre-samples and 0-5 post-samples, before and after the hit, respectively. Samples in front of/behind the hit are called pre- and post-samples. The pre- and post-samples are used in the next level of data reduction to determine the baseline on which the hit is located. Figure 3.1 visualises a hit with pre- and post-samples. The hits from the scanner including the pre- and post-samples are commonly called hitlets. Figure 3.2 shows a pulse, gener-

---

<sup>1</sup>VHSIC Hardware Description Language. VHSIC is another acronym which stands for Very High Speed Integrated Circuits.

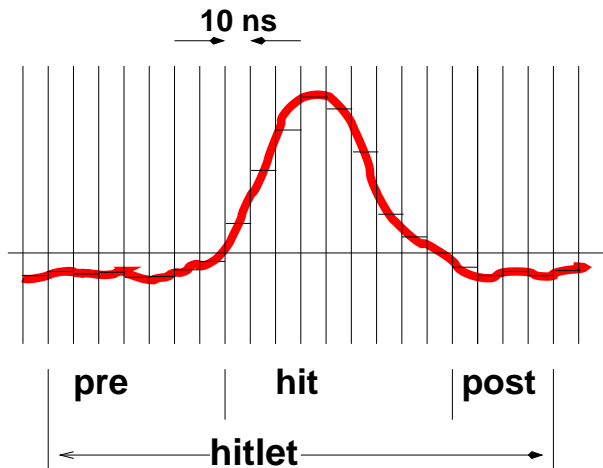


**Figure 3.1:** Scheme of a drift-chamber hit. The hit from the wire (red) is digitised in 10ns time intervals. Pre and post samples are indicated. The horizontal line indicates the threshold.

ated with a pulser, digitised with a FADC (upper panel in figure 3.2). The pulser output is distributed over all FADCs as indicated in figure 3.4. Therefore the left and right signal in this example (figure 3.2) are identical. The upper panel in figure 3.2 is read out using the SSM. The FADC signal is accessible directly via the SSM. The so called dump mode is part of the SSM functionality and provides the possibility to check the hit recognition of the SSM. The hit detection is performed with this data as input data. The lower panel of figure 3.2 shows the detected hit with pre- and post-samples as delivered to the next station of the readout chain. Note that the position of the pulse before and after the hit recognition is not the same along the x-axes. In the upper panel of figure 3.2 this axis denotes the FADC-addresses. 1024 time bins with a width of 10ns are available. The whole range of about ten  $\mu$ s are shown between the time bins 0 and 1024. The numbering of the bins is chosen in a way that the number of the bin corresponds to physical address offset of the FADC-memory. This is different in the lower panel of 3.2. During the experiment the FADC-memory is used continuously as a ring buffer. Therefore, the numbering of the bins corresponds to the number of time bins relative to the stop signal.

In order to guarantee a fast data transfer from the SSM to the **Steuerungs- und Auslese Modul (SAM)** (the next data reduction station), the **Geräte Bus GTB** interface provides a fast data transfer mode, called token mode. In this fast mono directional transfer mode, the SSM transfers the detected hits with pre- and post-samples to the SAM. In addition to this mode, a slow, bidirectional address mode can be used to program the thresholds, number of pre- and post-samples, scan range, and so on. In this address mode, one has transparent access to the FADC-memory. The address mode is only used to program the SSM and for debugging purposes during the development of the module. The available registers and hit buffer memory addresses are described in [Köpfler, 2001].

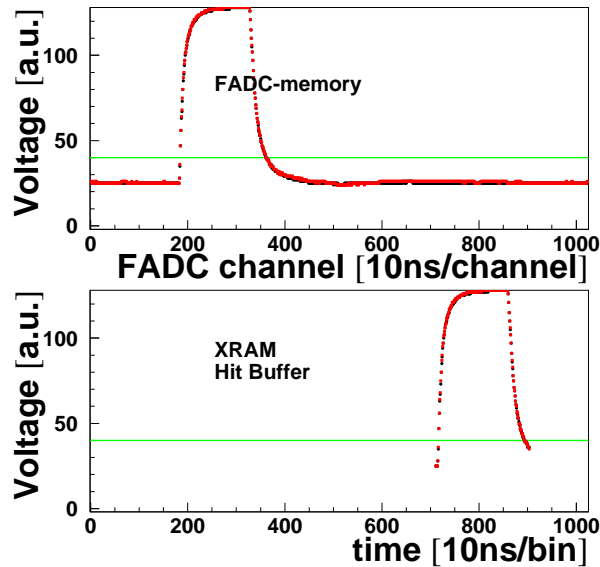


**Figure 3.2:** FADC dump and SSM hitlet. Upper panel: the FADC memory directly accessed via the SSM. Lower panel: Hitlet after hit recognition by the SSM. Colours: two channels corresponding to two ends of a wire. Further explanation see text.

The normal operational mode is the direct transfer of detected hits over the GTB to the SAM parallel to the hit detection. Both parts of the FADC-crate are read in parallel and two SSMs transfer the zero suppressed data simultaneously to one SAM. This provides a factor of 1.5 to 1.8 speedup, depending on the number of hits, since in the old setup scanning and data transfer were done via a VSB sequentially.

### 3.2.2 The SAM and Data Reduction

The SAM (Steuerungs- und Auslese Modul), now in the third generation, was originally developed for the cancer therapy by Jan Hoffmann at GSI [Hoffmann, 2001]. It is a VME<sup>2</sup> module with two GTB interfaces. The VME standard defines crates with a backplane which enables VME modules to communicate with each other. From two FADC-crate halves, the data can be received in parallel. The SAM module has two almost independent data paths, each for one GTB interface. From a small buffer memory (XRAM, YRAM), the data will be processed by two **Digital Signal Processors (DSP)** which will perform the data reduction, and the transfer to a dual ported ram<sup>3</sup> from which the data can be transferred over the VME backplane to a front end computer (RIO<sup>4</sup>). The possible data paths on the SAM3 board are depicted in figure 3.3. As on the SSM

<sup>2</sup>The term 'VME' stands for **V**ERSA**m**odule **E**urocard

<sup>3</sup>Dual ported ram: accessible by two interfaces in parallel.

<sup>4</sup>Described in section 3.2.3.

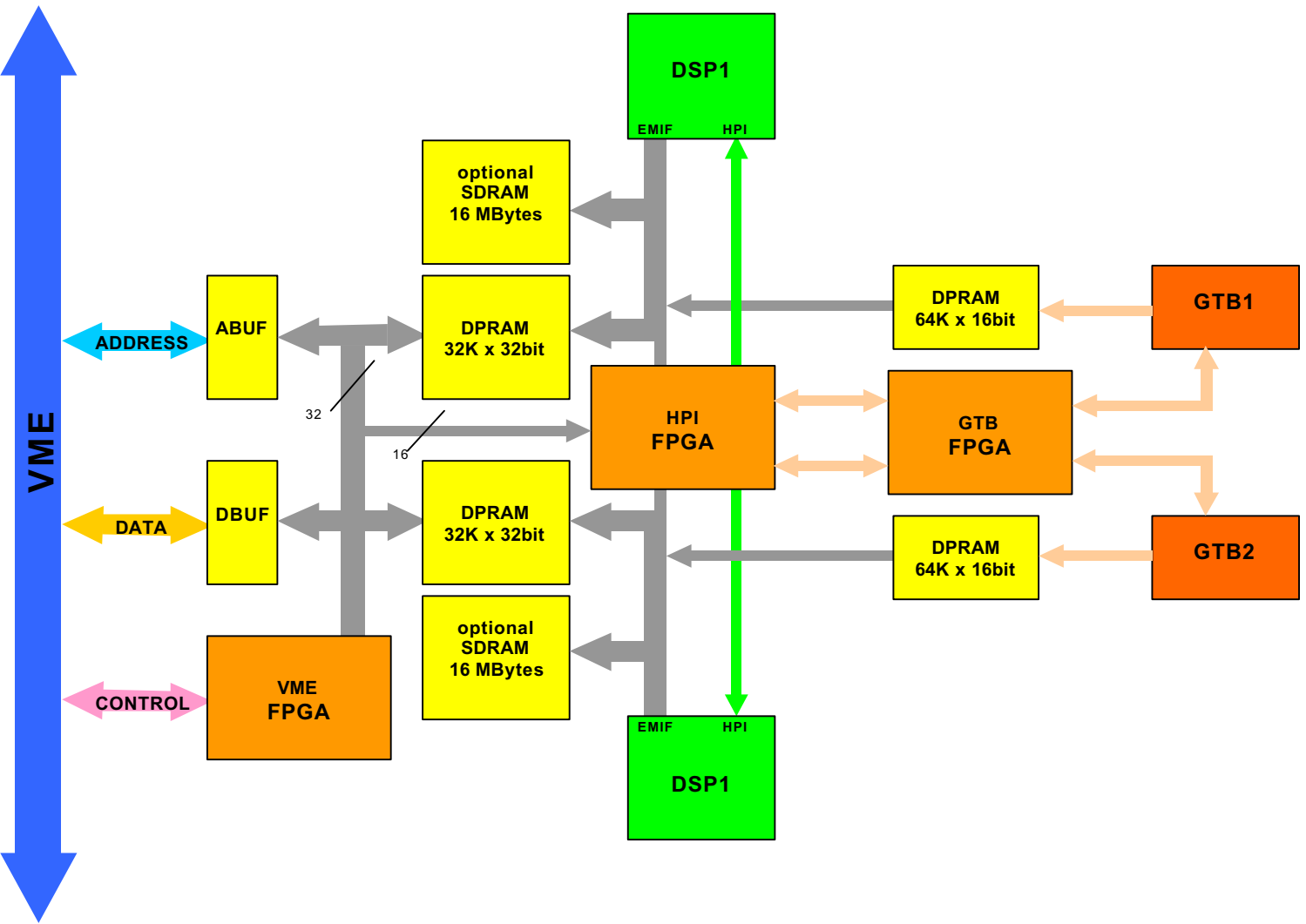


**Figure 3.3:** SAM3 technical sketch. The figure is taken from [Hoffmann, 2001]. The XRAM (YRAM) is connected to the GTB1 (GTB2) and is labeled with its size (64K × 16bit) and the RAM type (DRAM).

PC-board, FPGAs are used for the integration of bus protocols. The VME and GTB protocols are placed into separated FPGAs. Due to the possibilities of these programmable chips, changes in the implementation are easily applied without a change in the layout of the PC-board. Fast VME access is provided by the implemented 32 and 64bit block-transfer<sup>5</sup>. This mode will be used to transfer the data from the SAM3 to the sub-event builder (see section 3.2.3). The computing core consists of two TMS320c6701 DSPs manufactured by Texas Instruments. In the **FOPI**-setup the data reduction of the hits transferred from the SSM will be performed with these processors.

**FOPI**, in contrast to similar heavy ion experiment, uses an online data reduction on the bases of detected hitlets in a physics manner. Detected hits from the SSM are examined and reduced with a program running on the DSPs of the SAM. This program inspects the hitlets for valid hits and thus performs double hit recognition; a hitlet can contain hits originating from different tracks, due to the hit-definition used in the SSM module. The data corresponding to one hit (information acquired on both left and right ends of a wire) are reduced to five data words<sup>6</sup> namely the arrival times of the hit left and right, and the charge deposit which is connected to the energy loss of the particle which produced this hit  $t_l, t_r, q_l, q_r$ . Additionally information on overflows and pulse shape parameters (rise time and integration time) is transferred as well, coded in the fifth data word. This type of data reduction reduces the hitlets in a way that only the physics relevant information is transferred to the next station of the readout scheme.

### 3.2.3 VME Data Transfer Test

The DAQ system was evaluated in a small test system as depicted in figure 3.4. The readout chain of the drift-chambers is reproduced in a smaller scale. Input data from the drift-chambers is simulated by a pulser and fed to all FADC-modules. In contrast to the real DAQ, the pulser signals are not introduced via the analog backplane of the FADC-crate. The test input of each FADC-module is used instead. The splitted FADC-backplane was tested in this setup the first time. The newly developed terminator works properly with the splitted backplane that the transfer tests on the backplane were successfully completed. The FADCs are read out with the newly developed SSM. The SSM itself delivers the data to the SAM via the GTB. Finally, the RIO-board collects the data from the SAM-module. The VME module is a CES<sup>7</sup> RIO 8062 PowerPC card running the real time operating

---

<sup>5</sup>Block-transfer: The data transfer is initiated by the transfer of a start address and a block-size. The transfer is than performed without addition overhead.

<sup>6</sup>One word consists of 16Bit.

<sup>7</sup>Creative Electronic Systems, company name.

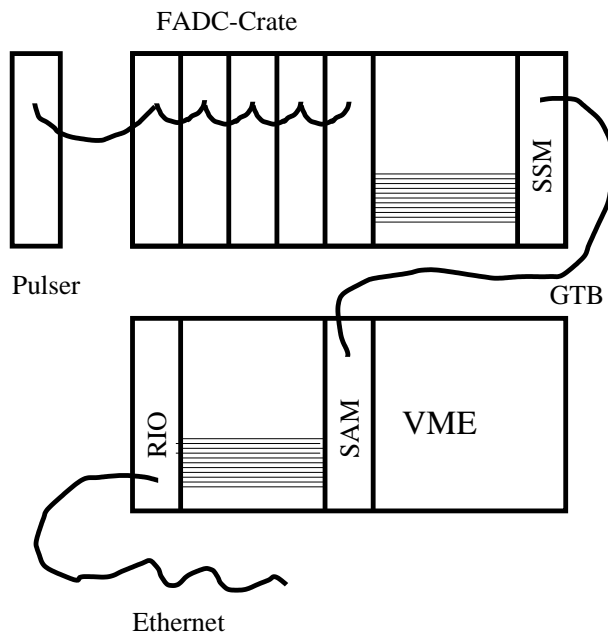


**Figure 3.4:** Heidelberg DAQ test system. Signals, generated by a pulser, were read by a SSM. The SSM is accessible via GTB from a SAM. The RIO module provides the access point from normal Ethernet to the SAM.

system LynxOS. This board uses a PowerPC 604 chip with 200MHz frequency as Central Processing Unit (CPU).

With this setup, first functionality and programming tests were performed. The programming of the SSM was implemented and tested. The fast data transfer using the GTB token mode can not be used due to a handshake problem in the GTB protocol which is implemented in the FPGA on the SSM board. In the present state, a data transfer is only possible from the internal hit-buffer memory of the SSM to the SAM X- or YRAM with the slow address mode. This readout configuration was used in a HELITRON test beam-time. The HELITRON data were transferred to the DAQ system with a transfer rate of approximately 4-5 events per second which is the speed limit in this configuration.

The data which is read out from the scanner and sent to the readout processor has to travel from the SAM over the VME Backplane to the RIO powerPC system. The speed of this data transfer is also limited and depends on the data transfer mode. The fastest transfer mode is a 64bit block-transfer, which will be available on the next generation SAM, called SAM3 (already introduced in section 3.2.2). In order to test the data transfer over the VME backplane before the availability of the new SAM, the data transfer was tested in the following ideal setup: two RIOs were configured in a master/slave setup and the transfer was initiated from the master. The transfer rate was measured with this system as 27 Mb/s. This is the maximum transfer rate on the backplane.

### 3.3 Status of the Readout Project

The central data-collection will be realised with PC based taping devices. The number of PCs which will be used as event builders is not fixed yet, and depends on the data rate which will have to be stored. The Multi Branch System (MBS) software, which will be used as the data acquisition software, can handle  $m$  data producers (sub-detectors) and  $n$  consumers (main event builders). This explains the  $m \times n$ -MBS naming of the software. The central data transport will be performed via a gigabit Ethernet. The gigabit Ethernet is already installed in the experimental hall, where the **FOPI**-detector is located and in the "Meßhütte", where parts of the experiment electronics are located. All sub-detectors are connected to this gigabit Ethernet via a sub-event builder.

A sketch of the complete, upgraded DAQ-system is shown in figure 3.5. The drift-chamber readout consists of 22 FADC crates and 44 SSM modules. 22 SAM3 modules will perform the data reduction and 4 or more RIO2 VME modules will deliver the sub-events of the drift-chambers to the main event builder in figure 3.5 referred to as Lynx PC. The MBS software is running on all CPUs under the operating system LynxOS.

### 3.4 A Second Level Trigger

The feasibility of implementing a second-level trigger into the **FOPI**-setup was investigated. As shown in [Best et al., 1997], it may not only enhance the capability of measuring  $K^+$  but, moreover, may as well allow to perform the same studies for  $K^-$  as well, namely flow studies, extraction of centrality dependencies and measurements of rapidity distributions. The pronounced and opposite in medium effect for  $K^-$  and  $K^+$  connected to the mass of the kaon is a matter of great theoretical [Schaffner et al., 1997] and experimental interest [Wiśniewski et al., 2000]. This difference, if it exists, can be really pinned down by measuring both,  $K^-$  and  $K^+$  with a statistically immovable accuracy. One effective way of increasing the statistic is to extend the beam-time of the measurement, and to write more events on tape. However, this leads to a necessity to store an enormous amount of data as well as to unacceptable beam-time duration. A better way is to introduce a more sophisticated trigger device in **FOPI** with the capability to identify kaon tracks in the event. The decision to archive the event should be available within  $100\mu\text{s}$ , in order to significantly reduce the dead-time of the DAQ system. While archiving an event the DAQ system cannot handle a second event. This circumstance blocks the DAQ for approximately 1 – 1.2ms. A trigger decision within  $100\mu\text{s}$  would reduce the dead-time of the system of a factor of 10. In order to fulfil that requirement, it is mandatory to obtain all the relevant information of an event as fast as

## FOPI DAQ UPGRADE

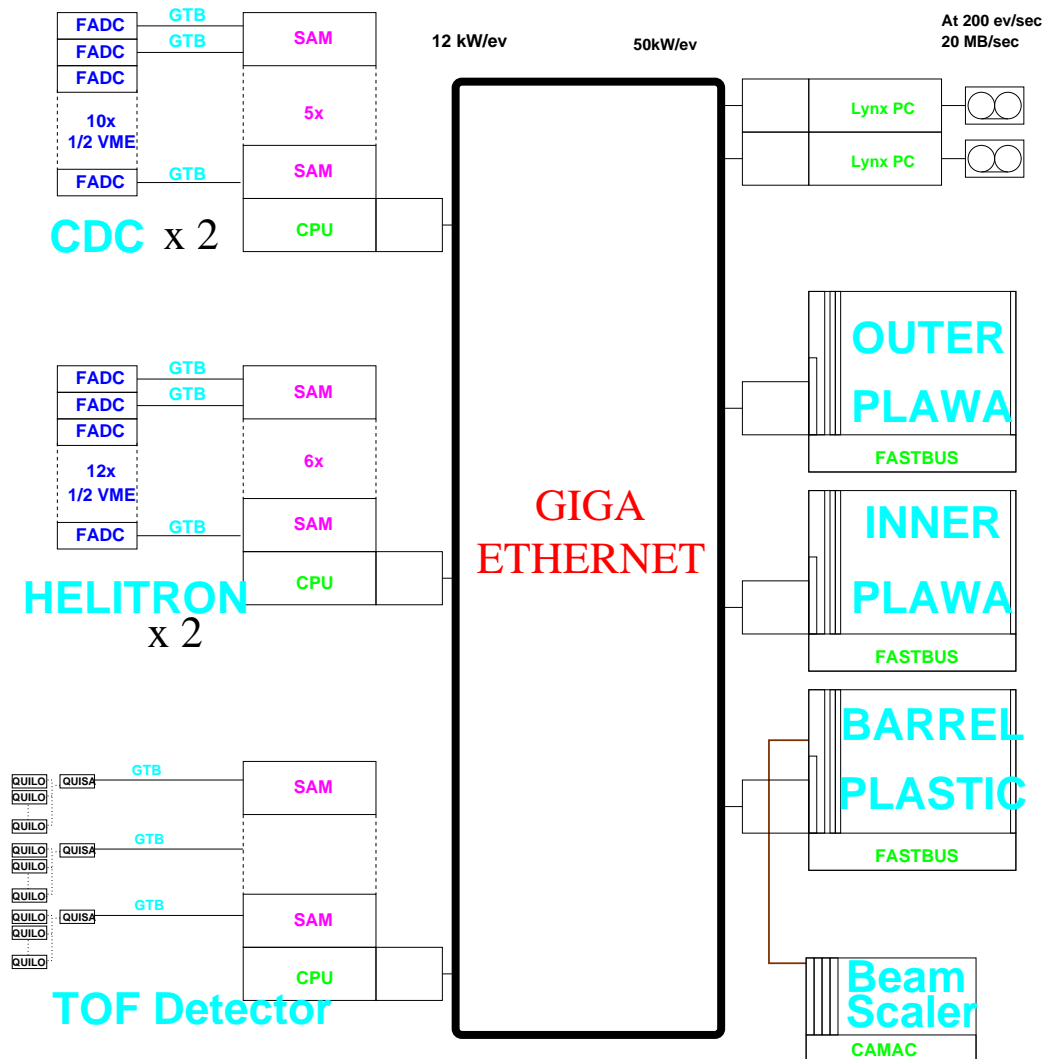


**Figure 3.5:** The future DAQ-System of the FOPI-detector. All sub-detectors are represented by their readout system. Fastbus systems for the forward ToF and the plastic BARREL (right) are connected via a RIO to the Gigabit Ethernet. The SAM and RIO modules of the new ToF detector (bottom left corner) are similar to the drift-chamber readout.

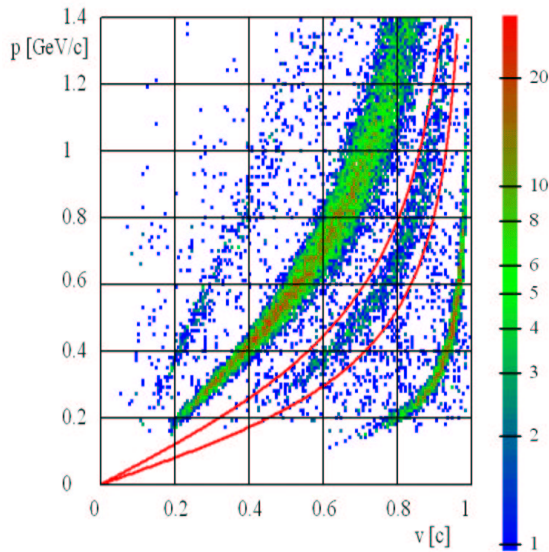


**Figure 3.6:** Two dimensional matrix: momentum  $p$  versus velocity  $v$ . The FPGA processor board Atlantis is able to process one event in  $100\mu\text{s}$  and identifies events with tracks in the region of interest (indicated by the two red lines) [Brosch, 2001].

possible. It is necessary to track the particle trajectories in the CDC, to match the tracks with hits in the time of flight barrel, to make use of the information about the  $z$ -coordinate in the ToF barrel, and to deduce the momentum of the track. Using the information about the momentum and the velocity, kaon candidates can be identified as shown in the matrix momentum  $p$  versus velocity  $v$  in figure 3.6. If tracks can be identified in the region of interest, indicated by the red lines in figure 3.6, the trigger starts the data acquisition for the currently considered event. If not, the event is discarded. However, the available information on the event is very limited at a time when the FADC are not read out. The arrival times of pulses are in principle available and the ToF information is already acquired as well. The arrival time can be deduced from a discriminator signal at the FADC front-panel. This signal indicates when a signal on a wire is above a certain threshold. A specific hit recognition is not performed at this discriminator output. At this point, many problems can be immediately identified. First of all, the information of  $\langle \frac{dE}{dx} \rangle$  is not accessible. Secondly, since the output is a combined signal of both ends of a wire, no information is given by the system on the  $z$ -coordinate of the hit. Last but not least, the output of the discriminator relies on the correct setting of the thresholds. Figure 3.7 shows the possible input of a second level trigger, if the threshold is set to a too low value. The noise will introduce fake signals and therefore fake hits which don't belong to a real signal and a track. Figure 3.7 shows a real  $Au + Au$  event at an energy of 1.0 AGeV. The red triangles are hits which are detected by the scanner. The black crosses are the accepted hits after the data reduction algorithm. The noise hits introduce straight tracks parallel to the sense plane. With a proper setting of the threshold the number of detected fake hits can be reduced significantly.

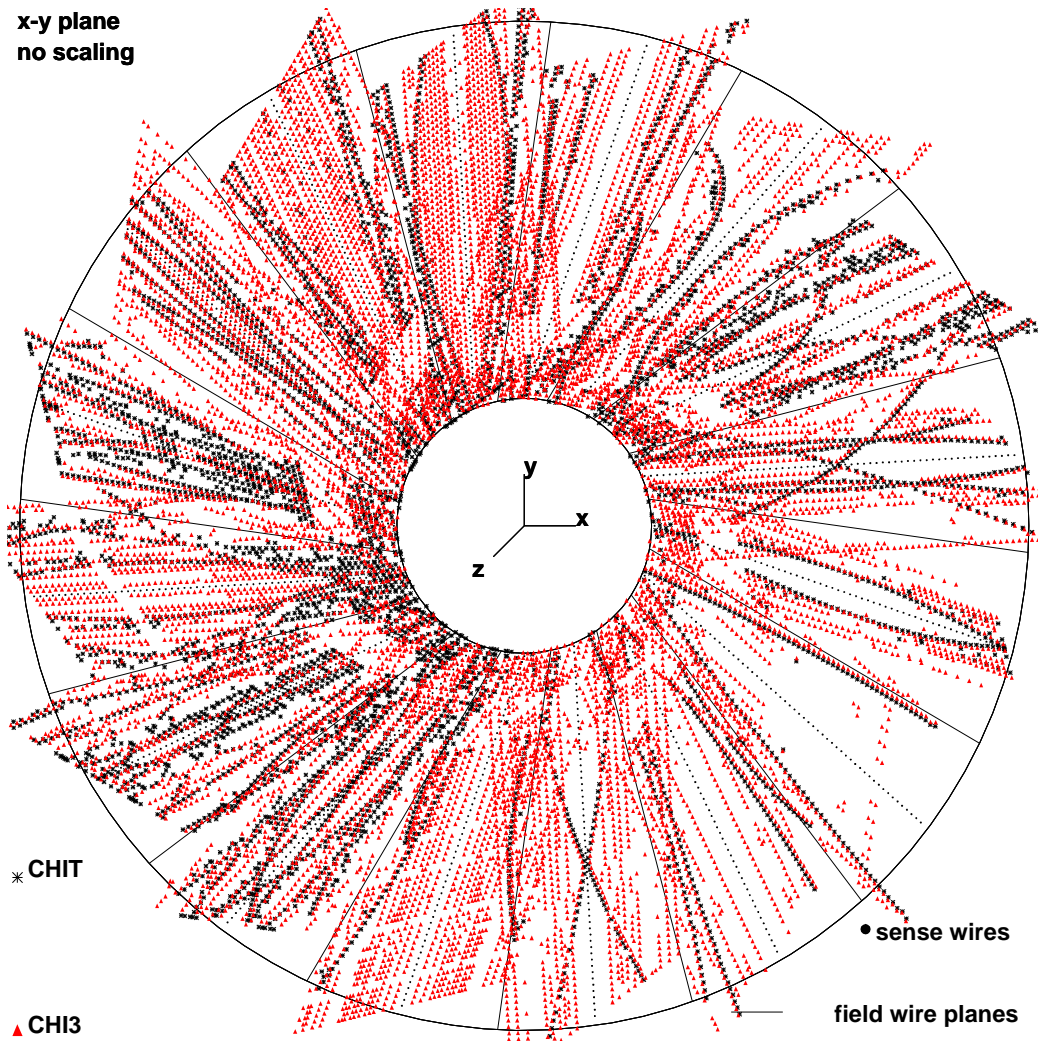


**Figure 3.7:** CDC event display with noise (red) introduced by a threshold setting of the FADC discriminator close to the noise level. The hits detected by the DAQ system are shown in black.  $[Au + Au]$  @ 1.0 AGeV

The trigger receives the time of flight information via the normal read-out scheme – a GTB bus, split to feed both, the trigger and the DAQ. In [Brosch et al., 2000] a hardware device is proposed which can handle the requirements for the usage in a second level trigger device.

The principle scheme of the second level trigger introduced here was developed during this thesis. The possible performance and hardware requirements are currently analysed [Brosch, 2001]. Figure 3.6 shows the outcome of the algorithm, which is supposed to be implemented on this Atlantis board.

Another field of application of this type of trigger could be the enhancement of high multiplicity pion counts whereas the statistics falls short also.

### 3.5 Changes and Future Enhancements of FOPI

The most significant change in the FOPI-setup is the upgrade of the ToF system which is mandatory in order to provide additional, valuable measurements in the field of "strangeness physics" at SIS-energies. Knowing the time of flight and the momentum of the particle, one can discriminate between  $\pi^+$ ,  $K^+$  and protons even in the momentum regime in which these particles are not separated with the information from the CDC alone. The research initiated by the FOPI collaboration was first focused on a PesTOF spark counter. The measurements and extensive tests of different PesTOF counter types are described in [Devimes, 2001]. The tests looked very promising since the counter fulfilled all the experimental requirements. However, it turned out that the conductive glass used in the counters has no longer the required mechanical properties, when it is produced in large quantities. The collaboration decided during the autumn meeting 2000 to search for a new type of ToF system. The so-called GRPC (glass resistive plate counter) system is now under development.

In order to have enough space to install the new ToF System the Čerenkov Barrel was removed from the setup. The old scintillator strips of the Plastic Barrel were replaced by new scintillator material. Additionally, they were shortened that they now cover the angular range  $65^\circ < \Theta_{cm} < 135^\circ$ .

The second and very important change are new CDC wires. The performance of the drift-chamber degraded over the years of operation. For some examples of damages of potential and sense wires see [Stockmeier, 1996]. Therefore, all drift and potential wires are changed as well as the wires of the outer field cage. However, the HI reactions described in this work are all measured with the old setup.



## Chapter 4

# Analysis of Experimental Data

The aim of this thesis is to derive the absolute number of pions as a function of the number of participating nucleons,  $A_{part}$ . In this work, only the CDC is used to identify charged particles. Consequently the particle identification is based on the energy loss versus momentum matrix and the functional dependence of the energy loss on particle mass, given by the Bethe-Bloch formula (equation 2.2). The pion identification procedure is described in section 4.7 on page 43.

With the available **FOPI** data, the production of charged pions can be studied as a function of system size and beam energy. The beam energies covered by the **FOPI** experiments range from 400 AMeV to 1500 AMeV. The system size systematics comprises symmetric beam–target combinations from  $Ca + Ca$  to  $Au + Au$ . The experiments of which data-sets are discussed in this work are briefly described in the following section. The general strategy for event selection, including background determination is described later on. Finally, the method used to derive the pion multiplicity is presented.

### 4.1 The Experiments

This thesis is based on two experiments, namely the S183 experiment (Isotopic ratios) and A183 experiment (Excitation function). The first one, which took place from 30-Aug-1996 until 26-Sep-1996, was performed with Ruthenium and Zirconium as beam and target. The second experiment run from 5-Aug-1997 until 27-Aug-1997 with Gold and Calcium as beams and targets. The considered reactions and energies are listed in the following table 4.1. In all experiments the target thicknesses were chosen in a way that 1 % of the beam particles interacted with the target foil. Typically, the duration of a spill<sup>1</sup> was about 8-10 seconds, and the number of particles per spill were set to  $5 \cdot 10^5$ , so that on average every 2 ms a

---

<sup>1</sup>Extraction time of the beam from the SIS

reaction (used)	target thickness	isotopic enrich- ment	energy [AMeV]
$^{96}\text{Ru} + ^{96}\text{Ru}$	431 mg/cm <sup>2</sup>	96.52 %	400, 1000, 1528
$^{96}\text{Zr} + ^{96}\text{Zr}$	380 mg/cm <sup>2</sup>	95.6 %	400, 1000, 1528
$^{197}\text{Au} + ^{197}\text{Au}$	202 mg/cm <sup>2</sup>	100 %	400, 1000, 1490
$^{40}\text{Ca} + ^{40}\text{Ca}$	386 mg/cm <sup>2</sup>	96 %	400, 1000, 1500

**Table 4.1:** Experimental conditions and energies for all reactions examined in this work. Quoted numbers for the *Zr*-target consider the Zirconium only.

reaction took place. In both experiments, the **FOPI**-detector was used in the setup as described in the previous chapter.

A trigger scheme without distortions of the multiplicity spectrum of charged particles is not possible. Such a trigger would lead to the full impact parameter distribution determined e.g. with the charged particle distribution. To grant a large impact parameter range a so called minimum bias trigger is used. The bias introduced by such a trigger is supposed to be small. Technically the trigger is defined as a multiplicity trigger requesting a certain number of hits in a fast plastic scintillator detector like the Plastic Wall and/or the Barrel. For the minimum bias reaction trigger at least one particle in the plastic wall is mandatory. Since under this trigger conditions, the background stemming from events originating not from the target is typically large for low multiplicities, in addition, at least one hit in the plastic scintillator barrel surrounding the CDC is required. This condition, the so-called minimum bias plus barrel (MB+bar) trigger, is close to the minimum bias trigger and available for all experiments. For the lowest charged particle multiplicities and therefore peripheral reactions residual influence of the trigger condition is unavoidable.

## 4.2 Event Selection

A real event is the interaction of one beam nucleus with one target nucleus. All other events are called background events. There are several places where the beam can interact with matter besides the target. Section 2.3 (page 16) describes the material and components which can contribute to background events. Back-

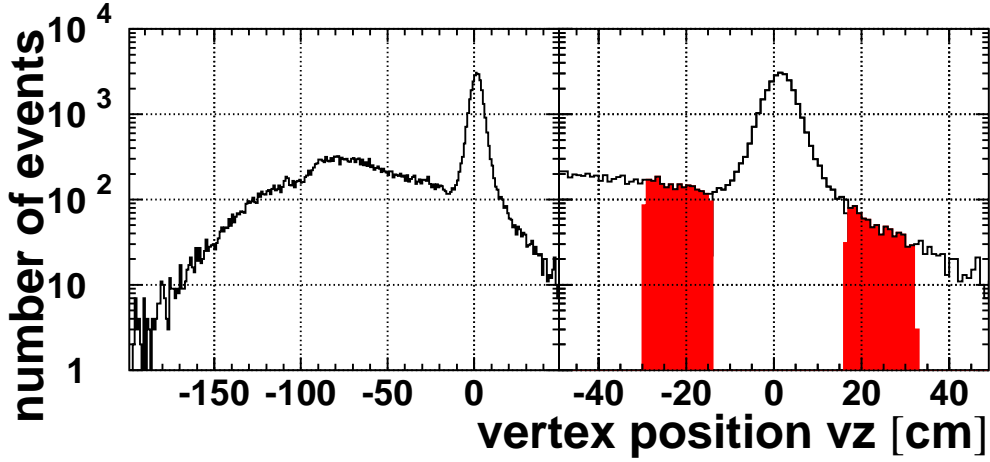


**Figure 4.1:** The distribution of the interaction vertex along the beam axis; left for a large range of  $z$ , right the enlarged view around the nominal vertex position. The red shaded areas on the left and right side of the peak show event samples used for background estimation. [ $Au + Au$  @ 1.0 AGeV, MB+bar trigger condition]

ground events which are accepted by the trigger described in the previous section have their origin close to the detector, e.g. the start-detector foil.

Principally, the event vertex can be reconstructed from the particle tracks registered in the CDC. Typically, vertex resolutions of 2.0mm in the  $xy$ -plane and 3-10cm in the  $z$ -direction, depending on the particle multiplicity, are achieved. The accuracy of the latter is determined by the charge division resolution of the CDC.

The reconstructed position of the event vertex is used to discriminate background events and to estimate the contribution of background events to events with the proper  $z$ -position. The necessary information is contained in the position of the reconstructed vertex along the beam axis,  $v_z$ . Figure 4.1 shows a distribution of this variable in two different scales. On the left side, the distribution is shown for  $z$ -coordinates down to the exit window of the beam pipe. This indicates that nuclear reactions of beam particles take place over a whole range of distances around the nominal target position at 0cm. A prominent peak is located around the nominal target position. Events with  $|v_z - v_{peak}| \leq 10\text{cm}$  are considered to stem from the target ( $v_{peak}$ : peak position of the  $v_z$ -distribution). Events which fulfil these cut criteria are selected for the further analysis.

It is worth to mention that the typical target size in  $z$ -direction is about  $200\mu\text{m}$ . This has to be compared with the selection criterion of about 10cm around the

peak position. The nominal target position is at the origin of the coordinate system used in this analysis. Since the event vertex is reconstructed using all tracks in the considered event, the width of the event peak is primarily affected by the accuracy with which the position of individual hits in the CDC along the  $z$  axis can be determined and the track multiplicity,  $N_{track}$ , of the event,  $\sigma_{vz} \approx \frac{1}{\sqrt{N_{track}}}$ .

### 4.3 Background Determination

The event vertex distribution around the target position is shown on the left side panel of figure 4.1. It is evident that there is a considerable amount of background events even in the event sample of which the deviation of the reconstructed vertex position to the nominal target position is small. These background events cannot be identified in a direct way. To estimate their contribution to the real event peak, two regions on the left and right sides of the target peak are selected with the implicit assumption, that background events have a smooth distribution of the vertex position around the target peak. The selection of event samples used for the determination of the amount of background events under the target peak is shown in the right panel of figure 4.1. The selected range in  $z$  position on both sides of the peak, indicated by the shaded area in the figure, is half of the cut range of the peak to avoid normalisation problems. Similarly, i.e. assuming that the distribution of the background is smooth around the target peak, the contribution of the background events to the pion multiplicity is determined too (see section 4.8.1). In the  $vx, vy$ -plane the background events are not distinguishable from real events.

### 4.4 Determination of the Impact Parameter $b$

In principle, any quantity which scales monotonously with the impact parameter, can be used for determining  $b$ . One observable that fits this requirement is the multiplicity of charged particles per event. The multiplicity of charged particles is expected to rise with increasing centrality and decreasing impact parameter  $b$  [Cavata et al., 1990]. This gradual increase of the multiplicity is a consequence of the fact that the reaction is more violent for more central events. For derivation of the impact parameter, the cross section per multiplicity bin has to be known. The total cross section is then obtained by integrating the multiplicity spectrum from  $mul = \infty$  to  $mul = 0$ . In order to have the broadest range of multiplicities for all systems the minimum bias (plus CDC) trigger is used. Depending on the main goal of the experiment, the various trigger conditions may be additionally suppressed in comparison to the central trigger. The suppression leads to different down scale factors  $dscal_{trig}$ , which depend on the respective trigger. This factor is

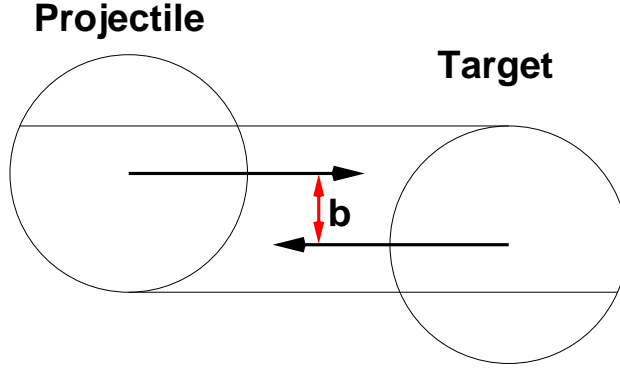


**Figure 4.2:** Reaction geometry of two colliding nuclei. The impact parameter is indicated.

hardware-wise chosen in a device called trigger-box, TB8000. In addition, a second factor accounting for the dead-time of the data acquisition system,  $dscal_{dead}$ , has to be introduced.

- down scale due to detector dead-time:  $dscal_{dead} = N_{inhibited} / N_{raw}$
- down scale in the trigger box:  $dscal_{trig} = N_{accepted} / N_{inhibited}$

with  $N_{raw}$  denotes all events which passed the trigger-box,  $N_{inhibited}$  is the number of events which did not take place during the dead-time of the DAQ, but still before the decision of the trigger box, and  $N_{accepted}$  stands for all accepted and, therefore, stored events.

The absolute cross section for a given trigger  $trig$  is then given by:

$$\sigma_{obs,trig} = \frac{1}{N_{beam} N_{target}} \cdot \frac{N_{obs,trig}}{dscal_{dead} dscal_{trig}}, \quad (4.1)$$

while  $N_{beam}$  denotes the number of beam particles (given by the start counter),  $N_{target}$  the number of target particles per unit area and  $N_{obs,trig}$  the number of observed events of a given trigger. Technically, all the mentioned numbers are counted using fast scalers and stored on tape after every beam spill.

Using the sharp cutoff model, the observed cross section  $\sigma_{obs,trig}$  can be related to the impact parameter:

$$\sigma_{obs,trig} = \pi b^2. \quad (4.2)$$

The expression above makes use of the geometrical interpretation of the cross section as being an effective area. The beam energy range examined here is well above the Coulomb threshold; therefore, the geometrical interpretation is valid.

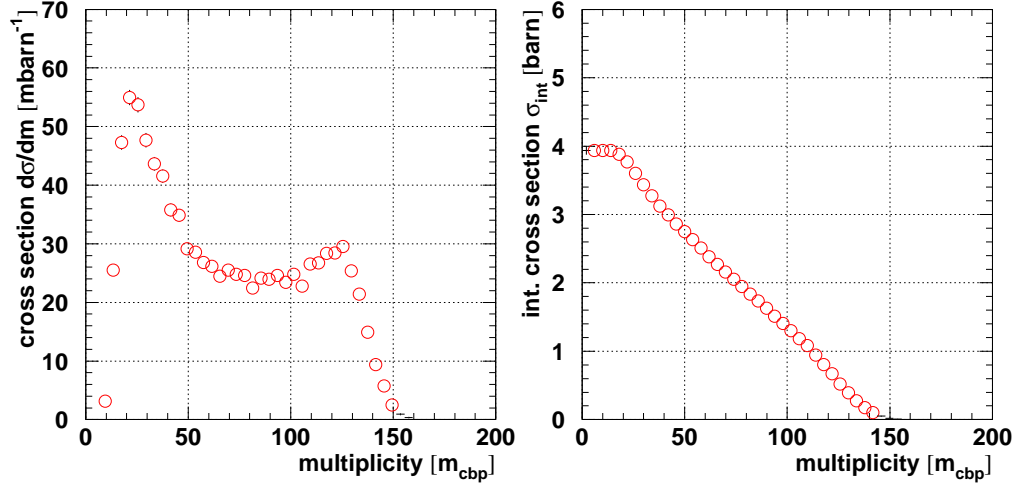


**Figure 4.3:** Integration of multiplicity spectrum  $\frac{d\sigma}{dm}$  (left panel) from  $-\infty$  to 0. The integrated cross section  $\sigma_{int}$  is given on the right panel. [Au + Au @ 1.0GeV]

The left panel of Figure 4.3 shows the differential cross section,  $\frac{d\sigma}{dm}$ , versus the multiplicity for the Gold system at a beam energy of 1.0GeV. The integration of this spectrum from  $-\infty$  to 0 gives the observed reaction cross section. On the right panel of Figure 4.3, the values of the integrals from  $-\infty$  to certain multiplicities are shown. Therefore, the plotted dependence has to be read as follows:

$$\sigma_{int}(mul) = \int_{\infty}^{mul} d\sigma(mul')dmul'. \quad (4.3)$$

The total cross section  $\sigma_{int}(0)$ , calculated in this way, is of the order of 4 barn. Geometrically, using the sharp cutoff model, a cross section for this reaction of  $\sigma = 1.22A^{\frac{1}{3}} = 6.15$  barn is expected. Clearly a certain part of the cross section must be missing in the measurement of this reaction. This loss occurs in the low multiplicity region and is due to a trigger bias which can not be avoided. The determination of the impact parameter for these peripheral events is not possible. In the considered example of the Gold on Gold reactions, this leads to a maximal accessible impact parameter of  $b_{max} = 11.28$  fm according to the sharp cutoff model. More peripheral events with  $b > b_{max}$  could not be detected in the experimental conditions of the measurements. Since surface effects smear the impact parameter determination, it can be stated that 20% of the cross section is missed for peripheral reactions.

From the knowledge of the impact parameter, the number of nucleons participating in a reaction is deduced as described in the following section.

## 4.5 Determination of $A_{part}$

The number of participating nucleons,  $A_{part}$ , is the number of nucleons in the target nucleus and the incoming beam ion which collide with each other during the reaction. This definition originates from a geometrical interpretation: the participating nucleons are the ones which are located in the geometrical overlay region of the colliding nuclei. Mathematically it is the volume of an intersection of a sphere with a cylinder (for one nucleus). Since the diffuseness of the nuclei is disregarded, this concept is called the sharp cut off model. In [Gosset et al., 1977] the general formulas are given for asymmetric reactions in the following form:

$$N_T = A_T F(v, b^{(0)}) \quad \text{with } v = \frac{R_T}{R_P + R_T} \quad \text{and} \quad b^{(0)} = \frac{b}{R_P + R_T}. \quad (4.4)$$

where  $b^{(0)}$  denotes the reduced impact parameter ( $b^{(0)} = \frac{b}{b_{max}}$ ) and  $R_T$ ,  $R_P$  the radii of the target and the projectile nucleus, respectively.  $N_T$  represents then the participants from the target nucleus. In the case of  $R_P$  greater than  $R_T$ , the function  $F(v, b^{(0)})$  reads:

$$F(v, b^{(0)}) = \frac{3}{4}(1-v)^{1/2} \left( \frac{1-b^{(0)}}{v} \right)^2 - \frac{1}{8} [3(1-v)^{1/2} - 1] \left( \frac{1-b^{(0)}}{v} \right)^3. \quad (4.5)$$

Since all reactions examined in this work are mass symmetric reactions,  $R_P$  and  $R_T$  are identical. In such a case, the number of participants,  $A_{part}$ , is calculated using the following expression:

$$A_{part} = A_{tot} F(1/2, b^{(0)}). \quad (4.6)$$

Here  $A_{tot}$  is the total number of nucleons in the system. Figure 4.4 shows the dependence of  $A_{part}$  on  $b$  calculated for all considered reactions.

For the calculation of  $A_{part}$  it is essential to know the impact parameter,  $b$ , directly. However, it requires determination of a quantity which is not under the control of the experimentalist. Note, that one is not able to “aim” at a nucleus with another one.

Since, as discussed in section 4.4, there is a maximal resolvable impact parameter, there exist as well a lower limit of the number of participating nucleons that can be determined.

## 4.6 Multiplicity Spectra

Within the FOPI setup, charged particles are measured by different sub-detectors as discussed in chapter 2. This implies that different techniques are used to count

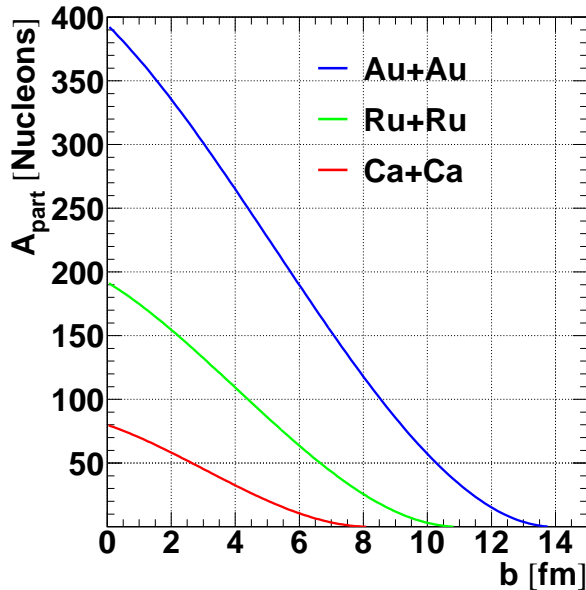


**Figure 4.4:** The number of participating nucleons,  $A_{part}$ , as a function of impact parameter  $b$  as calculated with equation 4.6 for the three considered reactions  $^{197}\text{Au} + ^{197}\text{Au}$ ,  $^{96}\text{Ru} + ^{96}\text{Ru}$  and  $^{40}\text{Ca} + ^{40}\text{Ca}$ .

charged particles in different regions of phase-space. As discussed in section 4.4, the particle multiplicity gives a handle on the determination of the impact parameter. However, it turns out that different multiplicity observables lead to different impact parameter measurements and, therefore, different  $A_{part}$ -axes.

Three different multiplicity variables are introduced to check how the selection of the observable used for the  $A_{part}$ -determination can influence the measurement of pions.

One of the considered multiplicities is the particle multiplicity in the forward wall,  $m_{ptrk}$ . The particle number is simply the number of hits registered in the scintillator material. The second observable is the number of tracks detected with the CDC,  $m_{ctrk}$ .  $m_{ctrk}$  is equal to the number of found tracks. No further selection on particle-species or other track-parameters is performed. The third considered multiplicity, namely  $m_{cbp}$ , is the baryon multiplicity, detected with the CDC plus the plastic wall hit count,  $m_{ptrk}$ . Only CDC tracks within the cut criteria, e.g. baryons originating from the primary vertex, which are described later, are taken into account. For example, pions detected in the CDC as being mesons, i.e. particles produced in the reaction, are discarded from  $m_{cbp}$ .

All multiplicity observables described above are determined for each event. The resulting particle multiplicity distributions obtained in the case of the reaction  $\text{Au} + \text{Au}$  @ 1.0 AGeV are plotted in figure 4.5. The contribution of background events is indicated by the red shaded area in 4.5. Low multiplicity events are more strongly contaminated by background, whereas no background is present in the case of high multiplicities. For the lowest multiplicities the background con-

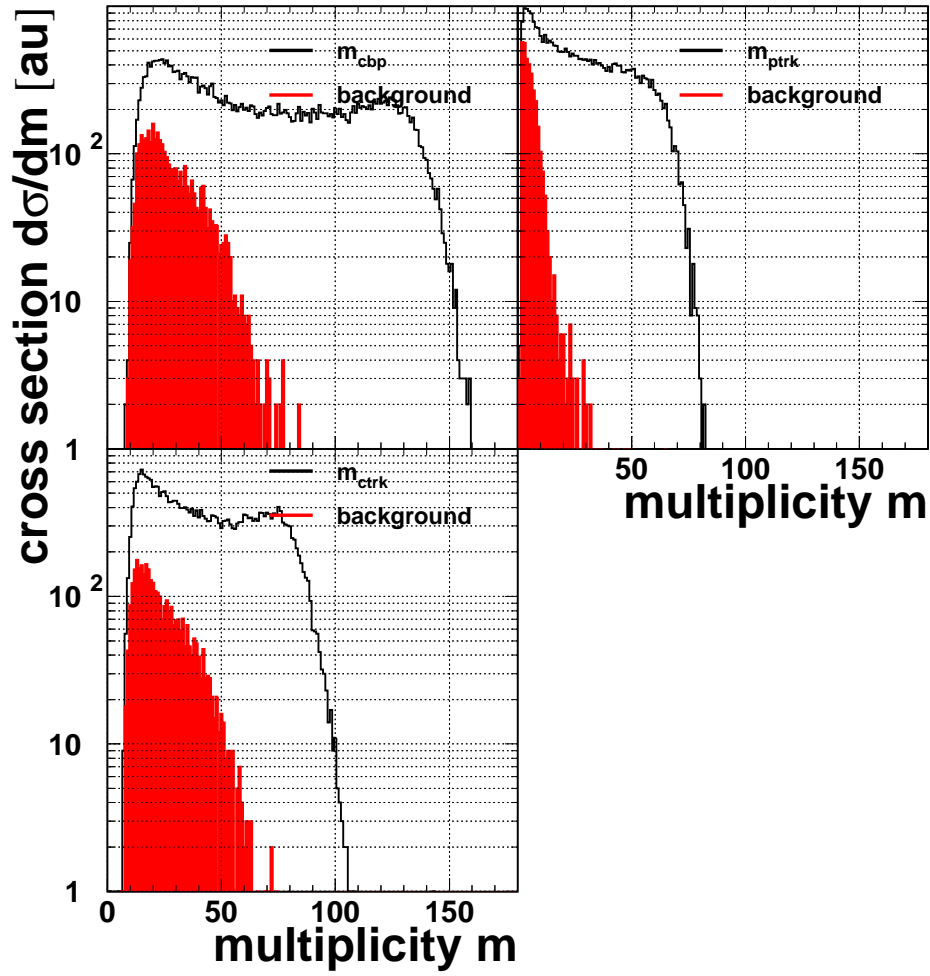


**Figure 4.5:** Different multiplicity  $m_i$  spectra for the reaction  $Au + Au @ 1.0 AGeV$ .  $m_{cbp}$  denotes the CDC baryon multiplicity plus the plastic wall multiplicity. The plastic wall multiplicity  $m_{ptrk}$  and the CDC track multiplicity  $m_{ctrk}$  are shown too. Background events are shown as the red shaded histogram.

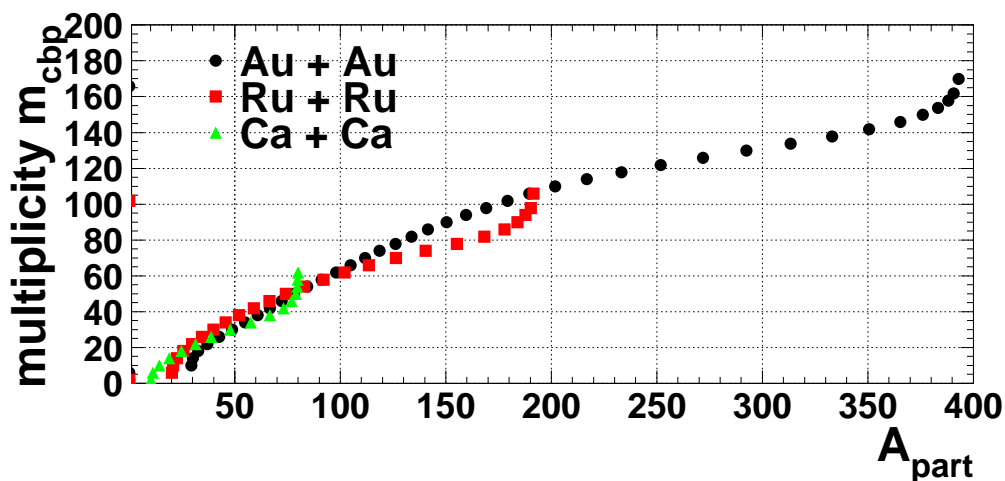


**Figure 4.6:** Correlation between multiplicity and  $A_{part}$  for 1.0 AGeV for the three reaction systems Calcium, Ruthenium and Gold.

tamination is in the order of 16% in the CDC ( $m_{ctrk}$ ) and above 60% for the plastic wall ( $m_{ptrk}$ ). This observation can be explained by taking into account the origin of background events. The Au–nuclei collide with light nuclei of the material that is present close to the beam flight path, i.e., C, O, and He from the scintillator material of the various beam detectors, capton foils and the Helium environment surrounding the target. The reaction products are emitted preferentially in the forward direction with a small opening angle due to the inverse kinematics (a heavy on a light nucleus). Since  $m_{cbp}$  is a mixture of both variables the effect is smeared out and the background contribution is in the order of 35%. The contribution of identified background events to the number of pions is described in section 4.8.1 on page 51.

As discussed in section 4.4 and section 4.5, the charged particle multiplicity can be linked to the impact parameter and, hence, to the number of nucleons participating in the reaction. Exemplarily, figure 4.6 shows the connection between the measured multiplicity  $m_{cbp}$  and the calculated number of participants  $A_{part}(b(m_{cbp}))$ . The three curves displayed in the figure correspond to the three considered colliding systems at an energy of 1.0 AGeV. According to the different system sizes, the derived maximum values of  $A_{part}$  are 80, 192 and 394 in the case of  $^{40}\text{Ca} + ^{40}\text{Ca}$ ,  $^{96}\text{Ru} + ^{96}\text{Ru}$  and  $^{197}\text{Au} + ^{197}\text{Au}$ , respectively. The shape of all three curves are identical. Moreover, particle multiplicities corresponding to the same  $A_{part}$  are found to be different by only 20% for all three systems. It is common to all reactions that for low numbers of participants the determination of

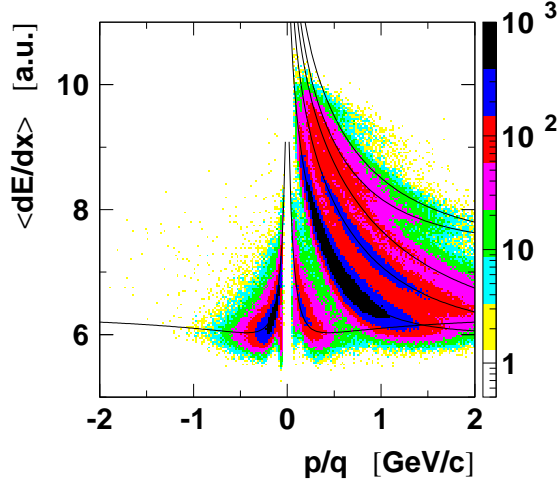


**Figure 4.7:**  $\langle dE/dx \rangle$  as a function of momentum over charge  $\frac{p}{q}$ . Negative momenta correspond to negatively charged particles and are plotted in order to discriminate  $\pi^-$  from  $\pi^+$ . The lines are drawn according to formula 2.2. No track selection cuts [ $Au + Au$  @ 1.0 AGeV].

the impact parameter is not possible due to the unmeasured part of the cross section (see section 4.4). Similar features are observed for the other energies as well. In addition, these findings are independent on the method used for the determination of  $A_{part}$ . The computation of  $A_{part}$  from  $m_{ptrk}$  and  $m_{ctrk}$  leads to observations similar to those displayed in Figure 4.6.

Differences are the sizes of the spectators: Central  $Ca + Ca$  reactions, with  $A_{part} > 60$  and with almost negligible spectator matter around, are expected to differ from the  $Au + Au$  system with  $A_{part} \approx 60$ . In the case of the Gold system, the spectators have the size of around 220 nucleons. Whereas Ruthenium reactions with  $A_{part} \approx 60$  are almost in the semi-central region.

## 4.7 Pion Identification

As shown in the following section 4.8, when the geometrical acceptance of the CDC is reflected with respect to the mid-rapidity, only a small fraction of the pion phase space distribution remains unmeasured for mass symmetric systems. Therefore, pions identified in other FOPI sub-detectors are discarded, and the pion identification is based on the information from the CDC only. Pions are identified in the CDC via the dependence of the mean energy loss per flight-path  $\langle \frac{dE}{dx} \rangle$  as a function of the momentum  $p$ . The lines in figure 4.7 represent the Bethe-Bloch parameterisation (equation 2.2, page 11) for the different particle masses. For every entry (particle) in this matrix a mass is calculated. The mass spectrum derived in this way is shown in figure 4.8. The mass assigned to the particle in this way is called the CDC-mass. All particles with a CDC-mass less than  $0.4 GeV$  are regarded to be pions.

For momenta larger than  $600 MeV/c$  the distinction of  $\pi^+$  mesons from pro-

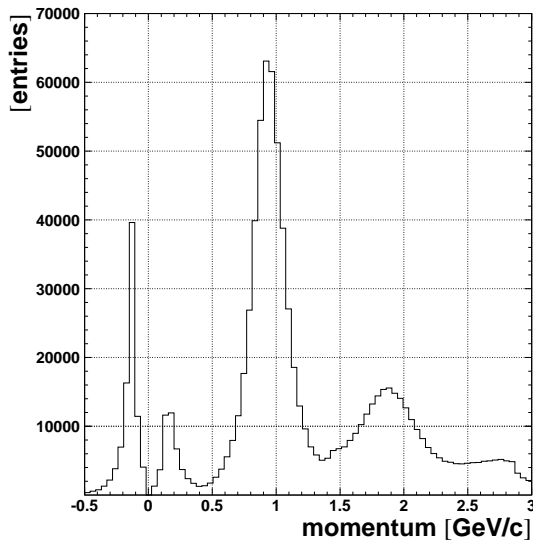


**Figure 4.8:** Mass distribution of the CDC determined from the Bethe-Bloch parameterisation of  $\langle dE/dx \rangle$  for the mass region below 2 GeV. [Au + Au @ 1.0 AGeV]

tons based on the  $\langle dE/dx \rangle$  information is problematic. The  $\pi^+$   $\langle dE/dx \rangle$  starts to rise<sup>2</sup> and tends to cross the proton  $\langle dE/dx \rangle$  line. Above this momentum a  $\pi^+$  is not distinguishable from a proton. As a consequence, all positively charged particles with a momentum above 600 MeV are considered to be protons and are disregarded when pions are counted.

Moreover, the Bethe-Bloch parameterisation has the same minimum for all particles. The energy loss at this minimum corresponds to the energy loss for minimum ionising particles, MIPs. Therefore, some tracks of which the  $\langle dE/dx \rangle$  is smaller than this value may not be well identified. Since most of the pions are mostly MIPs, this is a serious problem when their multiplicities are determined. Additionally pions are preferentially emitted with low momenta and have a certain possibility to curl in the CDC. Curled pions may be counted twice.

As shown in the section 4.7.1, the effect of these experimental difficulties are observed, for example in the distance to vertex distribution of pions. The double counting is taken into account automatically using the correction described in section 4.9.

### 4.7.1 Distance to Vertex

As discussed in section 4.7, particles are identified by curvature and energy loss of a track. Other parameters determine the track quality and, hence, the quality of the particle identification. These parameters are: hit-multiplicity per track, chi-squares showing the quality of the fit through the points assigned to a track, and

<sup>2</sup>Relativistic rise, after the minimum for the MIPs.

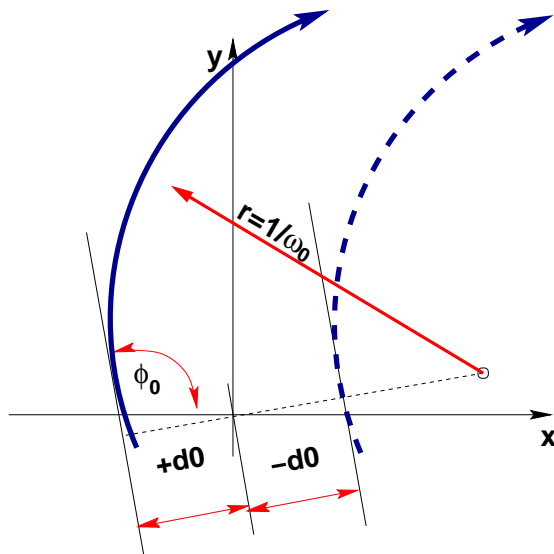


**Figure 4.9:** Definition of the  $d0$  parameter. Two tracks are indicated by the arrows. The sign of  $d0$  is defined as illustrated.

the distance of the individual track to the primary vertex  $d0$ . Here,  $d0$  is used to reduce pion background due to "fake" tracks, e.g. pions spiralled in the CDC and tracks not originating from the target.

The distance of a particle track to the primary event vertex,  $d0$ , is influenced by the fitting method [Billoir, 1984], [Karimaki, 1998].  $d0$  is defined in the  $xy$ -plane, which corresponds to the cross section of the CDC in figure 2.2, and denotes the shortest distance at which the particle trajectory approaches the reconstructed reaction vertex. As illustrated in figure 4.9, a sign is assigned to this distance  $d0$  as well. The  $d0$ -quantity yields a possibility to identify fake tracks, i.e. mirror track. The two histograms in figure 4.10 show the total  $d0$ -distribution for pions, in which the mirror tracks manifest themselves in a second peak only for positively charged pions. Mirror tracks, observed in the  $\pi^+$ -case, generate a peak of  $d0$  values between  $-15\text{cm}$  and  $-10\text{cm}$ . For  $\pi^-$ -mesons no such structure can be observed, since the environment for truly counterclockwise bent particles is much cleaner<sup>3</sup>.

In former data summary tape (DST) generations, tracks with a  $|d0|$  less than  $0.5\text{cm}$  were refitted once more when the position of the event vertex was determined. In this additional fit, the position of the event vertex was included as a track point with a very high weight. The free fit was not available anymore on the DST, consequently in some analysis only refitted tracks were taken into account [Hong et al., 1997]. This strategy is now changed in a way that both sets of track parameters, the ones before the refitting was done and the refitted ones, are available for each identified particle trajectory. It turns out that the spread of the

<sup>3</sup>Negatively charged particles compare section 2.1

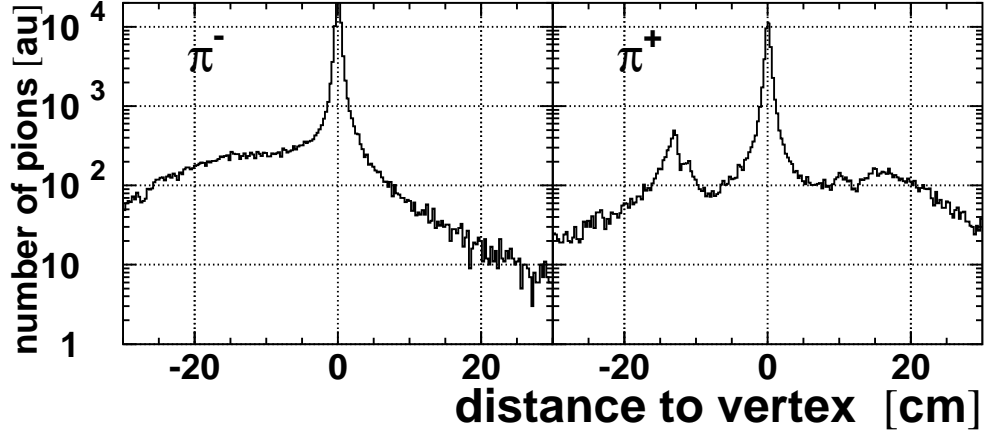


**Figure 4.10:** Distance to vertex distribution for  $\pi^-$  and  $\pi^+$  mesons. The  $d0$ -distribution of  $\pi^+$  shows a double peak structure indicating misidentified mirror tracks while the  $\pi^-$  distribution does not show this structure. [ $Au + Au$  @ 1.0GeV]

distance to vertex of tracks depends on  $p_{\perp}$ . The upper panel in figure 4.11 shows the dependence of the  $d0$  parameter on the transverse momentum  $p_{\perp}$ . The distribution gets narrower for larger  $p_{\perp}$ . To quantify this behaviour  $d0$  distributions for consecutive  $p_{\perp}$ -bins were fitted with a Gaussian-function. In the second panel of figure 4.11, the widths,  $\sigma_{d0}(p_{\perp})$ , of these Gaussians are shown as a function of  $p_{\perp}$ . The former stringent cut of  $|d0| < 0.5$  cm is marked as a black line in figure 4.11. As an example, at  $p_{\perp} = 100$  MeV/c, 33% of all  $\pi^-$ -tracks were rejected by the  $d0$ -cut in earlier analysis. This bias is removed in the current analysis of the data.

Equation 4.7 gives the functional behaviour of the widths  $\sigma_{d0}(p_{\perp})$

$$\sigma_{d0}(p_{\perp}) = P1 + P2 \cdot \frac{1}{p_{\perp}^2}. \quad (4.7)$$

For illustration, the fit of this form is included in figure 4.11. The fit-range is indicated by the red line and the extrapolation according to the fit results is depicted with the dashed black line. The parameter sets  $P1$  and  $P2$  for the different systems are collected in the tables C.1, C.2, C.4 (appendix C page 101). As an excerpt of these tables, the fit parameters obtained in the case of the Gold system at 1.0 AGeV are listed in tabular 4.2. Both, data and simulation (described in section 4.9.1), show the behaviour displayed in figure 4.11. The parameter  $P1$  gives the limiting value of the accuracy with which the distance to the primary vertex is

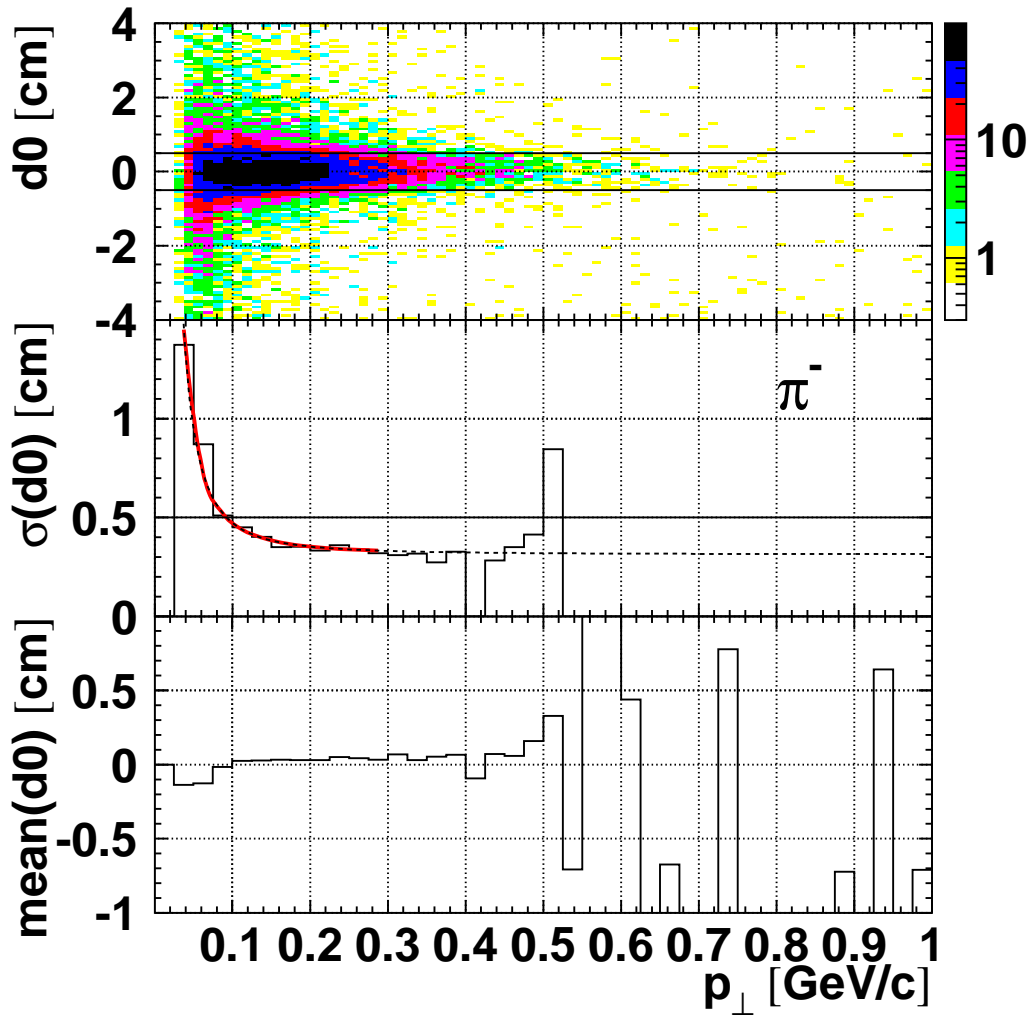


**Figure 4.11:** Distance to vertex  $d0$  for  $\pi^-$  mesons. Upper panel: two-dimensional distribution of  $d0$  as a function of  $p_{\perp}$ . Middle panel: the widths of  $d0$  in  $p_{\perp}$  slices as a function of  $p_{\perp}$ . The red line represents a fit to this dependence. Lower panel: the mean of the  $d0$  distribution. The former 0.5 cm cut is indicated in the two upper panels as well. [Au + Au @ 1.0 AGeV]

	particle	$P1$	$P2$
$Au + Au$ 1000AMeV GEANT	$\pi^-$	0.18455	0.0012884
	$\pi^+$	0.17667	0.0055900
	protons	0.14031	0.0098014
$Au + Au$ 1000AMeV experiment	$\pi^-$	0.26679	0.0020516
	$\pi^+$	0.23042	0.0037760
	protons	0.16034	0.013694

**Table 4.2:** Distance to vertex parameter used for the cut definition. The fit results are shown for experiment and simulation. [ $Au + Au$  @ 1.0 AGeV]

determined. This value is reached for trajectories of particles with high transverse momenta. The value of the  $P1$  parameter determined for the distribution of tracks of identified pions is, in general, larger by about 25% than that of proton tracks. This holds for both the experimental data and the simulations. The  $P1$  values obtained for positively and negatively charged pions differ by not more than 10%. The observations above are true for all measured systems and energies.

As a cross-check, the third panel of figure 4.11 shows the variation of the location of the mean value of the Gaussian fit. The peak position is located around zero for charged pion. For protons this quantity is shifted for low  $p_\perp$  tracks to negative values and approaches zero at a transverse momentum on the order of 0.15 GeV.

With this parameterisation it is possible to introduce a  $d0$ -cut which is dependent on  $p_\perp$ . Different cuts are considered to test the resulting corrections which are introduced in section 4.9.2. For example, a  $n\sigma$  cut is derived from equation 4.7 by multiplying the values of  $\sigma(p_\perp)$  with  $n$ . All pions with

$$|d0(p_\perp)| < n \times \sigma_{d0}(p_\perp) = n \times \left( P1 + P2 \cdot \frac{1}{p_\perp^2} \right) \quad (4.8)$$

are accepted in the analysis when a  $n\sigma$ -cut is used. Different values of  $n$  ( $n = 1, 3, 5$ ) are considered later in order to check the validity of the method with which the results are corrected (section 4.9).

The functional dependence of  $\sigma(d0)$  as a function of transverse momentum can be inferred from [Billoir, 1984] and [Groom et al., 2000]. The radius  $\rho$  of the track is related to the curvature  $k$  via the formula  $k = \frac{1}{\rho}$ . For a large number of hits ( $> 10$ ) the inaccuracy of the  $k$  determination,  $\delta k$ , is given by the resolution  $\delta k_{res}$  and an error introduced by multiple scattering  $\delta k_{ms}$ .

$$(\delta k)^2 = (\delta k_{res})^2 + (\delta k_{ms})^2 \quad (4.9)$$

where  $\delta k_{res}$

$$\delta k_{res} = \frac{\varepsilon}{L^2} \sqrt{\frac{720}{N+4}} \quad (4.10)$$

depends on the length of the measured trajectory in the  $xy$ -plane,  $L$ , and the error of the individual point measurement,  $\varepsilon$ .  $N$  is the number of measured points of the track. This error is independent of the transverse momentum and, therefore, not causal for the  $p_{\perp}$  dependence of  $\sigma_{d0}$ . The part of the measurement inaccuracy corresponding to the multiple scattering is described by the following equation:

$$\delta k_{ms} = \frac{(0,016)(\frac{GeV}{c})q}{L \cdot p_{\perp} \beta \sin(\Theta)} \sqrt{\frac{L}{x_0}}. \quad (4.11)$$

$\Theta$  denotes the emission angle in the lab frame,  $q$  the charge of the particle and  $x_0$  the radiation length of the detector gas.

Since  $\beta_{\perp} = \beta \sin(\Theta)$  and  $p_{\perp} = \beta_{\perp} \gamma m$ ,  $\delta k_{ms}$  is proportional to  $\frac{1}{p_{\perp}^2}$ .

## 4.8 Pion Acceptance and Pion Counting

As illustrated in figure 2.3 on page 14, the geometrical acceptance of the CDC spans the backward hemisphere of symmetric reactions in the centre of mass frame. The phase-space coverage of the CDC of selected charged pions is shown in figure 4.12. The representation is such that the transverse momentum  $p_{\perp}$  is divided by the pion mass to enlarge the scale in this direction. The left two panels are the CDC acceptance for  $\pi^{-}$  and  $\pi^{+}$ . The distribution is very broad and fills a large part of phase-space. In order to cover the whole phase-space the distribution is reflected with respect to  $y^{(0)} = 0$ . All measured pions with  $y^{(0)} > 0$  are disregarded. The reflection at  $y^{(0)} = 0$  is allowed since only mass symmetric reactions are considered. As already mentioned the positive pions are only identified with a momentum less than  $0.6 \text{ GeV}/c$ . This upper momentum limit is visible in the phase-space populated by the identified  $\pi^{+}$  at scaled rapidities larger than 0. However, when the measured distributions are reflected with respect to  $y^{(0)} = 0$ , this limit becomes irrelevant.

Applying this concept, the pions are counted event-wise in one phase-space hemisphere and the other side of the phase space is reconstructed by mirroring with respect to  $y^{(0)} = 0$ . This leads to an acceptance hole at low transverse momentum at mid-rapidity. The correction proposed in section 4.9.2 compensates this effect.

The evolution of pion multiplicities with increasing particle multiplicity of the events is shown in figure 4.13. This figure shows the two dimensional distribution of pions (left  $\pi^{-}$ , right  $\pi^{+}$ ) as a function of charged particle multiplicity  $m_{cbp}$ . The

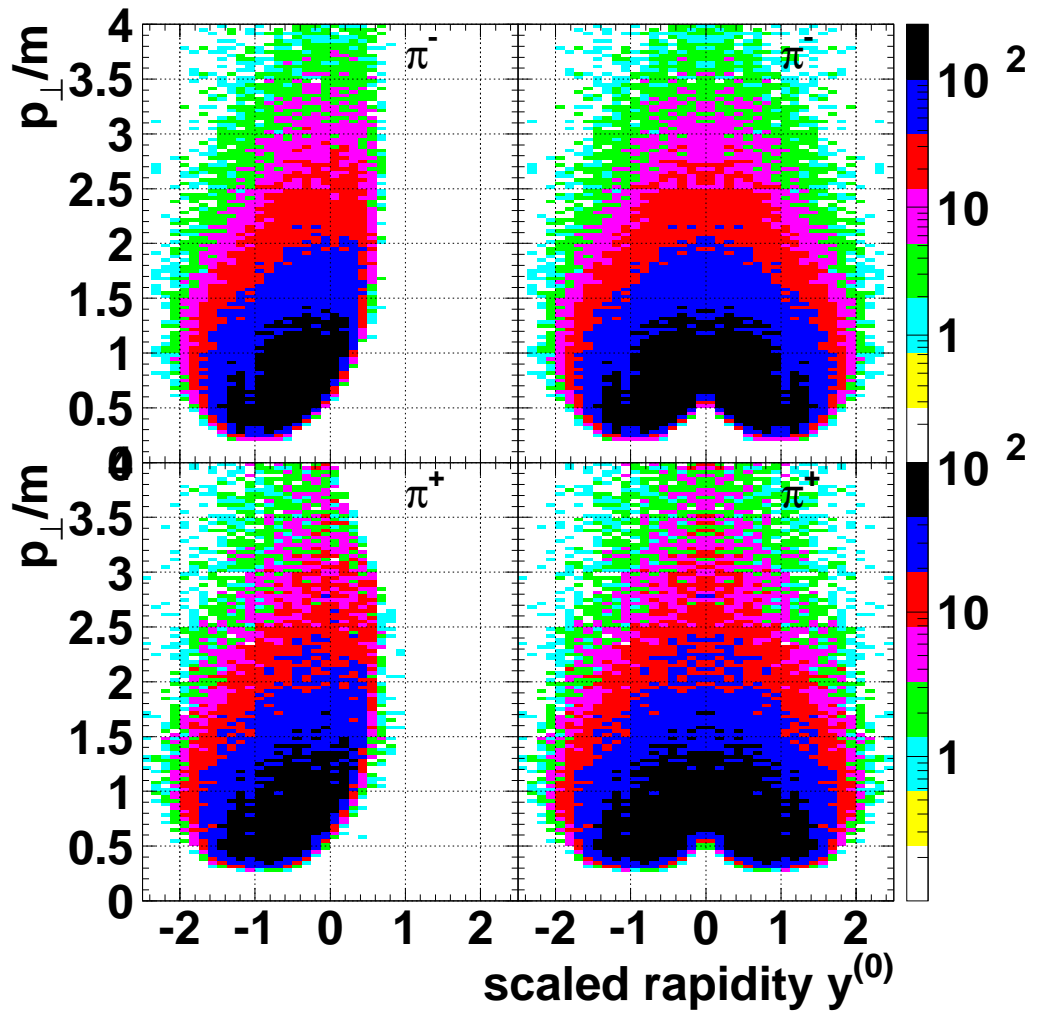


**Figure 4.12:** Acceptance of the CDC for pions ( $\pi^{-}$  upper and  $\pi^{+}$  lower two panels). Left: the measured phase-space distributions of pions. Right: phase-space distributions after reflection with respect to mid-rapidity. Losses at  $y^{(0)} = -1$  are due to absorption of pions in the target. [Au + Au @ 1 AGeV]

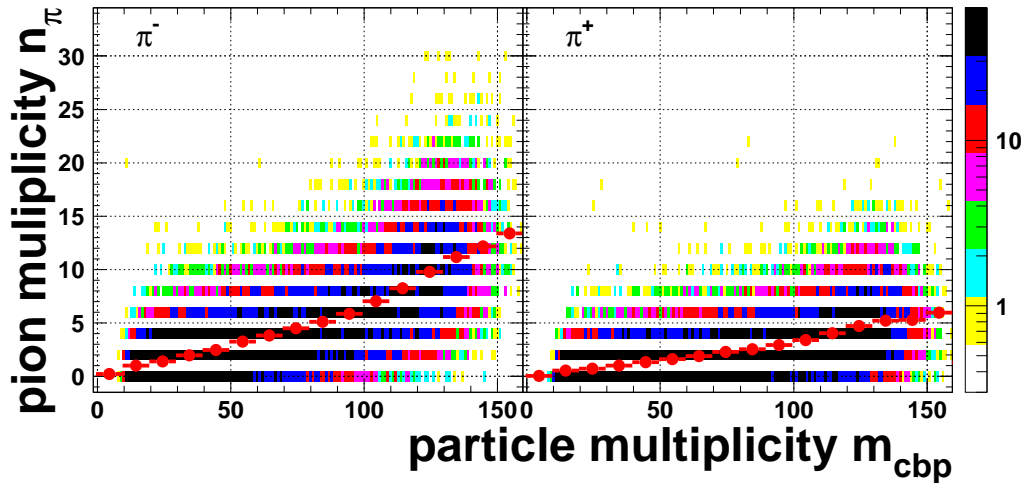


**Figure 4.13:** Pion multiplicity as a function of  $m_{cbp}$ . The red dots depict the mean values for events of a given  $m_{cbp}$ . The structure of the scatter plot is an artifact due to the acceptance correction of the  $\pi$ -multiplicity, e.g. by multiplying the measured  $\pi$ -multiplicity with a factor of two.

red dots symbolise the mean of the distribution. The pion multiplicity rises with the particle multiplicity of the event.

#### 4.8.1 Pion Background

As mentioned in section 4.2 on page 34, there is a certain contribution of the background events to the events with the nominal vertex position around the target. These events contribute to the pion multiplicities as well. To estimate the pion background contribution of these events, the background event selection of section 4.2 is used. The pions from background events have to be subtracted from the measured pion multiplicity in order to get the real number of pions. This has to be done for all chosen charged particle multiplicity variables. The pion multiplicity per event as a function of the different particle multiplicities is shown in figure 4.14. The selected background events are treated in the same way as normal events, in particular all cuts are the same for both event samples. The background events tend to have a lower particle multiplicity (which is already shown in section 4.2) and pion multiplicity at once (see figure 4.14). In the case of  $m_{ptrk}$ , pions stemming from the background events and those from events on target are indistinguishable in terms of pion multiplicity, even for events with particle multiplicities as high as  $m_{ptrk} \leq 20$ . For the particle multiplicities  $m_{cbp}$  and  $m_{ctrk}$  the

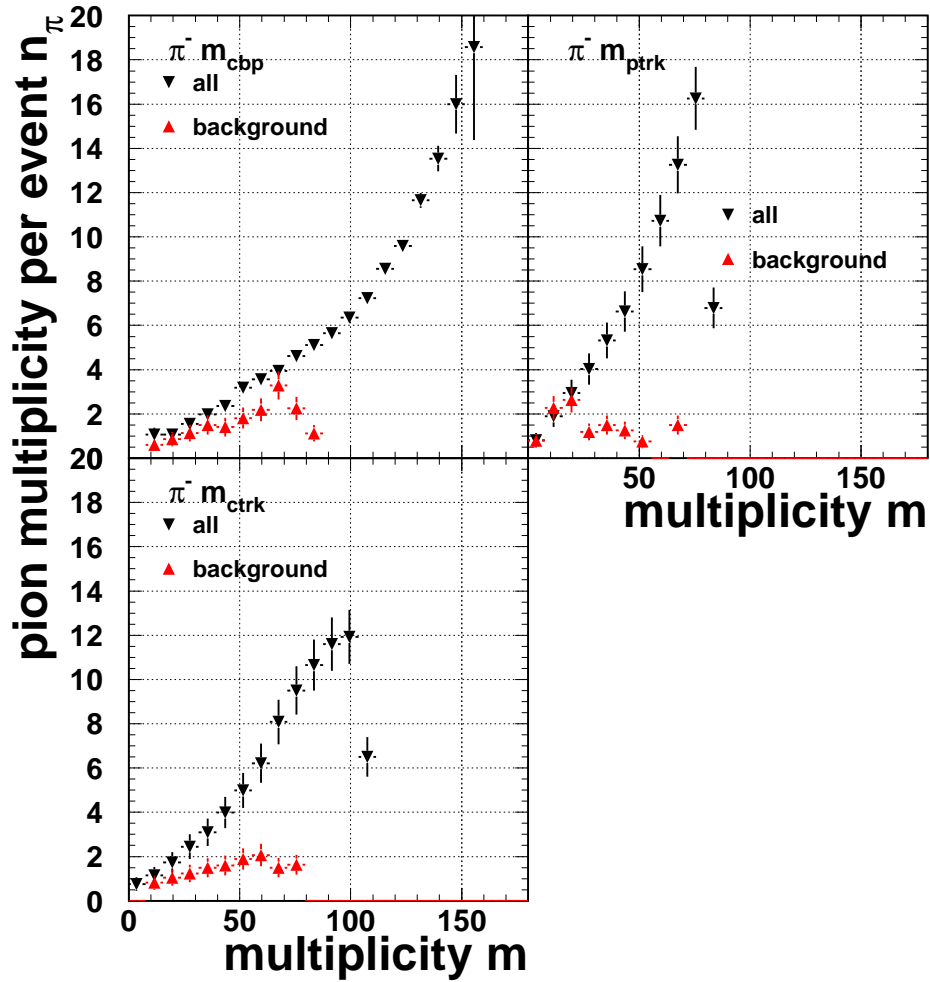


**Figure 4.14:** Pion ( $\pi^-$ ) multiplicity as a function of different particle multiplicities,  $m_{cbp}$ ,  $m_{ptrk}$ , and  $m_{ptrk}$ , introduced in section 4.6. Pions from non-target events are shown as the red triangles. [Au + Au @ 1.0 AGeV]

number of pions from background events is always smaller than the number of pions attributed to the events stemming from the target. All central events with a high number of charged particles are free of pion background. This observation is compatible with the explanations of the origin of background events given in section 4.6, namely that the background events stemming from collisions with light nuclei are forward focused and, therefore, most of their products are detected with the PLASTIC WALL.

Note that the pion multiplicities in figure 4.14 are not weighted with the number of events! In order to correct for the presence of the pions from background events, the properly weighted pion multiplicities are subtracted from the pion multiplicities measured in events that fulfil the appropriate selection criteria.

Since the real background under the event peak is not accessible directly, all background studies rely strongly on the assumption that the real background events have the same behaviour as the so-called background events selected in the regions close to the event peak in  $v_z$ -coordinate (see figure 4.1 on page 35).

No background events are included in the GEANT simulation discussed later. In that sense the determination of background is done intrinsic within the experimental data sample without using the simulation.

## 4.9 Pion Efficiency, Corrections

The basic idea of the following analysis is to have an "all inclusive" correction, which can be applied to the measured pion data. In addition, the correction should be as close to the final observable as possible. Since the functional dependence of the number of pions of the number of participating nucleons,  $A_{part}$ , is almost linear,  $A_{part}$  seems to be well suited for such corrections. The geometrical acceptance of the **FOPI**-detector is not perfect, a correction according to geometrical losses is necessary. The pion reconstruction efficiency which is not known a priori has to be corrected as well. The capability to identify charged pions with the CDC appears to be a function of track density, which, by itself, is a function of the global charged particle multiplicity, and, finally a function of  $A_{part}$ .

To determine the pion identification efficiency, simulations within the GEANT(3.21) environment are performed. As input for the simulations, i.e. as event generator, the results of the iQMD model are used<sup>4</sup>.

### 4.9.1 Monte Carlo Simulation of the Detector

The complete **FOPI**-detector setup is implemented in the GEANT simulation tool [Brun et al., 1987]. GEANT allows to simulate the detector response to a

---

<sup>4</sup>A brief introduction to the iQMD model is given in section 6.2 on page 85.

given stimulus, e.g. the passage of a particle. The simulation is based on the Monte Carlo method and in the following referred to as the MC simulation. Figure 2.1 on page 10 is in fact generated using the detector geometry defined in GEANT. In this paragraph the part of the GEANT-simulation is described which deals with the CDC.

The digitisation of the simulation output is done on the level of the energy loss along the particle trajectory. A particle from the event generator is propagated through the detector volume. The energy loss and, hence, the number of primary electrons along the trajectory are determined by the intrinsic GEANT routines. The charge collection on the sense wires is delayed by the time corresponding to the drift of the electrons in the chamber. The charge multiplication in the vicinity of the sense wire is parameterised to match the real detector properties. The shape of the signal induced on the wire is simulated realistically as well, including a smearing of the charge division, fluctuations and correlated noise. The functional modelling of these detector responses are derived from experimental detector data. All performed GEANT simulations made use of the same set of digitisation parameters, although the parameters were tuned to describe the Ruthenium experiment [Wiśniewski, 2000]. The processing of the digitised output of the simulation includes the subsequent front-end electronics functionality, i.e., scanning, zero suppression, and the reduction of the CDC data by the front-end algorithm (see section 3.2.2 on page 23). After this chain of simulation steps the output of the simulation has the same structure as the experimental data.

Therefore, the experimental data and the result of the MC simulation can be treated in the same way, e.g. the track-finding algorithm and the refitting strategies for tracks can be applied in the same fashion to both of them. In particular, all cuts and parameters of the tracking program that are used are in both cases identical.

As comparison of real and simulated data, in figure 4.15 the hit distribution, namely the number of hits along a track for a given particle, is shown. The histograms are normalised to the same area. Note that for negative pions the number of hits per track can exceed the number of wires in a CDC sector. 56 wires in each CDC sector were read out during all three experiments. This limit is not overcome by positively charged particles. It is exceeded in the case of negative pions, because negatively charged particles curl in opposite direction in the CDC. They cross sector borders more frequently than positive particles, and therefore, their tracks are made of a larger number of hits on average. The steps in the spectra shown in figure 4.15 are due to certain features of the track finding algorithm, and correspond to different stages in the track-search process. The maxima in the simulated pion spectra are at higher number of hits than those of the experimental spectra. This means that the simulated detector response is still cleaner than the response of the experimental device. However, the maximum uncertainty can be estimated by extrapolating the hit distribution to zero for zero hits is on the order of

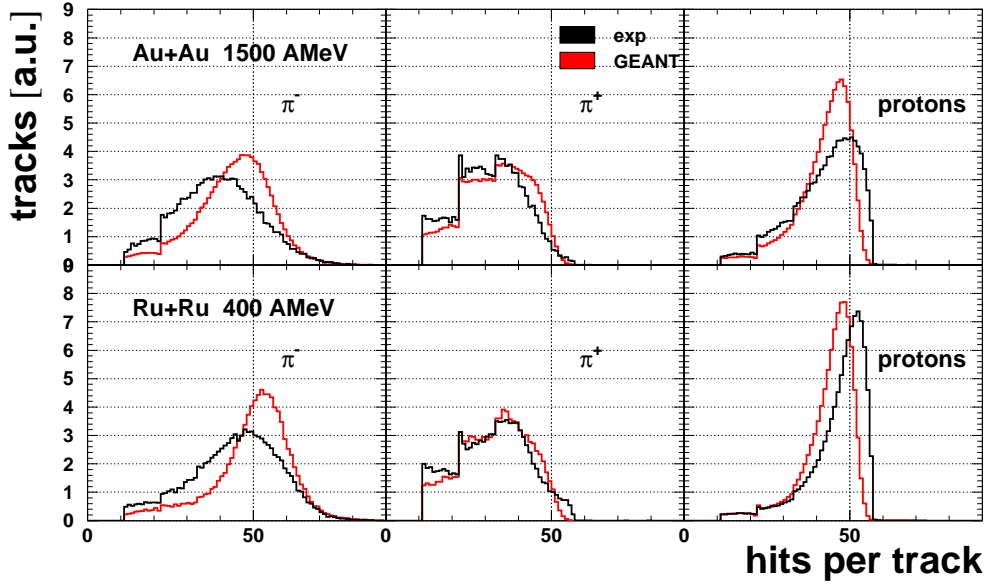


**Figure 4.15:** The distribution of number of hits a particle track consist of for different particle species.  $Au + Au$  @ 1.5 AGeV upper three panes and  $Ru + Ru$  @ 0.4 AGeV lower panels. The steps in the distribution are artifacts of the tracking algorithm and correspond to different stages of the track search. The histograms for experiment (exp) and simulation (GEANT) are normalised to the same area. No particle multiplicity cut is applied.

4% for  $\pi^+$  mesons and of 3% for the  $\pi^-$ , independent of the total hit-multiplicity in the chamber. To show the consistency in the MC-simulation the extreme cases of  $Au + Au$  @ 1.5 AGeV and  $Ru + Ru$  @ 0.4 AGeV are shown in figure 4.15. For the counting of pions the number of hits per track is not a crucial quantity since every pion is counted independent of the number of hits per track. In other words, the description of the detector response with the MC simulation is well enough to deduce a correction for the experimental data. The systematic error introduced by this discrepancy is, considering other sources of errors (compare section 4.12), acceptable.

Comparing the distance to vertex  $d_0$  distributions of experimental data and Monte Carlo in terms of the introduced transverse momentum  $p_\perp$  dependency (section 4.7.1 on page 44), the simulated detector response is also too accurate. To take this into account the cuts on  $d_0$  are individually applied to GEANT events and to experimental data adjusting to the same relative width expressed in multiples of the sigma of the  $d_0$ -distribution as introduced in section 4.7.1. The adjustments were done according to the derived fit parameters  $P1$  and  $P2$  (as given in the appendix C on page 101).

Since the input for the GEANT simulation arises from the iQMD model, the input for the simulation and the output from the simulation is known. A comparison between the input distributions and the outcome of the simulation gives access to more specific aspects of the overall detection efficiencies, like geometrical and tracking inefficiencies separately.

### 4.9.2 Global Correction Function with Respect to $A_{part}$

This correction is obtained by comparing pion multiplicities  $n_\pi$  as a function of  $A_{part}$ . Different contributions, namely geometrical and reconstruction efficiency, can be identified using the proper distributions from the different simulation stages. In the following, fully tracked Monte Carlo data is indicated by the superscript *MC*. The input of the GEANT simulation, which is the full  $4\pi$ -phase-space, is denoted by  $4\pi$  accordingly. In addition, a geometrical cut can be applied to the  $4\pi$  input. This introduces a particle selection to the phase-space accessible to the CDC. Particles are accepted if they are emitted into the geometrical acceptance of the CDC as given in table 2.1. A lower transverse momentum cut of  $p_\perp/m = 0.25$  ensures that only particles are selected, which can principally be detected by the CDC. The distributions obtained by filtering the iQMD events with this geometrical cut are indicated by *geo*.

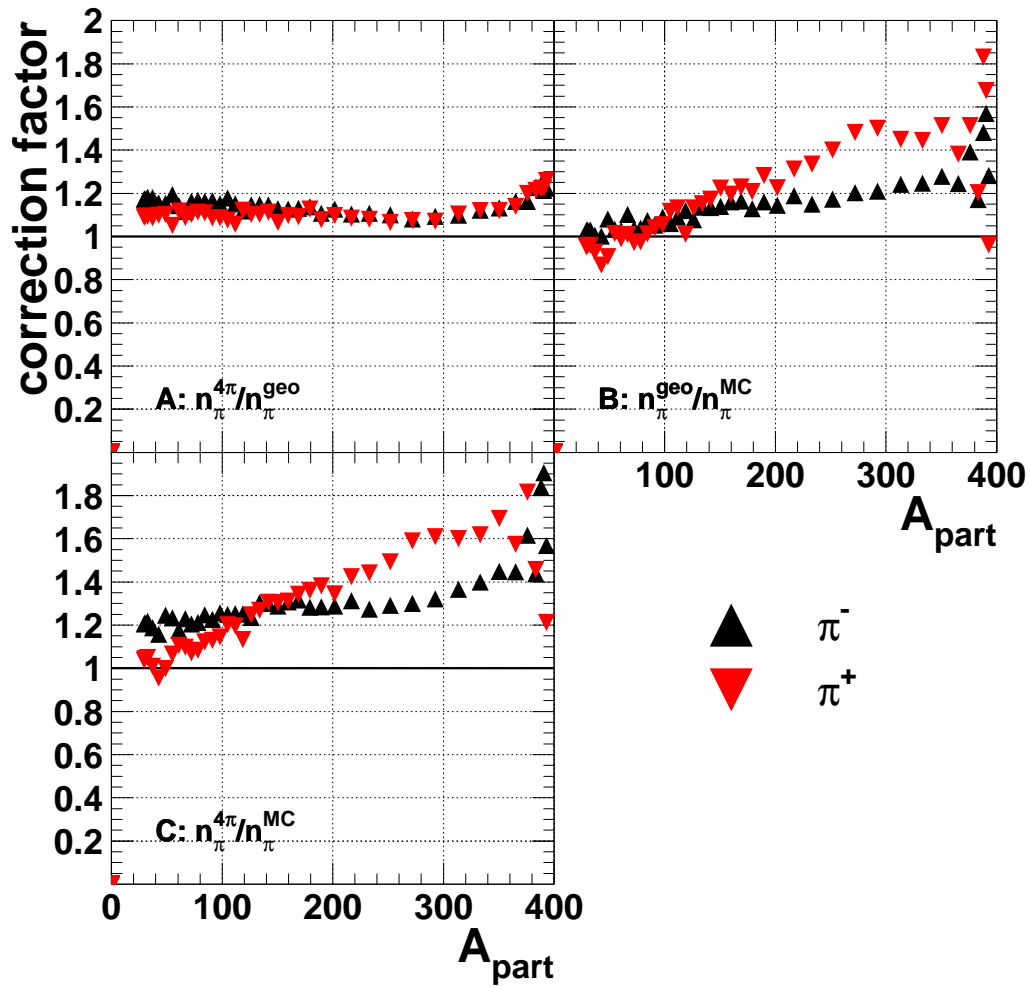
The  $4\pi$  input distribution for the pion multiplicity is the pure iQMD input and referred to as  $n_\pi^{4\pi}(A_{part})$ .  $A_{part}$  can be determined for this input distribution in different ways, namely from the known impact parameter given by iQMD, or indirectly, starting from the total charged particle multiplicity (or other multiplicities discussed already in this chapter). However, for a meaningful comparison of different  $A_{part}$  axes, only  $4\pi$  particle multiplicities filtered by the geometrical acceptance of the detector are used to determine  $A_{part}$ , i.e.,  $m^{geo}$  distributions are used instead of  $m^{4\pi}$  distributions.

Figure 4.16 summarises the different deduced corrections. To span a large range in the number of participants, the Gold system at an energy of 1.0 AGeV is chosen exemplarily. The following part of this section describes the various contributions to the "all inclusive" correction, e.g. the correction originating from the geometrical acceptance of the CDC or the one corresponding to the tracking efficiencies. By definition, the efficiency  $\varepsilon$  is related to the correction factor by the expression:  $c = \frac{1}{\varepsilon}$ .

The geometrical correction is shown in panel A of figure 4.16. Here, the input  $4\pi$  pion distribution,  $n_\pi^{4\pi}(A_{part})$ , is divided by the distribution obtained by filtering the input with the geometrical acceptance of the detector,  $n_\pi^{geo}(A_{part})$ <sup>5</sup>.

---

<sup>5</sup>Technically the spectra are interpolated by a spline function to account the different  $A_{part}$ -axis.



**Figure 4.16:** Determination of the corrections according to  $A_{part}$ . A: "Geometrical" correction. B: "Tracking" correction. C: Total correction. Representative for all systems the corrections for the Gold system at 1.0 AGeV are shown.

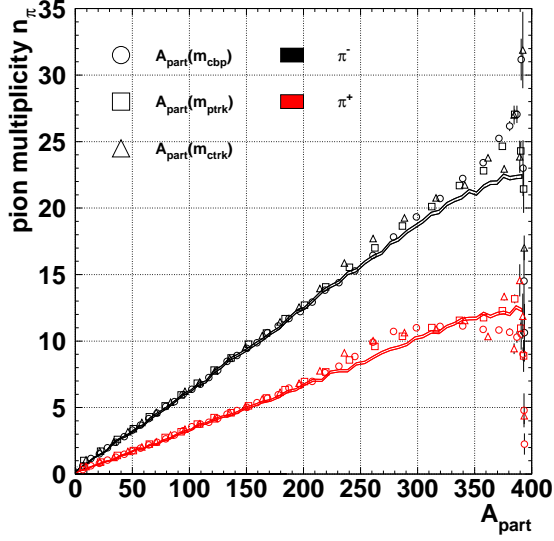


**Figure 4.17:** Consistency check of the determined functional dependence of the correction factors on  $A_{part}$ . Different symbols depict the pion multiplicities obtained when different particle multiplicities were used for the determination of  $A_{part}$ . The two lines denote the "input" to the GEANT simulation. In this case  $A_{part}$  is directly calculated from the impact parameter  $b$  of the iQMD events. [Au + Au @ 1.0 AGeV]

The correction factor

$$c_{geo} = \frac{n_{\pi}^{4\pi}(A_{part})}{n_{\pi}^{geo}(A_{part})} \quad (4.12)$$

is on the order of 1.1 which shows a geometrical efficiency of 90% and this correction is independent of  $A_{part}$  and the pion species. The tracking efficiency is shown in panel B of 4.16. Here, the ratio  $c_{track}$  of the distribution of particles filtered through the geometrical cut,  $n_{\pi}^{geo}(A_{part})$ , to the fully GEANT simulated and tracked distribution,  $n_{\pi}^{MC}(A_{part})$ , is plotted. This leads to the tracking correction:

$$c_{track} = \frac{n_{\pi}^{geo}(A_{part})}{n_{\pi}^{MC}(A_{part})}. \quad (4.13)$$

It turns out that the two charged pion species are tracked with different efficiencies. While the  $\pi^{-}$  meson correction function is almost constant as a function of  $A_{part}$ , the  $\pi^{+}$  meson correction rises with increasing numbers of participants.

The overall correction,  $c$ , is obtained by the comparison of the full  $4\pi$ -information  $n_{\pi}^{4\pi}(A_{part})$  to the final output of the GEANT simulation  $n_{\pi}^{MC}(A_{part})$ :

$$c = \frac{n_{\pi}^{4\pi}(A_{part})}{n_{\pi}^{MC}(A_{part})} = c_{geo} \cdot c_{track}. \quad (4.14)$$

Here, both effects are taken into account, i.e. the tracking inefficiency and the geometrical acceptance. The overall correction shows the same behaviour as a function of  $A_{part}$  as the tracking efficiency, since the geometrical correction is independent of  $A_{part}$ .

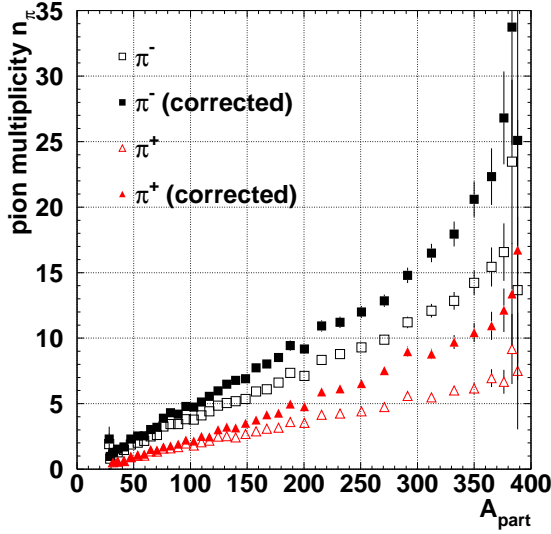


**Figure 4.18:** Corrected pion multiplicity spectra according to the direct  $A_{part}$  correction. The effect of the  $A_{part}$ -dependent correction on the pion multiplicity spectra. The open symbols depict the measured spectra (triangles  $\pi^+$ , squares  $\pi^-$ ). The filled symbols correspond to the corrected spectra. [ $Au + Au @ 1 \text{ AGeV}$ ]

In order to cross check the validity of the method, the distribution resulting directly from the input to the GEANT simulations,  $n_{\pi}^{4\pi}(A_{part}(b))$ , is compared to the results of the simulation corrected with the efficiency factors described above,  $n_{\pi}^{MC}$ . This is illustrated with figure 4.17. Here, the iQMD input,  $n_{\pi}^{4\pi}(A_{part}(b))$ , is depicted by the band.  $A_{part}$  is calculated directly using equation 4.6 with the impact parameter given by the iQMD model. All pions are included and no geometrical or kinematical selection conditions are applied. The Monte Carlo data,  $n_{\pi}^{MC}$ , is represented by the symbols. Different symbols correspond to results obtained when different particle multiplicities  $m_{cbp}$ ,  $m_{ptrk}$ , and  $m_{ctrk}$ , are used for  $A_{part}$  determination. The number of pions,  $n_{\pi}^{MC}$ , are corrected with the correction factors discussed before. All MC data points lay on top of the input, independently which particle multiplicity is used for the  $A_{part}$  determination, which validates the proposed correction method with deviations smaller than 5% up to an  $A_{part}$  of 320 nucleons. Beyond, the limited selectivity of the multiplicity variable disturbs the result.

Figure 4.18 illustrates the effect of the correction. The corrected and the uncorrected pion multiplicities are plotted as a function of  $A_{part}$ . The uncorrected pion data is depicted by open symbols. The “over all” correction is now applied to the measured data and the resulting pion multiplicities are shown with the filled symbols.

The slope of this distribution is later used to determine the pion yield 4.11. The effect on the slope is described shortly in the following. In the  $Au + Au$  system at 1.0 AGeV, the applied corrections change the slopes of the pion multiplicities with respect to the  $A_{part}$  axes by about 28% and 36% in the case of the negative and the positive pions, respectively. The influence of the correction is less pronounced

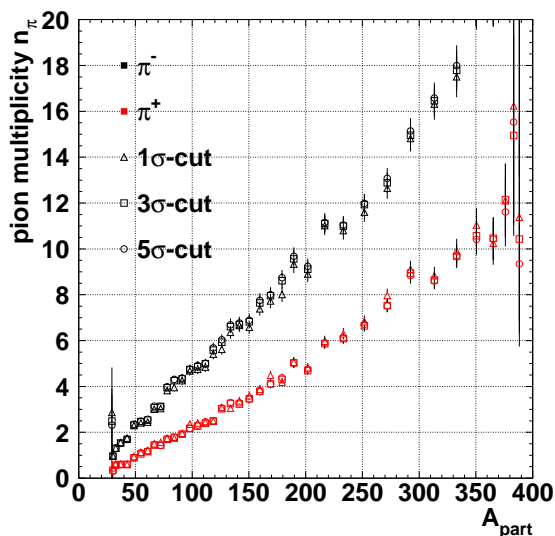


**Figure 4.19:** 1,3,5 $\sigma$ -cut detected pion pion multiplicities. The pion multiplicities coincide with each other perfectly. [Au + Au @ 1 AGeV]

in the Ruthenium system at 1.0 AGeV. Here, the slopes of the  $\pi^-$  and  $\pi^+$  meson multiplicity distributions change about 22% and 33%, respectively. In the case of the Calcium system, the correction changes the slopes by about 20% for both charged pion species.

The same situation is found at a bombarding energy of 1.5 AGeV for all three systems. This is changed at an energy of 400 AMeV, here the overall correction is independent of the number of participants and about 20%. The resulting overall change in the slope and therefore the number of pions per  $A_{part}$  is about 30% for all systems<sup>6</sup>.

The fit was restricted to a range  $0.15 < A_{part}/A_{sys} < 0.85$  in order to avoid distortions due to the impact parameter selectivity of the apparatus. This restriction ensures in addition that autocorrelations of the pion numbers are not influencing the determination of the slope.

The different cut conditions are tested by varying the the distance to vertex cut. Figure 4.19 shows the pion numbers as a function of participating nucleons,  $A_{part}$ . In this figure the  $A_{part}$ -axis is calculated using  $m_{cbp}$  in all three cases. The above described procedure of the correction is applied to pion data determined with 1 $\sigma$ , 3 $\sigma$ , and 5 $\sigma$ -cuts<sup>7</sup> on pion tracks. The resulting pion numbers are the same within 3%. No difference is found for the fits applied to get the mean number of pions per participating nucleon. The correction factors determined by the described method are changed according to the loss/gain of pions compared to the 3 $\sigma$ -cut. With this knowledge the 3 $\sigma$ -cut on the distance to vertex distribution is chosen as the standard cut.

<sup>6</sup>Note that it is always a free fit which is performed.

<sup>7</sup>Notation introduced in section 4.7.1.

In the course of this thesis an error was discovered in the detailed balance routine of the iQMD version used by the **FOPI** collaboration. This error lead to approximately 30% more pions than the correct iQMD calculation. The correction described in the above section is obtained with the old iQMD version. The correction is checked with the new iQMD version, and found to be stable and not connected to the number of pions in the simulation.

The corrected iQMD version is used in figure 6.5 to compare with the experimental data.

### 4.9.3 Correction Function According to Multiplicity

An alternative way to determine the correction described in the previous section, is to introduce a correction according to the charged particle multiplicity directly without the use of the calculated  $A_{part}$ -axis. With such a correction the pion multiplicities can be corrected as a function of charged particle multiplicity before the calculation of  $A_{part}$  from this particle multiplicity. The measured charged particle multiplicity<sup>8</sup>,  $m^{exp}$ , has to be related to the real multiplicity spectrum,  $m^{4\pi}$ . The real multiplicity distribution is not accessible, since only particles which are measured contribute to the measured multiplicity spectrum. However, in the case of the iQMD results and the GEANT simulation, the whole information is available, as stated in section 4.9.1. Here, the iQMD input  $m_{iQMD}^{4\pi}$  is simply regarded as being the not-measured, "real" multiplicity,  $m^{4\pi}$ . Similarly, the measured spectrum  $m^{exp}$  which can be identified with  $m^{MC}$ , i.e. the spectrum corresponding to the fully simulated GEANT events. In order to keep the notation simple, the sub- and superscripts will be omitted, and the "measured" observables are marked with (').  $n'_\pi$  will denote the number of pions and  $m'$  the particle multiplicity.

The following mathematical description shows the method of determining a correction as a function of the chosen multiplicity variable. Only the calculation concerning the multiplicity correction is shown.

The measured number of pions,  $dn'_\pi$ , per multiplicity bin,  $dm'(b)$ , is:

$$dn'_\pi = f_{n'_\pi}(m'(b))dm'(b) \quad (4.15)$$

where  $f_{n'_\pi}(m'(b))$  is the number of pions as a function of  $m'(b)$ .

The quantity which is not accessible in the experiment, but from which the measured one originates is:

$$dn_\pi = f_{n_\pi}(m(b))dm(b) \quad (4.16)$$

with the same notation.

---

<sup>8</sup>The multiplicity which is later on used to determine  $A_{part}$

The following equation shows how the real number of pions,  $n_\pi$ , and the real multiplicity,  $m$ , are related to the measured quantities:

$$\begin{aligned} dn_\pi &= f_{n_\pi}(m(b))dm(b) = f_{n'_\pi}(m'(b)) \frac{f_{n_\pi}(m(b))}{f_{n'_\pi}(m'(b))} dm(b) \\ &= \underbrace{f_{n'_\pi}(m'(b))}_{\text{measured}} \underbrace{\frac{f_{n_\pi}(m(b))}{f_{n'_\pi}(m'(b))} \frac{dm(b)}{dm'(b)}}_{\text{correction}} \underbrace{dm'(b)}_{\text{measured}}. \end{aligned} \quad (4.17)$$

This transformation includes the introduction of a correction factor which consists of a ratio of pion multiplicities,  $f_{n_\pi}(m(b))/f_{n'_\pi}(m'(b))$ , and a ratio of gradients,  $dm/dm'$ , corresponding to a Jacobian matrix. In the case of the simulation, the two parts of the correction factor can be identified as mentioned before.

In order to calculate the correction a common variable to all particle and pion multiplicities is needed. The impact parameter,  $b$ , is the choice of such a variable, since all multiplicities depend on the impact parameter. In iQMD, the impact parameter is known for every single event. Therefore, all considered quantities can be identified with spectra of the variable as a function of  $b$ , the same  $b$  for  $m$ ,  $m'$ ,  $n_\pi$ , and  $n'_\pi$ . This leads to following equations for the pion multiplicity and the charged particle multiplicities:

$$f_{n_\pi}(m(b)) = \frac{dn_\pi}{dm(b)} = g_{n_\pi}(b), \quad f'_{n'_\pi}(m'(b)) = g'_{n'_\pi}(b) \quad (4.18)$$

and therefore:

$$\frac{f_{n_\pi}(m(b))}{f_{n'_\pi}(m'(b))} = \frac{g_{n_\pi}(b)}{g'_{n'_\pi}(b)}. \quad (4.19)$$

The ratio of derivatives is depending on  $b$  from the beginning.

Note that the correction has to be calculated for  $\pi^-$  and  $\pi^+$  separately. Figure 4.20 shows the different steps described above that lead to the derivation of the total correction. The different corrections described in equation 4.17 are shown explicitly. The left upper panel in figure 4.20 shows the two multiplicities as a function of  $b$ . The spectra are derived from iQMD events where the impact parameter  $b$  is a direct input parameter. The first spectrum (blue dots), identified as  $m(b)$ , corresponds to the multiplicity of particles within the geometrical acceptance of the detector when tracking is disregarded. The second spectrum in this panel figure depicts the particle multiplicity observable  $m_{cbp}$ , after a full GEANT simulation, to be identified with  $m'(b)$ . The ratio of derivatives,  $\frac{dm}{dm'}$ , is shown as black dots in this panel. The labels on the right side corresponds to the magnitude

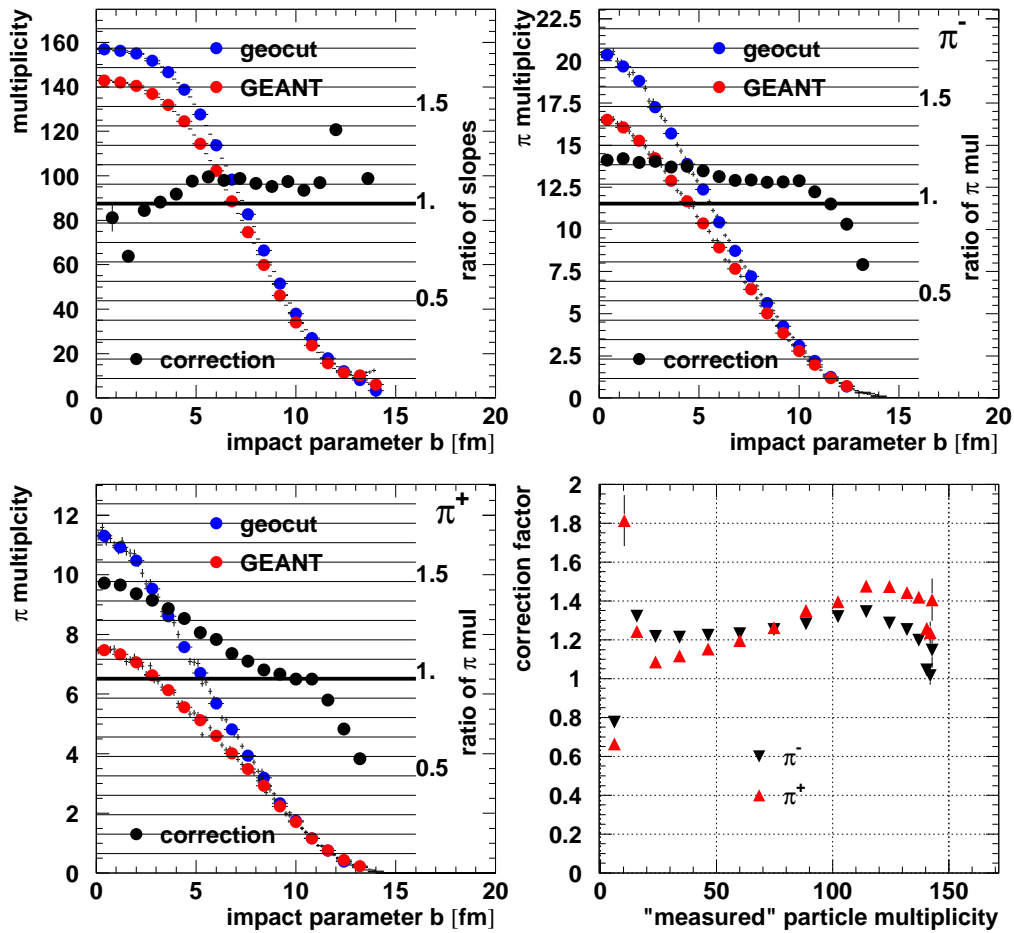


**Figure 4.20:** Determination of the correction according to multiplicity. Upper left panel: the correction due to the ratio of the derivatives of the particle multiplicities. Upper right panel: the ratio of  $\pi^-$  multiplicities. Lower left panel: the ratio of  $\pi^+$  multiplicities. Lower right panel: the final correction as a function of the multiplicity for the two pion species.

of this ratio<sup>9</sup>. The correction due to the matching of the two multiplicities namely the "true" spectrum,  $m(b)$ , and the "measured" spectrum,  $m'(b)$ , turns out to be in the order of 1.1, and to be flat over a large range of impact parameters.

The correction for the two pion species is the ratio of the individual pion multiplicities  $\frac{g_{n\pi}(b)}{g'_{n\pi}(b)}$ . This is depicted with the same colour code in the upper right panel for the  $\pi^-$  and the lower left panel for the  $\pi^+$ . Inefficiencies of the  $\pi^+$  identification are visible as a function of  $b$ . The correction factor drops from about 1.6 to approximately 1. with increasing impact parameter. In contrast, the  $\pi^-$  is not that much effected by losses and the correction factor stays roughly constant with a slight drop from 1.3 to 1.1. This qualitative difference is a result of different charges of the two pion species. Since the  $\pi^-$  are curved in the opposite direction to the  $\pi^+$  mesons the identification of  $\pi^-$  tracks is clearer then that of  $\pi^+$ .

The total correction is derived by combining the two corrections. Since  $b$  is not directly measured in the experiment, the correction is related to the "measured" multiplicity instead – compare lower left panel in figure 4.20. Here, the individual corrections for  $\pi^-$  and  $\pi^+$  are shown. The qualitative difference between the corrections obtained for  $\pi^-$  and  $\pi^+$  remain because the correction due to the multiplicity of particles is flat and the same for both pion species. The correction obtained shows the same trends as the correction from section 4.9.2.

However, it must be noted that the derived correction is not stable and depends on the input distribution. In figure 4.20, the charged particle multiplicities that were used as input distribution,  $m$ , are the multiplicities of particles within the geometrical acceptance of the detector. The multiplicity  $m'$  denotes, as described before, the "measured" multiplicity distribution from the MC simulation.

If, on the other hand,  $m$  from the complete phase space would be used instead, the presented method would give a correction of which the functional dependence would be reversed as shown in figure 4.21. The correction factors are now large for small number for participants (on the order of 1.8), and decrease to values below 1.0 for large  $A_{part}$ . The pion distributions are the same as in figure 4.20, and therefore, the functional dependence of the corrections on the impact parameter does not change as well.

Due to this peculiar behaviour, the correction discussed in this section is not used in the analysis of pion multiplicities presented in the following chapter of this work.

---

<sup>9</sup>Black lines are drawn in distances of 0.1.

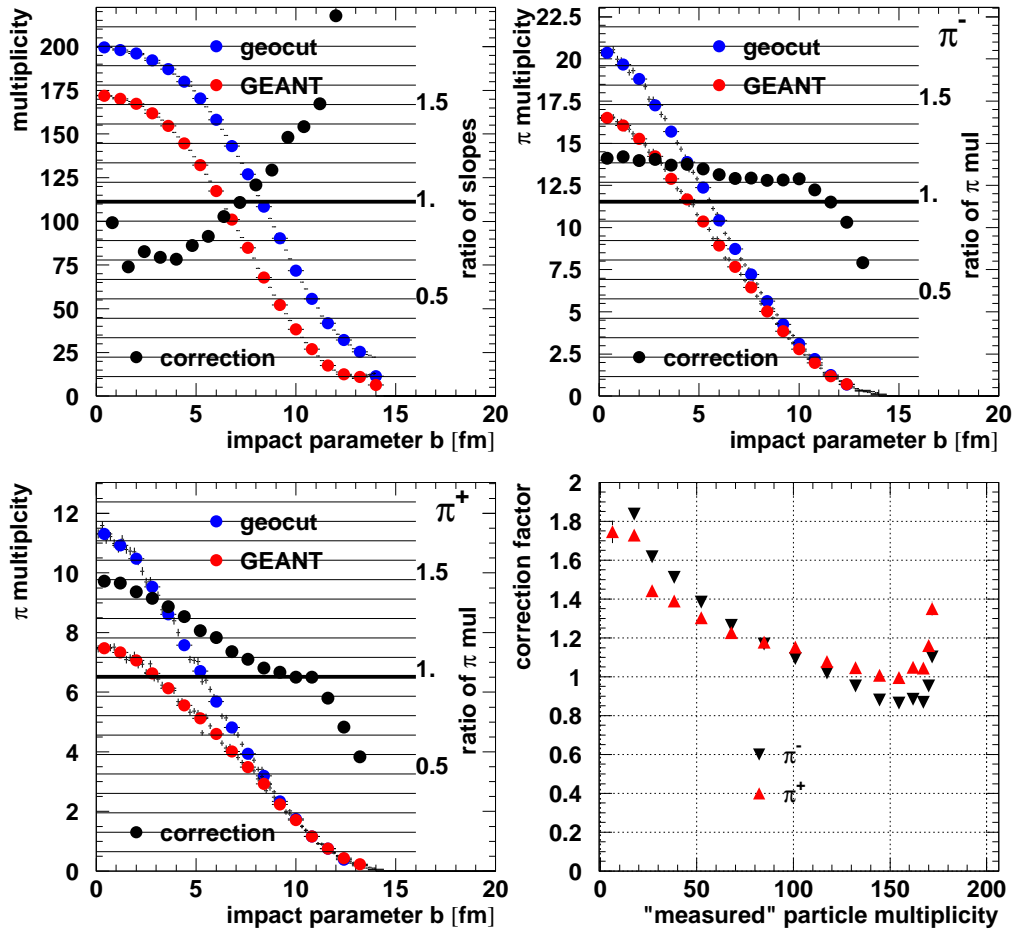


**Figure 4.21:** Determination of the correction according to multiplicity. However the complete charged particle multiplicity distribution is compared to the MC distribution.

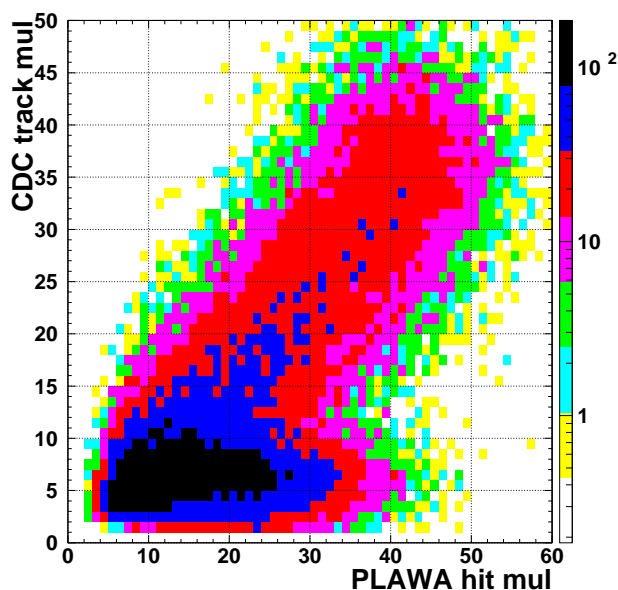


**Figure 4.22:** CDC track multiplicity,  $m_{ctrk}$ , versus PLAWA multiplicity,  $m_{ptrk}$ . The contribution from Oxygen events is visible as a band below 11 hits in the CDC.  $Zr + Zr$  @ 1.0 AGeV, no further selections

## 4.10 Different Treatment of Zr

The determination of the pion production for the  $Zr + Zr$  system is due to the target composition different to the other reactions. The Zirconium beam reacts with the Oxygen in the target foil and the Zirconium as well. Experimentally, the Oxygen events have to be considered as background and sorted out of the event sample which is used to determine the pion production. The inverse kinematics, a heavy beam (Zirconium) on a light target (Oxygen), provides a selection criterion on the Zirconium events. The Oxygen events are focused to the forward hemisphere. Figure 4.22 shows this behaviour. The Oxygen events can be removed with a cut on the CDC multiplicity,  $m_{ctrk}$ . The cut condition vary from 8, 11, and 12 tracks in the CDC for the different energies 400 AMeV, 1000 AMeV, and 1500 AMeV, respectively. In order to extract the pion data in the same manner as described above, the resulting  $m_{ptrk}$  distribution is integrated to determine the impact parameter, and therefore  $A_{part}$ . The correction factors are taken from the Ruthenium simulations because the of the same system size. The remaining analysis is the same as described above namely fitting the pion multiplicity versus the number of participants with a linear ansatz (see next section). The fit results are give in the appendix D.

## 4.11 Pion Yield Determination

From the corrected data the pion yield per participating nucleon can be derived. Since the dependence of the pion multiplicity on the number of participants is found to be linear in all measure colliding systems, the mean number of pions,  $\langle n_\pi \rangle$ , per mean number of participants,  $\langle A_{part} \rangle$ , can be determined directly as the slope of the pion multiplicity distribution with respect to  $A_{part}$ . Therefore, the corrected pion multiplicity spectra are fitted with the linear function

$$n_\pi(A_{part}) = a_0 + a_1 A_{part}. \quad (4.20)$$

The value of the fit parameter  $a_1$  gives the slope of the function  $n_\pi(A_{part})$

$$a_1 = \frac{\langle n_\pi \rangle}{\langle A_{part} \rangle}. \quad (4.21)$$

With decreasing number of participants the probability to produce a pion diminishes to zero. Hence, ideally the value of the parameter  $a_0$  should be small. The fit was restricted to a range  $0.15 < A_{part}/A_{sys} < 0.85$  in order to avoid distortions due to the impact parameter selectivity of the apparatus. In appendix D starting on page 105, all fit parameters are collected, together with the errors resulting from the fit. The uncorrected pion multiplicities are included there as well. The change in the slopes is already mentioned in section 4.9.2 to show the effect of the correction which is applied to the data.

For internal documentation the DST<sup>10</sup> generations of the finally analysed data are collected in the appendix B.1. Other DST generations than the listed ones give the same result concerning the pion multiplicities and the ratios. These two observables are not very dependent on the slight changes of the calibration going from one version of a DST generation to another. The run numbers are included in table B.1. The results for all systems and energies are given in the next chapter.

## 4.12 Error Estimations

The final observable, namely the slope of the pion versus  $A_{part}$  distribution, has different sources of uncertainties. Both results, the yield of pions and the pion ratio, are considered separately.

At first the deviation from the linear behaviour is treated. The error due to the fitting routine is negligible due to the fact that the functional dependence of the pion numbers vs.  $A_{part}$  is in the fit-range perfectly linear. The fit results are listed in the appendix D on page 105. Both, the free fit, equation 4.20, and the

---

<sup>10</sup>DST: Data Summary Tape.

reaction and energy [AMeV]	$\pi^-$ [%]	$\pi^+$ [%]	$\pi^- + \pi^+$ [%]
<i>Ca + Ca</i> 1000	8.24	3.9	6.4
<i>Ca + Ca</i> 1500	12.5	16.4	14.1
<i>Ru + Ru</i> 400	12.1	11.9	11.4
<i>Ru + Ru</i> 1000	6.65	6.08	6.43
<i>Ru + Ru</i> 1500	3.95	3.16	3.72
<i>Au + Au</i> 400	1.52	4.84	1.83
<i>Au + Au</i> 1000	2.35	1.28	1.91
<i>Au + Au</i> 1500	4.93	3.84	4.43

**Table 4.3:** Variation of the slopes of the different determinations of the pion versus  $A_{part}$ -axis. The third column denotes the variation of the fit of the sum of the charged pions.

constraint fit are listed including the fit errors. This error is not taken into account into the following discussion.

The yield determination has two error contributions. First the different charged particle multiplicities, which can be used to determine the  $A_{part}$ -axis, can give an estimation of the error on the slope introduced by these different methods to derive the impact parameter. The variance of the slope due to the different possibilities to determine the  $A_{part}$ -axis gives a handle on this error. Calculating the standard deviation leads to the errors listed in table 4.3. Since the yield is determined with the fit of the sum of negatively and positively charged pions the error of this quantity is used. In this context one has to note that for the 400 AMeV *Ca + Ca*-reactions only the multiplicity,  $m_{cbp}$  is available, because of the small number of charged particles in the other variables it is not possible to apply the same procedure to all multiplicity variables.

Second the contribution of the efficiency correction has to be considered. The standard deviation from the input slope is calculated to estimate this efficiency. Table 4.4 summerises the results of these estimations. The contribution to the error on the yield determination,  $\Delta n_{\pi}^{MC}$  is calculated as:

$$\Delta n_{\pi}^{MC} = 1.5 * \sqrt{(n_{\pi^-}^{MC})^2 + (n_{\pi^+}^{MC})^2}. \quad (4.22)$$

Both error contributions are considered to be independent of each other. Therefore the total error is calculated as the square root of the quadratic sum of both errors.

Tables 4.3 and 4.4 show agreement of the data and the MC simulation. Both error contributions are in the same range of 4 to 10%. The GEANT simulation of the detector works very well.

reaction and energy [AMeV]	$\pi^-$ [%]	$\pi^+$ [%]	$\pi^-/\pi^+$ [%]
<i>Ca + Ca</i> 400	13.1	7.09	10.8
<i>Ca + Ca</i> 1000	10.4	9.14	7.53
<i>Ca + Ca</i> 1500	7.55	7.37	2.15
<i>Ru + Ru</i> 400	8.68	12.3	5.41
<i>Ru + Ru</i> 1000	6.27	9.4	2.98
<i>Ru + Ru</i> 1500	5.92	10.2	4.04
<i>Au + Au</i> 400	7.12	10.2	5.1
<i>Au + Au</i> 1000	5.01	4.15	2.32
<i>Au + Au</i> 1500	5.1	8.07	2.91

**Table 4.4:** Reconstruction errors within the GEANT analysis. The standard deviation of the reconstruction efficiencies for the charged pions and the ratio of charged pions is shown.

The error of the charged pion ratio is expected to be smaller than the error of the yield. Cancellation effects of the determination of the  $A_{part}$ -axes, since this is the same for both charged pion species, are expected. The error on this observable is deduced from the standard deviation of the determined ratios to the input iQMD ratio. The last column of table 4.4 shows the error of the reconstruction of the pion ratio. It turns out that the ratio is determined in a much better accuracy than the individual pion slopes. This shows the systematic error introduced by the  $A_{part}$  determination. The uncertainty of the Monte Carlo simulation as introduced in section 4.9.1 is added quadratically to the deviation of the ratio reconstruction efficiency. This is the largest contribution to the error of the charged pion ratio.

Uncertainties in the absolute cross section determination, especially for the Calcium system leads to a systematic error. The measured cross section for the incident energies of 400 AMeV and 1000 AMeV has to be scaled with a factor of 1.5 and for the highest energy a scale of 1.8 is introduced. For example the change for the Calcium at 1000 AMeV from 1.5 to 1.8 reduces the slope of 4.0%. Gold reactions at 400 AMeV are scaled by 1.2, here the change from no scaling to the scaled cross section is on the same order of 4%. These changes have no effect at all on the ratios determined by the slopes of the charged pion multiplicities in the representation as pion numbers versus number of participants.



## Chapter 5

# Experimental Results

This chapter summarises the pion production data obtained for the  $Ca + Ca$ ,  $Ru + Ru$ ,  $Zr + Zr$ , and  $Au + Au$  reactions at energies of 400 AMeV, 1000 AMeV, and 1500 AMeV. The corrections described in the previous chapter are applied to all the four systems at all energies individually. After the experimental data are corrected, the mean number of pions per mean number of participant is derived. The results are listed in the different tables collected in the appendices D on page 105. It is possible to extract the system-size dependence and the evolution of pion abundances as a function of energy from the available results. Since both pion species are measured, the charged pion ratios  $R_\pi = \frac{n_{\pi^-}}{n_{\pi^+}}$  are extracted as well for the different colliding systems and energies. The following sections report on the measured pion yield and charged pion ratios for the examined reactions.

### 5.1 The Total Pion Yield

The charged pions are measured as described in the previous chapter. In order to extract the total pion yield, the contribution from neutral pions has to be estimated as well. Effectively the sum of the to charged pion species is multiplied by 1.5 to calculate the total number of pions.

Figure 5.1 shows a summary of the pion production per  $A_{part}$  for all systems and energies. The production probability per participating nucleon is given as the mean number of pions,  $\langle n_\pi \rangle$ , per mean number of participating nucleons,  $\langle A_{part} \rangle$ , and plotted versus the system size. For all energies a suppression of the number of pions per  $A_{part}$  is observed compared to the lightest system considered. The smallest system produces the largest number of pions, relative to the number of participants. The change in pion production, comparing Ruthenium and Gold, is on the order of 8% for the highest energy and almost not visible at 1000 AMeV. At an energy of 400 AMeV, the reduced pion number of the intermediate system

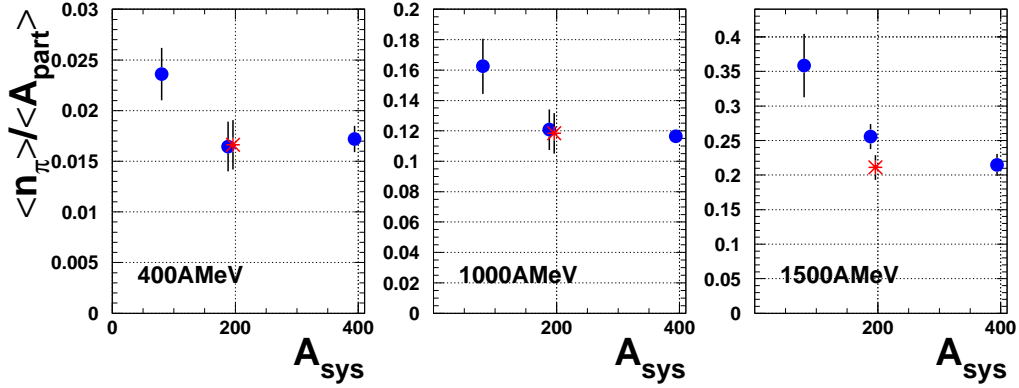


**Figure 5.1:** Pion production dependence on the colliding system and energy. The Zirconium data points are shown as the red crosses for a better distinction from the Ruthenium points in addition the equal mass number of Ruthenium and Zirconium of  $A = 96$  is shifted. (note: different scales!)

and the heaviest system are the same within errors. The change from Calcium to Ruthenium is larger than from Ruthenium to Gold, which is almost constant within errors. This can be interpreted as a saturation of the pion production and suggests that the system approaches some state which is close to an equilibrium value. This is required for a thermodynamic interpretation, e.g. an exact thermodynamic limit implies a constant number of pions per  $A_{part}$ , independent of the system size. The difference in the production probability from Calcium to Gold gets larger for higher energies (note the scales in figure 5.1).

The Zirconium pion multiplicities, represented in figure 5.1 with red crosses are indistinguishable from the Ruthenium data points at energies of 400 AMeV and 1000 AMeV. At 1500 AMeV bombarding energy the pion yield of the Zirconium system and the Ruthenium agrees within the errors.

The observed size dependence is by far not trivial to understand. On the one hand, the functional dependence of the number of pions on the number of participants is still linear for all examined systems. This behaviour implies that central  $Ru + Ru$  collisions are not the same as semi central  $Au + Au$  collisions. And especially the  $Ca + Ca$  collisions are not similar to peripheral collisions of heavy colliding systems. Since a size dependence on the fireball is not visible within a collision system alone, shadowing effects of spectator matter have to be taken into account. On the other hand, investigations on highly central reactions, where the shadowing due to spectator matter is negligible, have shown the same system size dependence (see section 5.3).

The excitation function is given in figure 5.2. The production probabilities

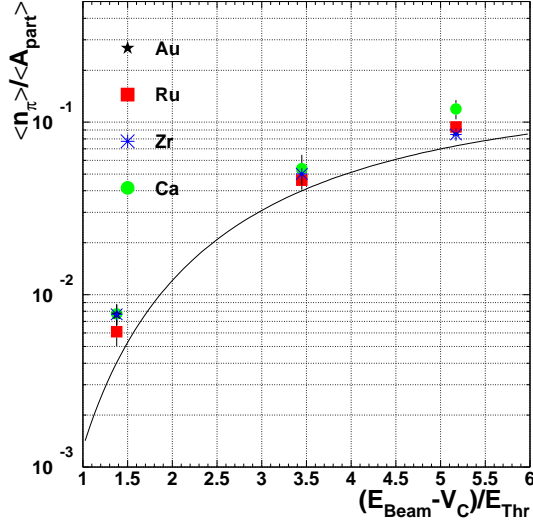


**Figure 5.2:** Pion Production excitation function for all systems. Only the negatively charged pions are shown. The solid line represents the Metag systematics.

are plotted as a function of incident beam energy normalised to the production threshold of pions. An empirical scaling, introduced by Metag [Metag, 1997], is depicted by the solid line. The Metag systematic is an empirical fit to the data of negatively charged pions available at that time, from subthreshold pion production up to SPS energies. The x-axis in this representation gives the bombarding energy in scales of the pion production threshold. The coulomb energy,  $V_C$ , is negligible in our energy range. The data points lie systematically above the Metag systematic but show the same trend. This difference should not be taken seriously since the original fit of Metag spans over 7 orders of magnitude in pion production probabilities.

## 5.2 Pion Ratios

Individual fits for the two charged pion species allow to extract the  $\pi^-$  to  $\pi^+$  ratio. The ratio,  $R_\pi$ , can be deduced from the slope parameter,  $a_1$ , of the fits of the charged pions.

$$R_\pi = \frac{n_{\pi^-}}{n_{\pi^+}} = \frac{\langle n_{\pi^-} \rangle}{\langle A_{part} \rangle} / \frac{\langle n_{\pi^+} \rangle}{\langle A_{part} \rangle} = \frac{a_1^{\pi^-}}{a_1^{\pi^+}}. \quad (5.1)$$

This method of deriving the ratios of charged pions neglects a possible  $A_{part}$  dependence of the primary quantities, the pion yields versus  $A_{part}$  but is a good measure as long as the pion multiplicities depend linearly on  $A_{part}$ . That this is the case is already shown with the smallness of the fit error as listed in appendix D. The extracted pion ratios are shown in figure 5.3. The extracted pion ratios of the

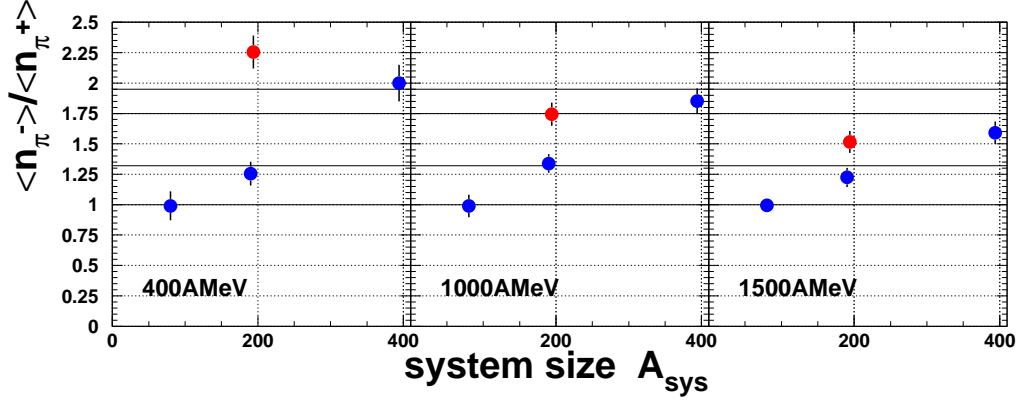


**Figure 5.3:** Pion ratios for different isospin conditions. Red dots correspond to the Zirconium system. The solid lines indicate the isobar model predictions.

colliding systems  $Ca + Ca$ ,  $Ru + Ru$ , and  $Au + Au$  agree with the isobar model predictions introduced with equation 5.2 (solid lines in figure 5.3) for the low energy data. This changes if the energy increases especially for the heaviest colliding system. The ratios are decreasing with increasing energy for the  $Au + Au$  system. This leads possibly to the conclusion that higher resonances are involved in the pion production. In particular for the system with the most nucleons.

The situation changes for the Zirconium system. A decrease of the pion ratio,  $R_{\pi}$ , with increasing energy is observed, too. The agreement to the isobar model is not given at the low energy and the high energy.

The isobar model [Stock, 1986] connects the third component of the isospin,  $I_3$ , of the reaction partners with the expected pion ratios<sup>1</sup>. Only the  $\Delta$ -resonance with  $I = \frac{3}{2}$  is considered in this model. The pion ratios  $n_{\pi^-} : n_{\pi^0} : n_{\pi^+}$  are calculated with the initial isospin conditions using the following formula:

$$n_{\pi^-} : n_{\pi^0} : n_{\pi^+} = (5N^2 + NZ) : (N^2 + 4NZ + Z^2) : (5Z^2 + NZ). \quad (5.2)$$

with  $N$ ,  $Z$  the number of neutrons, respectively protons in the target or projectile. Table 5.1 summarises the expected ratios for the reactions under consideration. The  $n_{\pi^-}$  to  $n_{\pi^+}$  ratio,  $R_{\pi}$ , is found in table 5.1 in the column  $n_{\pi^-}$  due to the normalisation that is used there.

The isospin predictions from equation 5.2 are based on a isospin  $I = 3/2$  resonance. The same calculations for a isospin  $I = 1/2$  resonances, the  $n'_{\pi^-} : n'_{\pi^0} : n'_{\pi^+}$  ratio would change to [Pelte et al., 1997a]:

$$n'_{\pi^-} : n'_{\pi^0} : n'_{\pi^+} = 2Z : (N + Z) : 2N. \quad (5.3)$$

<sup>1</sup> $I_3 = +\frac{1}{2}$  proton,  $I_3 = -\frac{1}{2}$  neutron.

System	A	Z	N	$\frac{N}{Z}$	$n_{\pi^-}$	$n_{\pi^0}$	$n_{\pi^+}$
Ca	40	20	20	1.0	1.0	1.0	1.0
Ru	96	44	52	1.18	1.32	1.15	1.0
Zr	96	40	56	1.4	1.75	1.34	1.0
Au	197	79	118	1.49	1.95	1.42	1.0

**Table 5.1:** Pion ratio predictions from the isobar model for the three different colliding systems. Only isospin symmetric systems are used. The numbers are normalised to the  $\pi^+$  meson, therefore  $R_\pi = n_{\pi^-}$

System	A	Z	N	$\frac{N}{Z}$	$n'_{\pi^-}$	$n'_{\pi^0}$	$n'_{\pi^+}$
Ca	40	20	20	1.0	1.0	1.0	1.0
Ru	96	44	52	1.18	0.85	0.92	1.0
Zr	96	40	56	1.4	0.71	0.86	1.0
Au	197	79	118	1.49	0.67	0.83	1.0

**Table 5.2:** Pion ratios from the isobar model ( $I_3 = \frac{1}{2}$ ) for the four different colliding systems. The numbers are normalised to the the  $\pi^+$  meson.

These ratios are even lower than the measured ones. The equations (5.2 and 5.3) are valid only for first generation resonance decays and comprise only pure  $I = \frac{3}{2}$  and  $I = \frac{1}{2}$  resonances, respectively. The degree of admixture of higher resonances represents an access to the temperature of the system. A comparison to a thermal model is given in the next chapter section 6.1 on page 81.

Formula 5.2 shows that the charged pion ratio depends on the initial isospin ratio. Therefore, the natural observable to plot the measured pion ratios is the neutron to proton ratio  $N/Z$  of the two colliding nuclei. As there are considered only isospin symmetric reactions the initial isospin ratio corresponds to the neutron to proton ratio of one nucleus. Equation 5.2 can be written as:

$$\frac{\pi^-}{\pi^+} = \frac{5N^2 + NZ}{5Z^2 + NZ} \approx \left(\frac{N}{Z}\right)^2 \quad (5.4)$$

Figure 5.4 shows the pion ratios versus the  $N/Z$  of the colliding nuclei. The quadratic behaviour is fulfilled for the lower two energies, while for the high energy data the linear dependence is favoured. In [Nagamiya et al., 1981] the  $\pi^-$  to  $\pi^+$  ratio is measured at 800 A MeV for seven different projectile/target combinations from Carbon to Lead. At this energy the simple  $(N/Z)^2$  scaling is fulfilled too<sup>2</sup>.

<sup>2</sup>In [Li et al., 1998] this is wrongly cited as the reaction  $Ar + KCl$  at an energy of 2.1 A GeV.

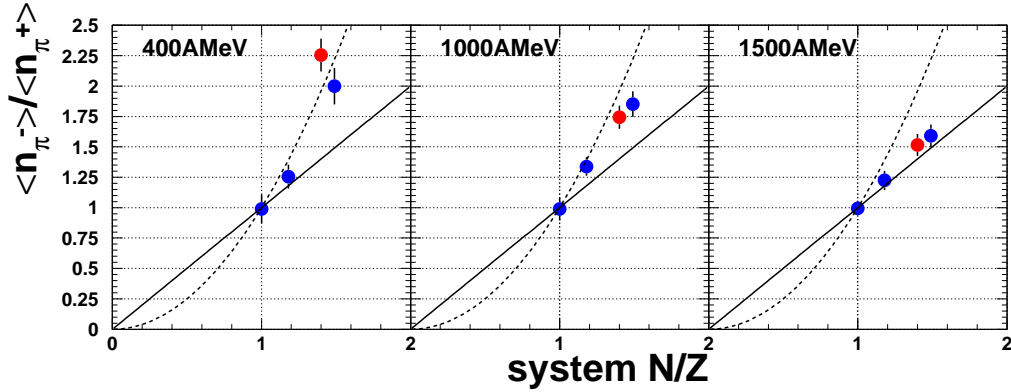


**Figure 5.4:** Charged pion ratios versus the initial isospin ratios. Solid line:  $\frac{N}{Z}$ , dashed line  $(\frac{N}{Z})^2$ .

### 5.3 Comparison with Experiments

Most experimental data on pion production are available for an incident energy of 1.0 A GeV. Figure 5.5 summarises the available data. The number of pion per participating nucleons versus the mean number of pions are plotted from the various experiments. The Ruthenium and Gold data presented here, seem to follow the Harris systematic, whereas the Calcium point exceeds the Harris systematic. The system size dependence of the pion yields found in this work contradicts the result of [Harris et al., 1985], since the reaction  $Ar + KCl$  investigated by the Streamer Chamber group has the same mass as the  $Ca + Ca$  system.

The presented pion production probabilities are in rather good agreement with the experimental findings of KaoS. The Calcium measurement fits to the trend given with the Carbon and the Nickel pion production probabilities stated by the KaoS collaboration. The flattening observed in this work seems to be more pronounced than in the KaoS measurements, but the gap in mass of the measured systems using the KaoS spectrometer is large and spans from Nickel to Gold. The Gold point of KaoS agrees within 19% with the Gold point presented here.

As far as former **FOPI** measurements are concerned, the data of this work exceed the values stated in [Pelte et al., 1997b], and [Pelte, 1998]. The Nickel measurement from [Pelte et al., 1997a] fits to the trend from the Calcium and the Ruthenium points. The deduced former Ruthenium measurement is exceeded by about 25%. The difference gets larger for the Gold point where the presented data are above the previously measured point by about 50%. The almost linear decrease of the number of produced pions per  $A_{part}$  versus  $A_{part}$  cannot be confirmed in this analysis. The former analysis used another method to determine

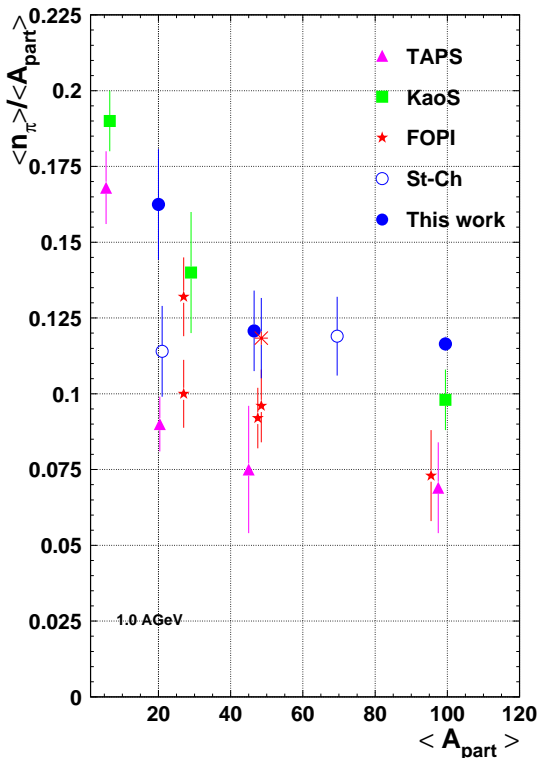


**Figure 5.5:** Pion production at 1 AGeV, same figure as 1.3, including the data of this work and [Hong et al., 1997].

$A_{part}$  and a different, not multiplicity dependent, efficiency correction. The differences are investigated in the following section.

In comparison to the TAPS data, all measurements using charged pions are always above the extrapolations from the measurements of the neutral pions,  $\pi^0$ . The system size dependence observed there is the same as observed in this work.

A comparison to other energies is done in the following section.

## 5.4 Comparison to FOPI Data

This section gives an internal comparison to existing published and unpublished pion data of the FOPI collaboration.

At 400 A MeV, left panel in figure 5.6, the results are taken from [Reisdorf, 2001]. These results are from a fully independent analysis, in which the two dimensional phase-space distributions were used to reconstruct the full phase space. The charged pions distributions were fitted with a biquadratic fit in order to extrapolate the unmeasured parts of the phase-space. In this analysis the most central reactions, 15% of the reduced impact parameter,  $b^{(0)} = b/b_{max}$ , of each event sample, are selected. This leads to a mean number of participants  $\langle A_{part} \rangle$  of 73, 180, 355 for the systems  $Ca + Ca$ ,  $Ru + Ru$ ,  $Au + Au$ , respec-

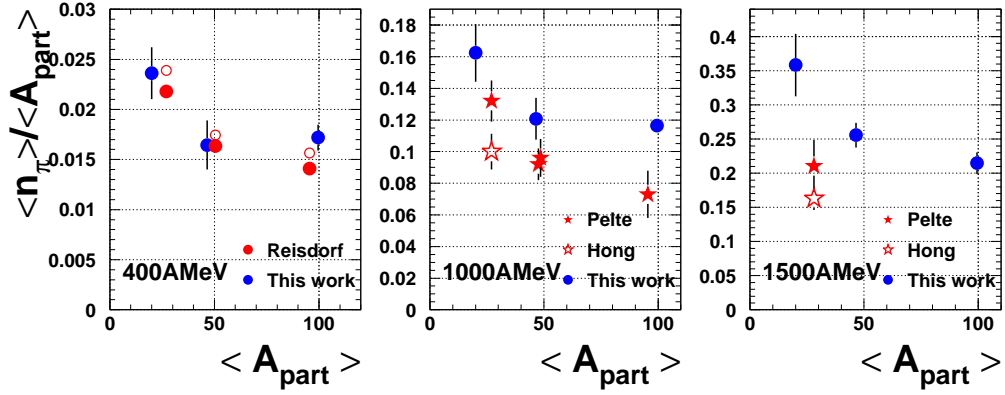


**Figure 5.6:** Comparison to FOPI-data at all measured energies. For a better visibility the points in the left panel are displaced. Additional reference [Hong et al., 1997].

tively [Gosset et al., 1977]. The resulting total number of pions normalised to the system size (depicted as red circles) is multiplied by  $A_{sys} / \langle A_{part} \rangle$  to give the mean number of pions per mean number of participants (depicted as red dots in figure 5.6). The results of the two analysis agree within errors perfectly.

For the comparison of the higher energies, published data are available from [Pelte et al., 1997a], [Pelte et al., 1997b], [Hong et al., 1997], and [Pelte, 1998].

In figure 5.6, middle and right panel, the data for 1.0 and 1.5 AGeV are compared with this former published data.

The corrections of the data introduced in [Pelte et al., 1997b] and [Pelte et al., 1997a] were different from those described in this work. Assuming that the efficiency of detecting a pion,  $\epsilon$ , does not depend on the multiplicity, only global corrections were applied. The following steps were done to find out the correction factors [Pelte, 2001].

The pions resulting of an iQMD calculation were counted using the whole phase space. The yields were normalised to the number of events and divided by the mean number of participants, by dividing the total system size by 4 ( $\langle A_{part} \rangle = A_{sys}/4$ ) The mean number of pions per participating nucleon  $\frac{\langle n_{\pi}^{4\pi} \rangle}{\langle A_{part} \rangle}$  was calculated. However, this approach implies the assumption that the linear dependence of the number of pions is fulfilled in the framework of iQMD, which is, as shown in the figure 4.17 on page 58, a correct assumption.

The GEANT data were treated in a different way. The multiplicity information was used to determine the cross section. The number of participants,  $A_{part}$ , was derived using a sharp cutoff model. The resulting pion per  $A_{part}$  spectra were

fitted using a third order polynomial:

$$n_{\pi}^{MC}(A_{part}) = \sum_{i=1}^3 a_i A_{part}^i. \quad (5.5)$$

In sequence the average number of pions,  $\langle n_{\pi}^{MC} \rangle$ , per average number of participants,  $\langle A_{part} \rangle$ , were deduced from the coefficients  $a_i$  via:

$$\frac{\langle n_{\pi}^{MC} \rangle}{\langle A_{part} \rangle} = \sum_{i=1}^3 \frac{a_i}{i} A^{i-1} \quad (5.6)$$

where  $A$  is the total number of nucleons. The correction factor,  $c = \frac{1}{\varepsilon}$ , is the ratio of the  $4\pi$  yield and the yield resulting of the GEANT simulation,  $MC$ :

$$c = \frac{1}{\varepsilon} = \frac{\langle n_{\pi}^{4\pi} \rangle}{\langle A_{part} \rangle} / \frac{\langle n_{\pi}^{MC} \rangle}{\langle A_{part} \rangle}. \quad (5.7)$$

The resulting correction was applied to the data. The  $A_{part}$  axis for the experimental data was determined differently. With the assumption that  $A_{part}$  has to follow the charged particle multiplicity in a one to one fashion [Pelte et al., 1997b] the parameters of a smeared nuclear density profile were chosen to fit this requirement. Another tracking algorithm was used in addition and the tracking efficiency was found to be one over all multiplicity bins. Effectively, only a 10% correction was applied to take into account the geometrical acceptance of the **FOPI**-detector as shown in figure 4.12 on page 50. The real counting of the charged pions was done in the same way as in this work, namely a double counting of identified pions in the region of  $y^{(0)} < 0$ .

Another way of counting is to determine the pion yield by integrating a  $\frac{dN}{dy}$  spectrum. This method is described in the next section.

### 5.4.1 Interpretation of $m_{\perp}$ -Spectra

In the analysis presented in [Hong et al., 1997] another strategy was embarked.  $m_{\perp}$ -spectra in different rapidity bins were fitted with two exponentials. This takes into account that the pion  $m_{\perp}$ -spectrum is not very well reproduced only with one exponential<sup>3</sup>. The low  $p_{\perp}$  region and, therefore, low transverse masses  $m_{\perp}$ , which is not covered by the acceptance of the **FOPI**-detector can be reconstructed using extrapolations of the fit to the unmeasured  $p_{\perp}$  region. In the work of [Hong et al., 1997] this was the only correction which was applied to the data.

---

<sup>3</sup>Note:  $m_{\perp} = \sqrt{m^2 + p_{\perp}^2}$ .

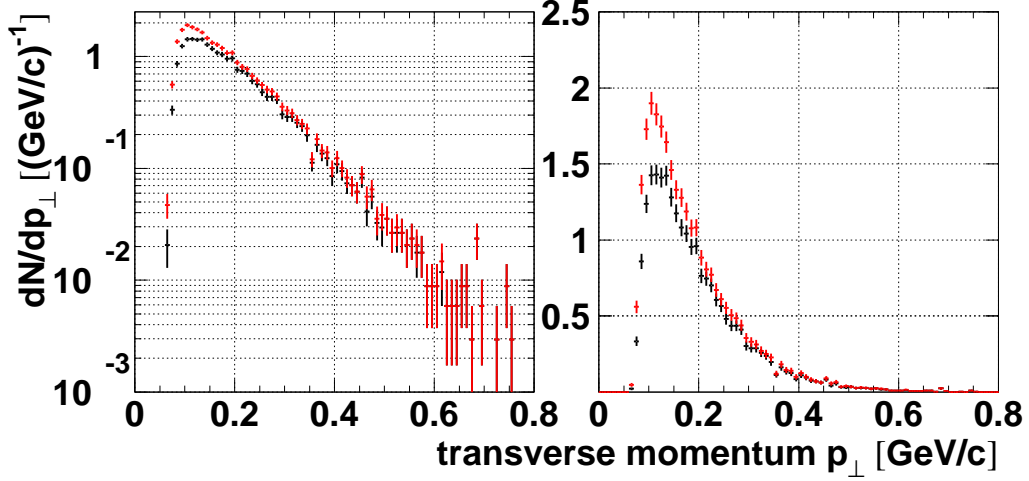


**Figure 5.7:**  $p_{\perp}$  distribution of the  $\pi^{-}$  meson in a rapidity window of  $-0.2 < y^{(0)} < 0.$ . black: under consideration of a  $d0$  cut of 0.5 cm. red: with a  $d0$  cut of  $3\sigma$ . left panel logarithmic scale, right panel the same with linear scale. [Au + Au @ 1.0 AGeV]

A lower transverse momentum cut was introduced in addition to exclude not reliable data ([Hong, 2001]). This can be seen in connection with the stringent  $d0$  cut of  $d0 = 0.5$  cm, which cuts arbitrarily the low momentum pions as shown in figure 4.11 on page 47. The low  $p_{\perp}$  cut varies from around 100 MeV/c for target rapidity to 250 MeV/c for mid-rapidity. The integration of the  $m_{\perp}$  spectrum from  $0 \rightarrow \infty$  including the unmeasured low  $p_{\perp}$  part gives the pion yield in the specific rapidity bin  $\frac{dn_{\pi}}{dy^{(0)}}$ . The  $\frac{dn_{\pi}}{dy^{(0)}}$  distribution can be reflected around mid-rapidity using the mass symmetry of the reaction partners. The integration of the  $\frac{dn_{\pi}}{dy^{(0)}}$  distribution gives the pion yield. Figure 5.7 shows the difference in the  $p_{\perp}$  spectrum using the proposed  $3\sigma$  cut in  $d0$  and the former 0.5 cm cut. The shape of the spectrum (left in figure 5.7) does not change that much. In the low  $p_{\perp}$  region a clear loss with the 0.5 cm cut is visible. The right panel of figure 5.7 shows this in a linear scale for a better visibility. For the determined pion yield this lead to a change in the number of pions of about 15%. Including a tracking efficiency of about 20%, which was not considered in [Hong et al., 1997], the extracted pion yield in terms of  $\langle n_{\pi} \rangle / \langle A_{part} \rangle$  shown in figure 5.6 rises to values slightly above the data of [Pelte et al., 1997a]. This fits the trend suggested by the data of this work at 1.0 AGeV but not at 1.5 AGeV.

The experimental results are compared to different model predictions in the following chapter.

## Chapter 6

# Comparison to Theory

For the interpretation of particle numbers, collective phenomena, and particle spectra observed in Heavy Ion reactions the need for comparisons to theoretical models is obvious.

Different approaches with different assumptions are developed. One can separate the theoretical models into two classes; the first one the thermal models consider the final state of the reaction only. A thermal equilibrium is assumed, therefore the history of the particles is not accessible due to the thermalization. With this assumption measured particle ratios are used to calculate a temperature and a chemical potential which lead to these ratios.

The second class of models include the dynamic evolution of the system. The so called transport models describe a HI reaction on the level of nucleons. The propagation of every single nucleon is calculated including individual  $NN$ -collisions in the presence of a common mean field which is connected to the equation of state (EOS).

Within a theoretical framework one can change some conditions in order to check for the changes in a chosen observable. For example the EOS can be chosen in iQMD and BUU. The effect on different parameterisation of the EOS on particle multiplicities and ratios can be calculated from such transport models. While a thermal model give access to temperature and the chemical potential for given particle ratios. A short introduction of different models is given in the following sections.

### 6.1 The Thermal Model

Within the thermal model the abundances of all particles can be described with two parameters: the temperature,  $T$ , and the baryo-chemical potential,  $\mu_B$ . Assuming a grand canonical ensemble, the freeze out configura-

tion, namely the particle ratios, can be used to determine these two parameters using equation 6.1. This is achieved by fitting simultaneously the measured particle ratios of different particle species  $i, j$ ,  $R = \frac{n_i}{n_j}$ . For the high energies at AGS<sup>1</sup> ( $p \sim 14.5 \frac{\text{AGeV}}{c}$ ) [Braun-Munzinger et al., 1995], at SPS<sup>2</sup> ( $p \sim 200 \frac{\text{AGeV}}{c}$ ) [Braun-Munzinger et al., 1996],[Braun-Munzinger et al., 1999], and at RHIC<sup>3</sup> with  $\sqrt{s} = 130 \text{ GeV}$  [Braun-Munzinger et al., 2001] the grand-canonical ensemble is successfully used to describe the data. The same model as in the above mentioned references is used here to illustrate the behaviour of charged pion ratios as a function of temperature for given chemical potentials.

In this ansatz thermal and chemical equilibrated hadronic matter is assumed. The density  $n$  of a particle species  $n_i$  is given as:

$$n_i = \frac{g_i}{2\pi^2} \int_0^\infty \frac{p^2 dp}{\exp\{[E_i(p) - \mu_i]/T \pm 1\}}, \quad (6.1)$$

with particle density  $n_i$ , spin/isospin degeneracy  $g_i$ ,  $\hbar = c = 1$ , momentum  $p$ , total energy  $E$  and chemical potential  $\mu_i$ . The chemical potential,  $\mu_i$ , is composed of:

$$\mu_i = \mu_B B_i - \mu_S S_i - \mu_{I_3} I_{3i}. \quad (6.2)$$

The quantities  $B_i$ ,  $S_i$ , and  $I_{3i}$  are the baryon, strangeness and the third component of the isospin quantum numbers of the particle of species  $i$ . The independent free parameters of the model are the temperature,  $T$ , and the baryo-chemical potential,  $\mu_B$ .  $S_i$  and  $I_{3i}$  and the Volume  $V$  are fixed by conservation laws:

$$V \sum_i n_i B_i = Z + N \quad V \sum_i n_i S_i = 0 \quad V \sum_i n_i I_{3i} = \frac{Z - N}{2}. \quad (6.3)$$

$Z$  and  $N$  are the proton and neutron number of the combined colliding nuclei, respectively ( $N = N_{projectile} + N_{target}$ ; same for the neutrons). The partition function contains the contributions from all mesons and baryons with masses up to 1.5 and 2.0 GeV, respectively. To account for repulsive interactions between hadrons at small distances, an eigen volume is assigned to all particles.

The other way around, for a given combination of  $T$  and  $\mu_B$ , particle ratios, like  $R_\pi = \frac{n_{\pi^-}}{n_{\pi^+}}$ , can be calculated. Figure 6.1 shows the evolution of charged pion ratios,  $R_\pi$ , as a function of temperature for baryo-chemical potentials between 700 MeV and 850 MeV. The model suggest that the data, represented as the pion ratios,  $R_\pi$ , are mostly sensitive to  $\mu_B$ , since at constant  $\mu_B$ , the calculated  $R_\pi$  does not change as a function of  $T$ . Comparing the measured pion ratios to the calculated ratios, the chemical potentials,  $\mu_B$ , are listed in table 6.1. The errors stated in this

<sup>1</sup>AGS: Alternating Gradient Synchrotron, BNL Brookhaven National Laboratory.

<sup>2</sup>SPS: Super Proton Synchrotron, CERN

<sup>3</sup>RHIC: Relativistic Heavy Ion Collider, BNL.

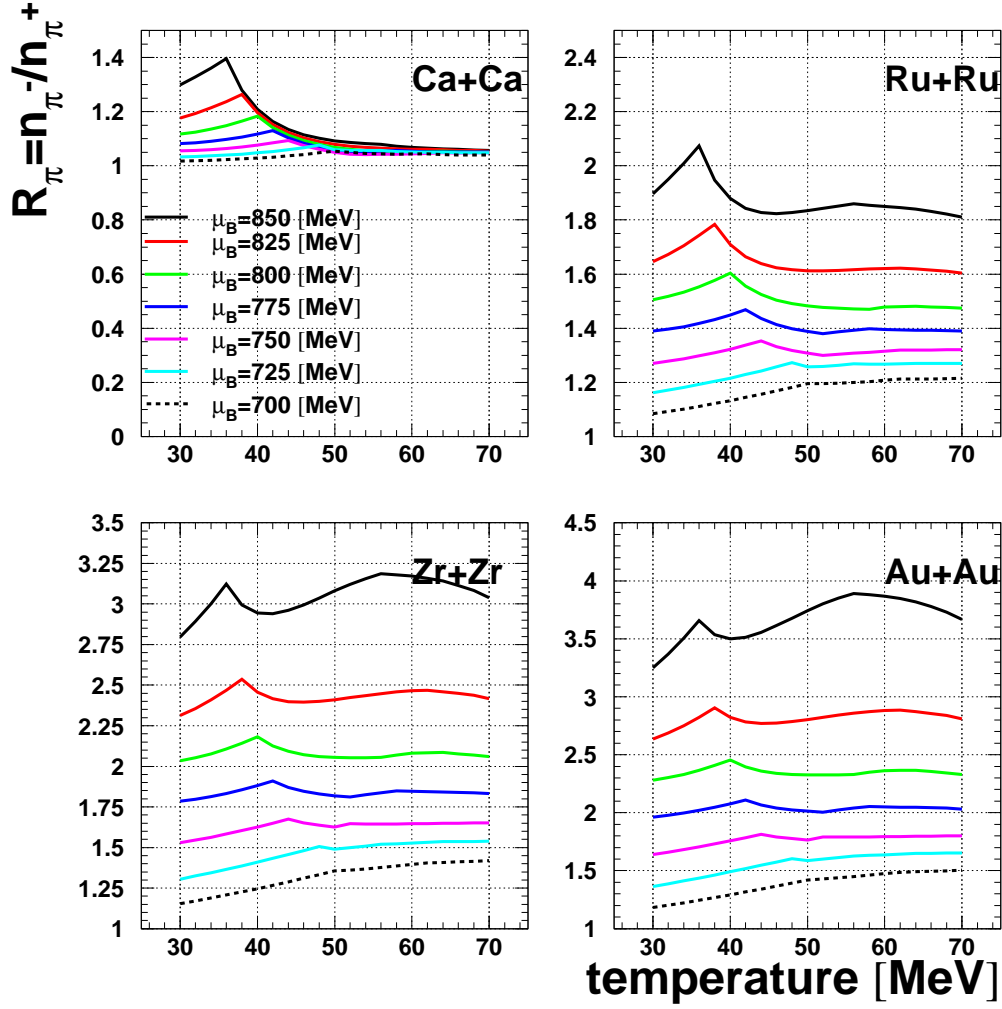


**Figure 6.1:** Pion ratios as a function of temperature calculated for different baryo-chemical potentials from  $\mu_B = 700$  MeV to  $\mu_B = 850$  MeV in steps of 25 MeV. All four systems are presented.

reaction	400 MeV	1000 MeV	1500 MeV
$^{197}\text{Au} + ^{197}\text{Au}$	$770 \pm 13$	$750 \pm 13$	$712 \pm 13$
$^{96}\text{Zr} + ^{96}\text{Zr}$	$812 \pm 13$	$762 \pm 13$	$725 \pm 13$
$^{96}\text{Ru} + ^{96}\text{Ru}$	$725 \pm 13$	$725 \pm 13$	$725 \pm 13$

**Table 6.1:** Extracted baryo-chemical potentials for three energies and reactions

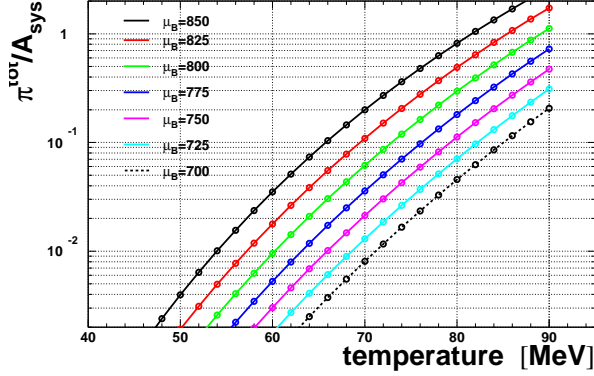


**Figure 6.2:** Pion yields determined from the thermal model. The baryo-chemical potentials are given in MeV

table are the maximal error of the measured charged pion ratio converted into the the baryo-chemical potential. Therefore the errors of the chemical potential are identical for all colliding systems.

The comparison for the Calcium system gives no access to  $\mu_B$ . At a temperature of 70 MeV the pion ratios merges 1.05 for all chemical potentials. At low temperatures the deviation to the measured ratio of  $R_\pi = 1.0$  is unexpectedly high (compare figure 6.1). Despite the isospin symmetry, the expected ratio of one is never reached in this framework. The Ruthenium system with a measured constant ratio of  $R_\pi = 1.3$  gives a constant baryo-chemical potential of  $\mu_B = 725$  MeV. The Gold and the Zirconium system show a dropping charged pion ratio  $R_\pi$  with rising incident energy. This leads to a dropping chemical potential within the framework of this thermal model as shown in table 6.1. The trend of a dropping baryo-chemical potential with rising bombarding energy is consistent with the observations at higher energies going from SIS to RHIC.

According to [Cleymans and Redlich, 1999], at a bombarding energy of 1.0 AGeV, a temperature of  $T = 50$  MeV and a baryo-chemical potential of  $\mu_B = 850$  MeV are expected to be reached. With these parameters, pion ratios  $R_\pi = n_{\pi^-}/n_{\pi^+}$  of 3.7, 3.1, 1.8, and 1.05 for the reactions  $Au + Au$ ,  $Zr + Zr$ ,  $Ru + Ru$ , and  $Ca + Ca$  respectively are predicted with this model, which is not in agreement of the measurements at 1.0 GeV (figure 5.3).

The complete information accessible with the thermal model includes the temperature as the second parameter of the model. With the additional information of the particle yield the temperature can be determined. To do so the particle densities have to be converted to a particle number comparable to the mean number of pions per  $\langle A_{part} \rangle$ . The total number of pions  $N_\pi$  is given as:

$$N_\pi = (n_{\pi^-} + n_{\pi^0} + n_{\pi^+}) * V. \quad (6.4)$$

Since the number of participants in this model are the total number of particles in the colliding system  $A_{sys} = A_{projectile} + A_{target}$  the corresponding observable is

reaction	400 MeV	1000 MeV	1500 MeV
$^{197}\text{Au} + ^{197}\text{Au}$	$66 \pm 3$	$79 \pm 3$	$87 \pm 3$
$^{96}\text{Zr} + ^{96}\text{Zr}$	$62 \pm 3$	$76 \pm 3$	$87 \pm 3$
$^{96}\text{Ru} + ^{96}\text{Ru}$	$71 \pm 3$	$83 \pm 3$	$88 \pm 3$

**Table 6.2:** Extracted Temperatures for three energies and reactions

$N_\pi/A_{\text{sys}}$ . Figure 6.2 shows the relation of pion production and the temperature for given chemical potentials. In this diagram the possible temperatures can be found for the previously determined baryo-chemical potential  $\mu_B$ . The results are given in the following table 6.2. The errors are determined from the maximal variation in  $\mu_B$ . The rise of the temperature with increasing bombarding energy consistent with the picture of a heating of the system. Within errors the temperatures of the different systems are identical. The agreement gets best for the highest energy.

One has to note here, that the presented model can only be used as a guideline for the interpretation of the charged pion ratios for different reaction systems presented here. The model is definitely not adapted for this range of parameters which represent the low energy range examined today and in the future. Processes like light nuclei cluster formation ( $d, t, {}^3\text{He}, \alpha, \dots, {}^{12}\text{C}$ ) would need to be implemented for a consistent description. Additionally the “kink” visible for all baryo-chemical potentials (figure 6.1) arises due to computational problems and is not a physics property of the thermal model itself.

## 6.2 The iQMD Model

In order to model the HI reaction from known  $NN$  collision properties, events were generated with the isospin Quantum Molecular Model (iQMD) [Hartnack et al., 1998], [Hartnack, 1993], [Neise et al., 1990], [Bass, 1993], [Bass et al., 1995]. These events are used, as mentioned several times, as the input of the GEANT simulation of the **FOPI**-detector. IQMD is a microscopic transport model which explicitly takes the differences of the proton and neutron potentials and cross sections into account. In this section, the production of pions within the iQMD model is discussed briefly. The nucleons of two colliding nuclei are initialised within a sphere of a radius  $R = r_0 A^{1/3}$  with  $r_0 = 1.12$  fm [Bass et al., ]. The radii of the participating nuclei and the geometrical cross section,  $\sigma_{\text{geo}}$ , are given in table 6.3. The nucleons (as all baryons) are represented by a Gaussian shaped density distribution. The width of the Gaussian distribution is one of the input parameters of the model. It has to be mentioned explicitly at this point, that this parameter was set to a constant value of  $8.66 \text{ fm}^2$ . For  $\text{Ca} + \text{Ca}$  a value of

reaction	radius [fm]	$\sigma_{geo}$ [barn]
$^{197}\text{Au} + ^{197}\text{Au}$	6.52	5.34
$^{96}\text{Ru} + ^{96}\text{Ru}$	5.13	3.3
$^{40}\text{Ca} + ^{40}\text{Ca}$	3.83	1.84

**Table 6.3:** Radii and geometrical cross sections,  $\sigma_{geo}$ , for the simulated reactions.

$4.33 \text{ fm}^2$  is suggested in [Hartnack et al., 1998]. The value above was adjusted to the gold case, but for all other reactions the same value of the parameter was used as well.

The iQMD model is a microscopic quasi-classical transport model. Therefore, the hadrons are propagated under the influence of the potential according to Hamilton's equation of motion:

$$\dot{q}_i = -\frac{\partial H}{\partial p_i}, \quad \dot{p}_i = \frac{\partial H}{\partial q_i}. \quad (6.5)$$

with being  $H = T + V$ , where  $T$  denotes the kinetic energy and  $V$  the potential energy.

The potential energy,  $V$ , includes a Yukawa potential, the Coulomb potential between two nucleons and a momentum dependent potential<sup>4</sup>. In addition, two and three body skyrme forces and a symmetry potential are included. The symmetry potential ensures the correct distribution of protons and neutrons in the simulated nucleus. It depends explicitly on the  $I_3$  isospin component, and is responsible for the isospin relations in iQMD. The two initialised nuclei collide with the given energy and impact parameter.

### 6.2.1 iQMD and Pions

The only considered pion production process involves the creation and subsequent decay of  $\Delta$  resonances.

The  $\Delta$ s are produced, or better the nucleon is excited, in the following inelastic  $NN$ -reactions:

- $NN \rightarrow \Delta N$  (hard  $\Delta$  production)
- $\Delta \rightarrow N\pi$  ( $\Delta$  decay)
- $\Delta N \rightarrow NN$  ( $\Delta$  absorption)
- $N\pi \rightarrow \Delta$  (soft  $\Delta$ -production).

<sup>4</sup>For a detailed description of the potentials used within iQMD see [Bass et al., 1995].

The different isospin channels of the Delta decay are taken into account using the respective Clebsch-Gordan coefficients

$$\begin{aligned}
\Delta^{++} &\longrightarrow 1(p + \pi^+) \\
\Delta^+ &\longrightarrow \frac{2}{3}(p + \pi^0) + \frac{1}{3}(n + \pi^+) \\
\Delta^0 &\longrightarrow \frac{2}{3}(n + \pi^0) + \frac{1}{3}(p + \pi^-) \\
\Delta^- &\longrightarrow 1(n + \pi^-).
\end{aligned} \tag{6.6}$$

The isospin decomposition is shown explicitly in the appendix A on page 97.

Due to the large  $\pi N$  cross section, the pions are often reabsorbed. Within iQMD, it is possible to trace the motion of a pion throughout its lifetime. In [Bass et al., 1995] a pion-nucleon loop  $\Delta \rightarrow \pi \rightarrow \Delta$  is discussed. After four loops (three pion absorption events), the pion freezes out and does not interact anymore. The calculation in [Bass et al., 1995] were performed for  $Au + Au$  at an incident beam energy of 1.0 AGeV. The pions propagate in the nuclear medium with coulomb forces acting upon them, but without any elastic collisions [Bass et al., 1995]. The same is true for the  $\Delta$  resonance.

The creation of the  $\Delta$  resonance is controlled by the inelastic reaction cross section of the individual  $NN$  collision. The elastic and inelastic  $NN$  cross sections used in iQMD are given in [Hartnack et al., 1998] and presented in figure 6.3 as a function of the centre of mass energy,  $\sqrt{s}$ , of the colliding  $NN$  system. Same cross sections are used for proton-proton and neutron-neutron collisions [Hartnack et al., 1998]. Two inelastic proton-proton ( $pp$ ) collision cross sections are given. First the ‘‘total’’ inelastic cross section (in figure 6.3 labeled with  $pp$ -total -  $pp$ -elastic) and second the  $pp$  inelastic cross section from  $\pi^0$ . The latter is really used to determine the pion production cross section. The procedure to create a  $\Delta$  is implemented in iQMD as follows [Hartnack, 2002]:

When a  $NN$  collision takes place the probability for an elastic or inelastic collision is calculated according to the isospin composition of the colliding partners.  $nn$  and  $pp$  collisions are treated with the same cross section, the  $pp$  cross section in figure 6.3 and  $np$  collisions with the  $np$  cross section in figure 6.3. If the collision is considered as an inelastic one, the cross section for the creation of a  $\Delta$ -resonance is deduced from the cross section of the process  $n + p \rightarrow \pi^0 + X$ . The cross section,  $\sigma_{n+p \rightarrow \pi^0 + X}$ , depicted in figure 6.3, is scaled to match the inelastic cross section of  $np$  collisions at the low energy part since the  $\pi^0$  is created by the decay of a  $\Delta^+$  and a  $\Delta^0$ , but these are not the only decay modes of these two  $\Delta$ s. In order to get the  $\Delta$  production cross section for the considered collision ( $pp$ ,  $nn$ , or  $np$ ),  $\sigma_{n+p \rightarrow \pi^0 + X}$  is scaled according to Clebsch-Gordan coefficients due to the possible isospin channels.

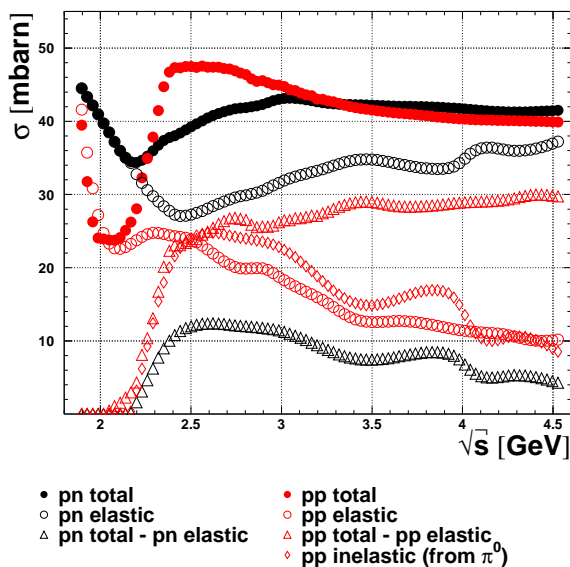


**Figure 6.3:** Elementary reaction cross section used in iQMD. Elastic and inelastic cross section of  $pp$  and  $np$  collisions as a function of the centre of mass energy  $\sqrt{s}$ . The  $np$  inelastic cross section deduced from the  $\pi^0$  production is used to determine the pion/ $\Delta$  production.

This leads to a loss of inelastic cross section, especially for the high energy range. A direct consequence of this is the low degree of stopping in the calculation for energies above 2.0 AGeV due to the missing degrees of freedom in which energy can dissipate to.

Since the iQMD model is used to derive a correction for the measured data using a Monte Carlo simulation (section 4.9 on page 53) a comparison of the pion data from this work with the iQMD model is shown in figure 6.4. The model calculations are done with four different sets of parameters that determine the EOS and the momentum dependence of the  $NN$ -interaction. A "soft" and a "hard" parametrisation of the EOS is used with compressibilities of 200 MeV and 380 MeV, respectively (indicated by s and h in figure 6.4). Both EOSs were calculated with and without momentum dependent  $NN$ -interactions. The momentum dependent interactions are well established [Aichelin, 1991], nevertheless the calculation without this dependency are included for educational purpose.

In contrast to the assumption in [Stock, 1986] the pion abundances do not depend on the EOS. In the  $Ca + Ca$  system, no dependence on the EOS was found, which is consistent with the expectation that in the case of a small system, the results are not sensitive to the underlying EOS. The sensitivity on the EOS increases with rising system size indicating that bulk effects are more pronounced in larger systems. But in the framework of iQMD this is not significant. In a model discussed later on the difference of the two parameterisations of the EOS is more pronounced (see 6.5). In general the soft EOS leads to more abundant pion production. The density gets higher in a soft scenario, and therefore the number

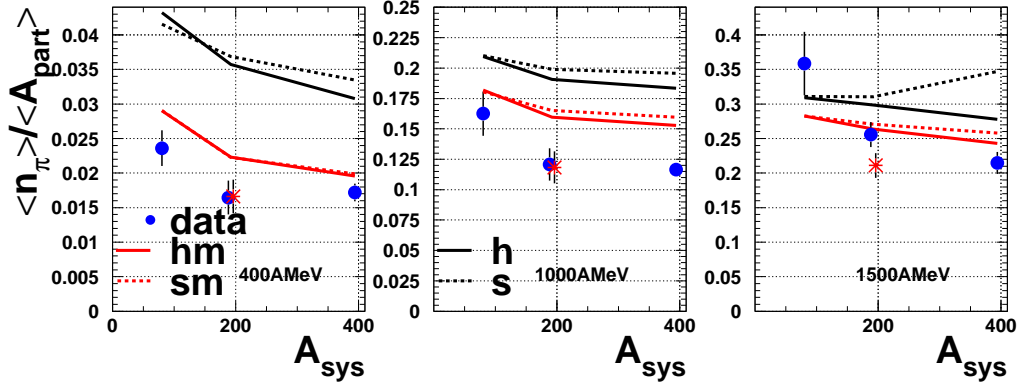


**Figure 6.4:** Comparison to the iQMD Model. A "soft" and "hard" EOS is used and displayed as dashed and solid lines, respectively. The calculations for the  $Zr + Zr$  system are on top of the calculation for  $Ru + Ru$  and not displayed in this figure.

of inelastic collisions, necessary to create a  $\Delta$ -resonance increases, which leads in total to a higher number of produced pions.

The calculation without momentum dependent interaction leads to higher pion yields for both versions of the EOS. To explain this observation, the same argument as for the EOS dependence can be used. The momentum dependent interaction pushes the nucleons apart so that the inelastic collisions get less frequent. With increasing bombarding energy, the differences in pion multiplicity due to the momentum dependent interactions get smaller. The model does not describe the size dependence of the pion multiplicities observed in the experimental data correctly. Especially for the highest energy, here the drop in pion numbers from Calcium to Gold gets less pronounced in the model as compared to the data. The overall agreement is in the order of 20% in the multiplicities of charged pions.

The charged pion ratios  $R_\pi$  from the iQMD model for all measured systems are compared to the data in figure 6.5. The ratios are extracted from the iQMD data from a linear fit to the pion multiplicity versus  $A_{part}$  in the same way as for the data.  $A_{part}$  in the case of iQMD is determined with the input impact parameter,  $b$ , using formula 4.6 (page 39). The ratios of the slopes of the individual fits for  $\pi^-$  and  $\pi^+$  for all measured systems and energies are given in figure 6.5 for both EOS parameterisations. The agreement of the simulation with the data is almost perfect. The perfect description of the data with the simulation lead to the discussion how this agreement is achieved by the theory. Since no higher resonances as the  $\Delta$ -resonance are included in iQMD the question of the pion production in iQMD was raised. The pion production within the framework of iQMD is already described above. The difference in the production cross section in  $np$

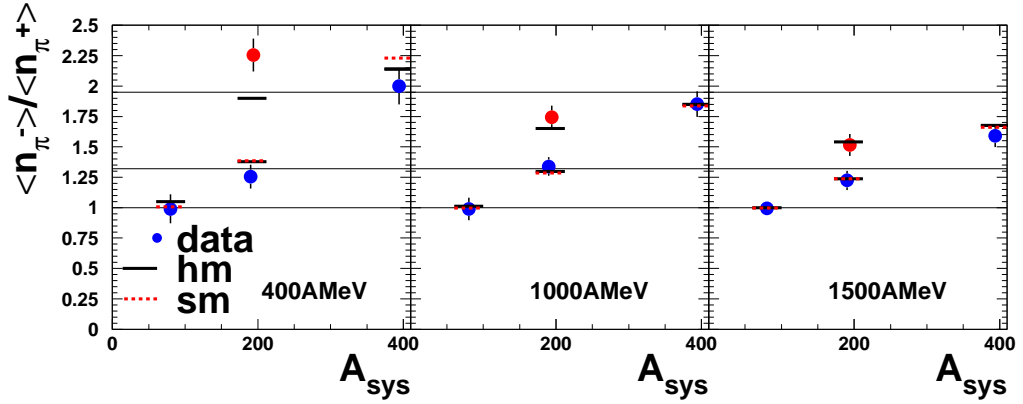


**Figure 6.5:** Pion ratios compared to the iQMD model. The model calculations are depicted as solid lines (hard EOS) and dashed lines (soft EOS).

and  $nn$  collisions is not the reason for the drop in the ratio. While iQMD and the isobar model agree very well for the low and mid-energy data (400, 1000 AMeV) for  $Ca + Ca$ ,  $Ru + Ru$ , and  $Au + Au$  the Zirconium system is only well described by the isobar prediction at 1000 AMeV. The difference of a factor of two in the  $np$  and  $nn$  cross section is implicitly included in the isobar model, where the coupling of  $n + p$  only the isospin  $I = 1$  state can couple to a  $\Delta$ . The  $np$  system is with the same probability in the  $I = 1$  and  $I = 0$  state (50%), which means that the probability to create a  $\Delta$  is twice as high in  $pp$  than in  $np$  collisions<sup>5</sup>(see appendix A on page 97). The dynamical evolution of the pions in the course of the collision is also not the reason of the good agreement. Transport models have the advantage that it is possible to switch of certain reactions. The pion ratio stays the same even if the pion is not allowed to do any reaction after the its creation. One possible explanation of the drop of the pion ratio,  $R_{\pi}$ , may be the mechanism of charge conservation. For high pion multiplicities (high colliding energies) the resulting effective  $N$  over  $Z$  ratio is shifted to lower numbers after the creation of negatively charged pions since there are no negative charges in the system at the beginning. At high energies multiple processes like the recollision of a nucleon from a  $\Delta$ -decay with the recreation of a  $\Delta$  gets more important and therefore the effective  $\frac{N}{Z}$  drops. This imagination describes not the deviation from the isobar model prediction for the Zirconium system at 400 AMeV incident energy.

<sup>5</sup>The  $I = 0$  resonance would be the  $N^*$  with a mass of 1440, MeV.

### 6.3 The BUU Model

A similar ansatz, based on the single particle distribution is followed by BUU-Models. The BUU abbreviation comes from the Boltzmann-Üling-Uhlenbeck (BUU) equation, which is solved in all models of this kind. In the nonrelativistic case, the BUU equation is written as follows [Hannuschke et al., 1991]:

$$\begin{aligned} \left\{ \frac{\partial}{\partial t} + \frac{\vec{p}}{m} \cdot \vec{\nabla}_r - \vec{\nabla}_r U \cdot \vec{\nabla}_p \right\} f(\vec{r}, \vec{p}, t) &= I_{collision} \\ &= \int \int d\vec{p}_2 d\vec{p}_3 \int d\Omega_4 |v_{12}| \frac{d\sigma}{d\Omega} (\vec{p}_2 - \vec{p}_4) \\ &\quad \times \delta^3(\vec{p}_1 + \vec{p}_2 - \vec{p}_3 - \vec{p}_4) \{ f_3 f_4 \bar{f}_1 \bar{f}_2 - f_1 f_2 \bar{f}_3 \bar{f}_4 \}. \end{aligned} \quad (6.7)$$

The left-hand side of this equation describes the time evolution of the single particle phase-space density  $f(\vec{r}, \vec{p}, t)$  in the presence of a mean field,  $U$ , which depends on the position, density, and eventually on the momentum. The evolution is determined by two body collisions. On the right hand side of the equation 6.7,  $I_{collision}$  is the collision term. Here, the momenta of the incoming particles,  $\vec{p}_1$  and  $\vec{p}_2$ , are connected to the outgoing particles  $\vec{p}_3, \vec{p}_4$  including the cross section  $\frac{d\sigma}{d\Omega}$  for this process. The Pauli principle is included in the last term of equation 6.7. In  $\{ f_3 f_4 \bar{f}_1 \bar{f}_2 - f_1 f_2 \bar{f}_3 \bar{f}_4 \}$ ,  $f$  are one-body distribution functions which act together as a blocking factor ( $f_1 f_2 \bar{f}_3 \bar{f}_4$ ) – the particles 1 and 2 stay in their original state) or an allowing factor ( $f_3 f_4 \bar{f}_1 \bar{f}_2$  – the particles 1 and 2 can go into the states 3 and 4). Note:  $\bar{f}_i = 1 - f(\vec{r}, \vec{p}_i, t)$  and  $|v_{12}|$  is the relative velocity of the colliding nucleons. The momentum conservation is guaranteed by the  $\delta^3(\vec{p}_1 + \vec{p}_2 - \vec{p}_3 - \vec{p}_4)$  term. The equation above is solved using the test-particle method. At  $t = 0$  the distribution function,  $f$ , is represented by an ensemble of of  $n(A_T + A_P)$  point-like test-particles. This can be interpreted as  $n$  parallel events, each with  $A_T$  target nucleons and  $A_P$  projectile nucleons.

The relativistic correct version of the BUU equation is described in [Blättel et al., 1993].

### 6.4 Different BUU Realisations

Different BUU realisations can be used for a comparison with the data. A recent approach [Larionov et al., 2001] tries to discuss the over-prediction of pion abundances of their so called standard calculation compared to [Pelte et al., 1997b]. The reaction cross section to create a resonance in a  $NN$ -collision is given by

$$\frac{d\sigma_{N_1 N_2 \rightarrow N_3 R_4}}{dM^2 d\Omega} = \frac{1}{64\pi^2} \overline{|\mathcal{M}|^2} \frac{p_{34}}{p_{12} \varepsilon^2} \mathcal{A}(M^2) \times 2(2J_R + 1), \quad (6.8)$$

where  $|\overline{\mathcal{M}}|^2$  is a spin averaged matrix element squared,  $p_{12}$  and  $p_{34}$  are c.m. momenta incoming and outgoing particles,  $\varepsilon$  is the total c.m. energy,  $\mathcal{A}(M^2)$  is the spectral function of the resonance  $R$ , and  $J_R$  is the spin of the resonance. For the inverse reaction, the cross section is

$$\frac{d\sigma_{N_3 R_4 \rightarrow N_1 N_2}}{d\Omega} = \frac{1}{64\pi^2} \overline{|\mathcal{M}|^2} \frac{p_{12}}{p_{34}\varepsilon^2} \times \frac{4}{C_{12}}. \quad (6.9)$$

with the same notation and  $C_{12}$  being equal to 2 if the nucleons  $N_1$  and  $N_2$  are identical and  $C_{12} = 1$  otherwise. According to the assumption of detailed balance, the matrix element  $\mathcal{M}$  has to be the same for both equations 6.8 and 6.9. To account for the pion data published in [Eskef et al., 1998] and [Pelte et al., 1997b], the authors introduced a density dependent matrix element in the following way:

$$|\overline{\mathcal{M}}|^2 = \kappa(\rho) |\overline{\mathcal{M}_{vac}}|^2 \quad \text{with} \quad \kappa(\rho) = \min(1, \max(0, 1 + \beta(\rho/\rho_0 - 1))), \quad \beta < 0 \quad (6.10)$$

The best agreement with the data from [Pelte et al., 1997b] was achieved for the given parametrisation of  $\kappa$  with  $\beta = -2$ . However, the scenario with  $\beta = -2$  can be ruled out by the data presented in this analysis. The resonance amplification with

$$\kappa = 1 + \beta \frac{\rho}{\rho_0}, \quad \beta > 0 \quad (6.11)$$

can also be ruled out since the data for the total pion production lies in between the  $\frac{\langle n_\pi \rangle}{\langle A_{part} \rangle} = 0.13$  for the amplified calculation ( $\beta = 3$ ) and the  $\frac{\langle n_\pi \rangle}{\langle A_{part} \rangle} = 0.08$  for the quenched resonance calculation ( $\beta = -2$ ). Further increase of  $\beta$  would not lead to a further decrease of the pion abundances [Larionov et al., 2001]. A slightly less quenched resonance calculation would agree with the presented data. It should be mentioned that the BUU standard calculation coincides with the iQMD calculation with a hard equation of state with no momentum dependent interaction. This already shows that in the different model approaches the pion production is not well under control.

## 6.5 The BEM Model

Another BUU approach gives a lower number of pions even in the case of the so called standard calculation. The results of these types of calculations are heavily depending on the default options of the respective author and the implementation of the program itself. The model of [Danielewicz, 1995] is called the Boltzmann Equation Model (BEM). This BUU type model gives different pion yields as compared to the previous one. As an example, the Gold system at 1 GeV is shown in figure 6.6. This is now a direct comparison of the data and the model diagrammed

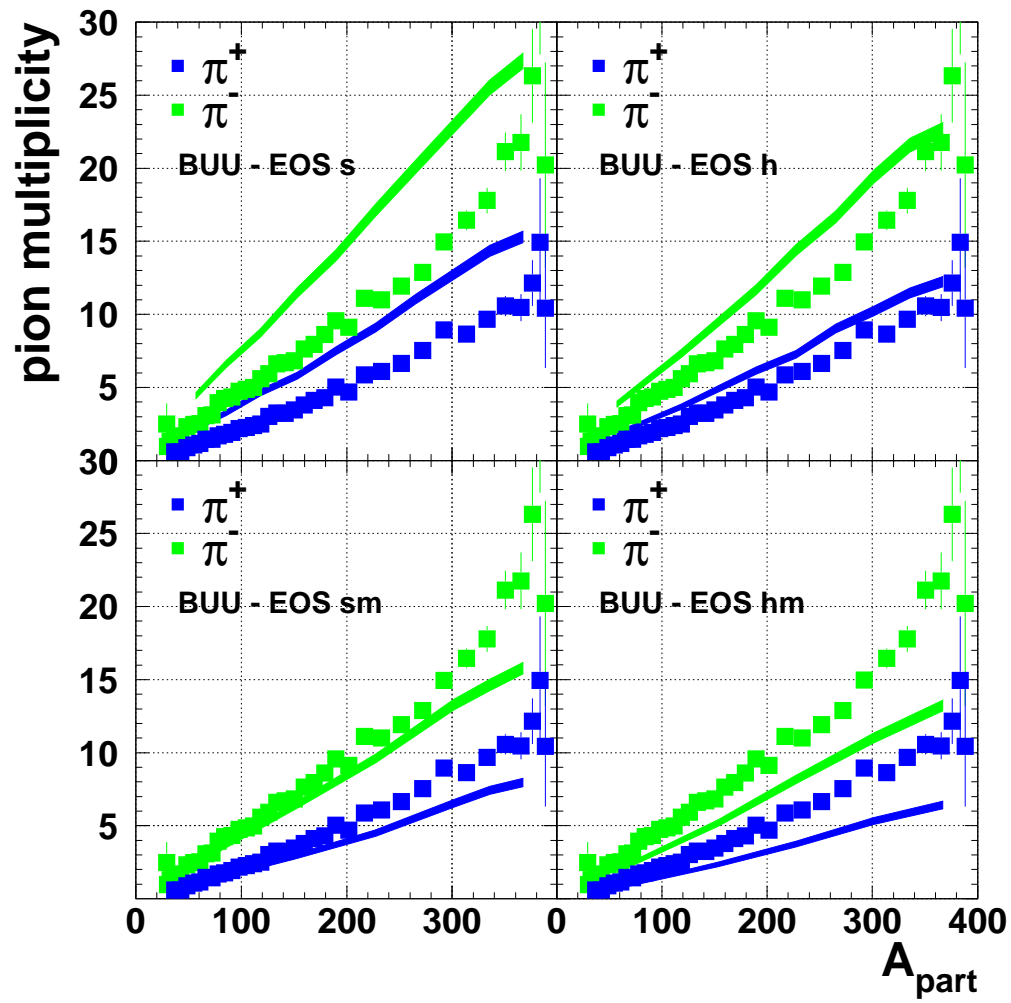


**Figure 6.6:** BUU Calculations by P. Danielewicz. The data points are indicated as squares, and the results of the calculation are given as a band [Danielewicz, 2001]

by the pion number versus the number of participants. In the case of the model calculation, the given impact parameter is used to derive  $A_{part}$  using equation 4.6 on page 39. The general trend in all models, that the results with momentum dependent interactions lead to a higher pion yield, is valid for this calculation, too. In contrast to the iQMD calculation, the BEM model of Danielewicz shows a sizable difference in the two versions of the EOS parameterisations, while the difference of the calculation with momentum dependent interactions and without are larger than in iQMD. The change from a soft to a hard EOS lowers the pion number of about 18%. The change from a calculation without momentum dependence to a momentum dependent calculation lowers the number of pions by a factor of 0.55. Since the momentum dependent interaction are well established, the best agreement with the data would be the choice of the calculation using a soft EOS. The Model gives in this case  $\frac{\langle \pi^- \rangle}{\langle A_{part} \rangle} = 0.021$ ,  $\frac{\langle \pi^+ \rangle}{\langle A_{part} \rangle} = 0.043$ , and  $\frac{\langle \pi_{tot} \rangle}{\langle A_{part} \rangle} = 0.096$ .

The different results and interpretations of the different models demonstrate the large uncertainties, that are still occurring in these type of calculations. To decide which of the models is the right one can only be deduced from a systematic comparison to the experimental data. In order to achieve this goal the experimental data has to be precise enough. The presented data in this work should be able to contribute to this intention. A final classification can only be achieved by a consistent description of different observables like pion production, strangeness production, radial-, side-, and elliptic flow with the same set of parameters.

## Chapter 7

# Conclusion and Outlook

The data of pion production as available for example at an energy of 1000 AMeV are not precise enough to draw a conclusion from or give a distinction between theoretical models. The main goal of this thesis is to give a systematic on the pion production at SIS energies. The **FOPI** device is used to revisit the problem of the pion production. In order to extract the pion numbers, the CDC is used to count the pions. The impact parameter  $b$  which is needed to extract the final observable, namely the mean number of pions,  $\langle n_\pi \rangle$ , per mean number of participants,  $\langle A_{part} \rangle$ , is deduced using different multiplicity variables. In the course of this thesis the functional dependence of the pion number on the number of participants is found to be linear. This fact was utilised to find the mean number of pions per mean number of participants directly with a linear fit.

With the data presented in this thesis a consistent analysis of the pion production is available for a large range of energies from 400 AMeV to 1500 AMeV and various systems  $Ca + Ca$ ,  $Ru + Ru$ ,  $Zr + Zr$ , and  $Au + Au$ . A clear system size dependence in the pion production is observed going from  $Ca + Ca$  to  $Au + Au$  reactions. The lightest system has about 35% more pions per participating nucleon than the two heavier systems. The charged pion ratio as a function of the initial isospin ratio  $\frac{N}{Z}$  shows a clear trend from an agreement to the  $(\frac{N}{Z})^2$  scaling, introduced by the isobar model, to a linear dependence on this quantity. With the help of a detailed Monte Carlo simulation a multiplicity dependent correction is deduced and applied to the data very successfully. The introduced corrections are well under control and allow the determination of the pion yield with an accuracy better than 10%. The charged pion ratio is even better determined with an error on the order of less than 5%. This accuracy is achieved with a full scale GEANT simulation which describes the detector response compared to the experiment very precise. The cross-check of detector variables between the experimental setup and the GEANT simulation is performed in the course of this thesis consistently for all systems. The simulation is found to be a very good description of the real de-

tor response. The error introduced by the simulation is on the order of 4%. The importance to introduce a transverse momentum dependent cut for pion tracks has been established.

The aim to give a consistent picture of the pion production is achieved in this work. The four systems and three energies are treated with the same method in order to reduce uncertainties due to different analysis attempts used in the past. Now a complete data set is available to compare with different model calculations.

The observed pion yields and pion ratios are compared intensively to different theoretical models. iQMD describes the data very reasonable. Especially the ratios are well under control in this theoretical framework. Even the change of the charged pion ratios as a function of the initial isospin ratio ( $N/Z$ ) from a quadratic to a linear dependence with rising energy is described. Within the iQMD model the sensitivity of the pion production observable on the equation of state is rather modest. This is different to the calculation of P. Danielewicz, where a dependence on the EOS is predicted. Compared to this model the experimental data would prefer a soft EOS with momentum interaction.

The comparison to a thermal model gives some hint on the temperatures of the hot and dense nuclear matter produced in this kind of Heavy Ion reactions. Within the accuracy of the model a consistent picture of temperatures and baryo-chemical potentials is deduced. At a bombarding energy of 1.5 AGeV a temperature of  $T = 87 \pm 3$  MeV and a baryo-chemical potential of  $\mu_B = 725 \pm 13$  MeV are reached independent of the colliding system.

For more extended studies, improvements, especially in the data acquisition sector were developed and tested. The operation principle of the new data acquisition was proven at a test scale in this work. The implementation of the changed FADC crates and the new SSM in the detector system is in progress. The changes will enable the **FOPI** collaboration to hunt for the deep subthreshold production of the  $\Xi^-$  [**FOPI** Collaboration, 2001].

From the perspective of this thesis the subject of pion production should be revisited with the upgraded **FOPI**-device, making use of the improved resolution and capabilities, so that the measurements of intermediate mass systems ( $A \approx 150$ ) and exotic  $\frac{N}{Z}$  ratios could complete the now available systematics.

## Appendix A

### Isospin Considerations

Isospin decomposition of the reactions 6.6 on page 87.

$$\begin{array}{llll}
 \Delta^{++} \longrightarrow \pi^+ + p & \left| \frac{3}{2}, \frac{3}{2} \right\rangle \rightarrow |1, 1\rangle \otimes \left| \frac{1}{2}, \frac{1}{2} \right\rangle & & 1 \\
 \Delta^+ \longrightarrow \pi^0 + p & \left| \frac{3}{2}, \frac{1}{2} \right\rangle \rightarrow |1, 0\rangle \otimes \left| \frac{1}{2}, \frac{1}{2} \right\rangle & & \frac{2}{3} \\
 \Delta^+ \longrightarrow \pi^+ + n & \left| \frac{3}{2}, \frac{1}{2} \right\rangle \rightarrow |1, 1\rangle \otimes \left| \frac{1}{2}, -\frac{1}{2} \right\rangle & & \frac{1}{3} \\
 \Delta^0 \longrightarrow \pi^- + p & \left| \frac{3}{2}, -\frac{1}{2} \right\rangle \rightarrow |1, -1\rangle \otimes \left| \frac{1}{2}, \frac{1}{2} \right\rangle & & \frac{1}{3} \\
 \Delta^0 \longrightarrow \pi^0 + n & \left| \frac{3}{2}, -\frac{1}{2} \right\rangle \rightarrow |1, 0\rangle \otimes \left| \frac{1}{2}, -\frac{1}{2} \right\rangle & & \frac{2}{3} \\
 \Delta^- \longrightarrow \pi^- + n & \left| \frac{3}{2}, -\frac{3}{2} \right\rangle \rightarrow |1, -1\rangle \otimes \left| \frac{1}{2}, -\frac{1}{2} \right\rangle & & 1 \quad (\text{A.1})
 \end{array}$$

with  $|I, I_3\rangle$  the isospin and the third component of the isospin. The third column in the equations A.1 shows the corresponding Clebsch-Gordan coefficient squared. Figure A.1 summarises the relevant Clebsch-Gordan coefficients for the production of the  $\Delta$  and the decay. In the above representation the production of the  $\Delta$  is

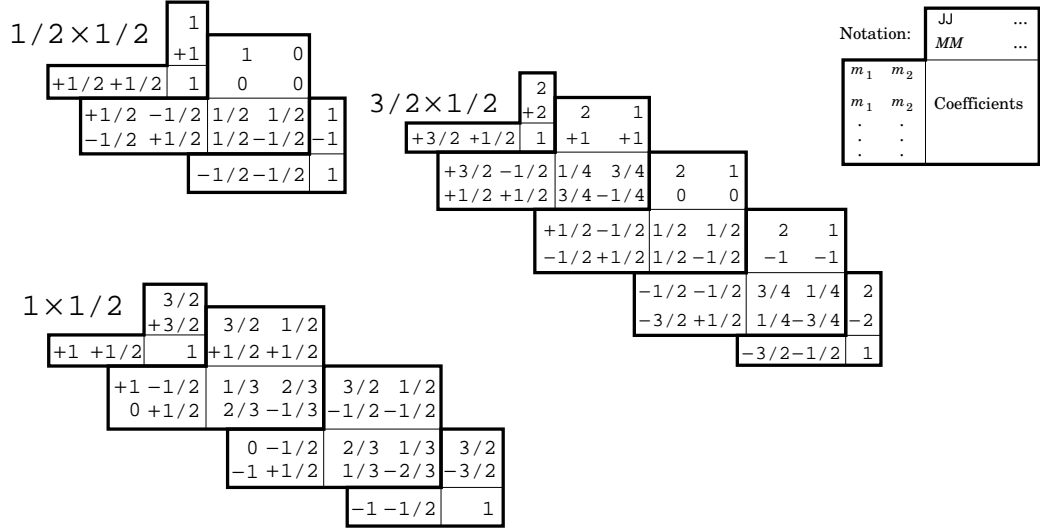


**Figure A.1:** The relevant Clebsch-Gordan coefficients [Groom et al., 2000].

written as:

$$\begin{aligned}
 pp &\longrightarrow n\Delta^{++} & |1, 1\rangle &\rightarrow \left| \frac{1}{2}, -\frac{1}{2} \right\rangle \otimes \left| \frac{3}{2}, \frac{3}{2} \right\rangle & \frac{3}{4} \\
 pp &\longrightarrow p\Delta^+ & |1, 1\rangle &\rightarrow \left| \frac{1}{2}, \frac{1}{2} \right\rangle \otimes \left| \frac{3}{2}, \frac{1}{2} \right\rangle & \frac{1}{4} \\
 pn &\longrightarrow n\Delta^+ & |1, 0\rangle &\rightarrow \left| \frac{1}{2}, -\frac{1}{2} \right\rangle \otimes \left| \frac{3}{2}, \frac{1}{2} \right\rangle & \frac{1}{2} \\
 pn &\longrightarrow p\Delta^0 & |1, 0\rangle &\rightarrow \left| \frac{1}{2}, \frac{1}{2} \right\rangle \otimes \left| \frac{3}{2}, -\frac{1}{2} \right\rangle & \frac{1}{2} \\
 nn &\longrightarrow n\Delta^0 & |1, -1\rangle &\rightarrow \left| \frac{1}{2}, -\frac{1}{2} \right\rangle \otimes \left| \frac{3}{2}, -\frac{1}{2} \right\rangle & \frac{1}{4} \\
 nn &\longrightarrow p\Delta^- & |1, -1\rangle &\rightarrow \left| \frac{1}{2}, \frac{1}{2} \right\rangle \otimes \left| \frac{3}{2}, -\frac{3}{2} \right\rangle & \frac{3}{4}
 \end{aligned} \tag{A.2}$$

Additionally, the  $pn$  reaction is suppressed by a factor of two, because for this system the probability is 50% to be in an  $I = 0$  state which can not couple to a  $\Delta$  resonance and a nucleon. This reduces the relative strength of this channel by a factor of two. In order to find the Clebsch-Gordan coefficients equations A.1 and A.2 have to be read as  $|JJ, MM\rangle \rightarrow |i_1, m_1\rangle \otimes |i_2, m_2\rangle$ , with  $i_i$  the isospin of the hadron. This notation picks up the notation from figure A.1 and must not be mistaken for the usual quantum numbers  $J$  and  $M$ .

# Appendix B

## Experiments

experiment	dst generation	run numbers
<i>Ca + Ca</i> 400 iQMD	00c vc25	1065-1211 00-19
<i>Ca + Ca</i> 1000 iQMD	00c c2f5	1741-1796 00-19
<i>Ca + Ca</i> 1500 iQMD	40b c2f5	1582-1685 02-19
<i>Ru + Ru</i> 400 iQMD	i25c12h vc25	3733-3844 00-19
<i>Ru + Ru</i> 1000 iQMD	ic25h00 c2f5	3845-3875 00-19
<i>Ru + Ru</i> 1500 iQMD	hc25h11 c2f5	4304-4314 00-19
<i>Zr + Zr</i> 400	i25c12h	2455-2552
<i>Zr + Zr</i> 1000	i25c12h	2688-2721
<i>Zr + Zr</i> 1500	hc25h12	3233-3348
<i>Au + Au</i> 400 iQMD	00c c2f5	1806-2025 00-19
<i>Au + Au</i> 1000 iQMD	10c vc25	2523-2642 00-19
<i>Au + Au</i> 1500 iQMD	02c c2f5	2915-3300 00-19

**Table B.1:** Summary of analysed dst generations and run numbers.

experiment	total number of events	selected events	background events
<i>Ca + Ca</i> 400	196976	94562	5698
<i>Ca + Ca</i> 1000	230329	88981	8322
<i>Ca + Ca</i> 1500	203847	67940	8794
<i>Ru + Ru</i> 400	43918	34347	1139
<i>Ru + Ru</i> 1000	55534	41580	760
<i>Ru + Ru</i> 1500	15903	11488	207
<i>Zr + Zr</i> 400	265657	151883	1252
<i>Zr + Zr</i> 1000	46286	20819	241
<i>Zr + Zr</i> 1500	225473	90605	2704
<i>Au + Au</i> 400	140998	67922	3931
<i>Au + Au</i> 1000	70125	30601	3353
<i>Au + Au</i> 1500	107433	46825	2241

**Table B.2:** Available events per experiment for the *MB + BARREL* trigger.

## Appendix C

### *d*0 Fit-Parameters

reaction	particle	P1	P2
<i>Au</i> + <i>Au</i> 400 AMeV experiment	$\pi^-$	0.29555	0.0016343
	$\pi^+$	0.35500	0.0048578
	protons	0.20203	0.012290
<i>Au</i> + <i>Au</i> 400 AMeV GEANT	$\pi^-$	0.18016	0.0012872
	$\pi^+$	0.16687	0.0059663
	protons	0.14889	0.0094222
<i>Au</i> + <i>Au</i> 1000 AMeV experiment	$\pi^-$	0.25445	0.00187980
	$\pi^+$	0.22575	0.0051119
	protons	0.18301	0.012328
<i>Au</i> + <i>Au</i> 1000 AMeV GEANT	$\pi^-$	0.18455	0.0012884
	$\pi^+$	0.17667	0.0055900
	protons	0.14031	0.0098014
<i>Au</i> + <i>Au</i> 1500 AMeV experiment	$\pi^-$	0.26679	0.0020516
	$\pi^+$	0.23042	0.0037760
	protons	0.16034	0.013694
<i>Au</i> + <i>Au</i> 1500 AMeV GEANT	$\pi^-$	0.25864	0.0024632
	$\pi^+$	0.22376	0.0039060
	protons	0.16840	0.013485

**Table C.1:** *d*0 parameters used for the *d*2*v* cut definition Au+Au.

reaction	particle	P1	P2
<i>Ru + Ru</i> 400 AMeV experiment	$\pi^-$	0.25198	0.0011376
	$\pi^+$	0.38905	0.0042666
	protons	0.10774	0.012941
<i>Ru + Ru</i> 400 AMeV GEANT	$\pi^-$	0.16278	0.0012184
	$\pi^+$	0.14252	0.0058431
	protons	0.13670	0.0095609
<i>Ru + Ru</i> 1000 AMeV experiment	$\pi^-$	0.21037	0.0016106
	$\pi^+$	0.17209	0.0022500
	protons	0.11673	0.012207
<i>Ru + Ru</i> 1000 AMeV GEANT	$\pi^-$	0.14469	0.0020570
	$\pi^+$	0.14149	0.0056038
	protons	0.13802	0.0093656
<i>Ru + Ru</i> 1500 AMeV experiment	$\pi^-$	0.19508	0.0015843
	$\pi^+$	0.15248	0.0037456
	protons	0.068528	0.014525
<i>Ru + Ru</i> 1500 AMeV GEANT	$\pi^-$	0.16287	0.0013897
	$\pi^+$	0.12650	0.0058049
	protons	0.12739	0.0094323

**Table C.2:** d0 parameters used for the d2v cut definition Ru+Ru.

reaction	particle	P1	P2
<i>Zr + Zr</i> 400 AMeV experiment	$\pi^-$	0.19491	0.001835
	$\pi^+$	0.23465	0.0022997
	protons	0.096682	0.012943
<i>Zr + Zr</i> 1000 AMeV experiment	$\pi^-$	0.21442	0.0015663
	$\pi^+$	0.16453	0.0023048
	protons	0.10505	0.012536
<i>Zr + Zr</i> 1500 AMeV experiment	$\pi^-$	0.16009	0.0023831
	$\pi^+$	0.12650	0.0058049
	protons	0.11699	0.010916

**Table C.3:** d0 parameters used for the d2v cut definition Zr+Zr.

reaction	particle	P1	P2
<i>Ca + Ca</i> 400 AMeV experiment	$\pi^-$	0.35370	0.0015477
	$\pi^+$	0.27939	0.0049069
	protons	0.18975	0.0049069
<i>Ca + Ca</i> 400 AMeV GEANT	$\pi^-$	0.14334	0.0016407
	$\pi^+$	0.10351	0.0055479
	protons	0.13578	0.0087621
<i>Ca + Ca</i> 1000 AMeV experiment	$\pi^-$	0.28397	0.0015919
	$\pi^+$	0.19809	0.0051954
	protons	0.19664	0.011914
<i>Ca + Ca</i> 1000 AMeV GEANT	$\pi^-$	0.15295	0.0012448
	$\pi^+$	0.11521	0.0055803
	protons	0.13324	0.0090872
<i>Ca + Ca</i> 1500 AMeV experiment	$\pi^-$	0.27335	0.0021286
	$\pi^+$	0.21617	0.0055254
	protons	0.19692	0.012149
<i>Ca + Ca</i> 1500 AMeV GEANT	$\pi^-$	0.14028	0.0017347
	$\pi^+$	0.15619	0.0044898
	protons	0.11379	0.010890

**Table C.4:** d0 parameters used for the d2v cut definition Ca+Ca.



## Appendix D

### Pion Production

The following tables summarise the pion production as determined by the free fit

$$n_{\pi}(A_{part}) = a_0 + a_1 A_{part} \quad (\text{D.1})$$

and the restricted fit with  $a_0 = 0$ , fit errors are included. The corrected data is indicated by the superscript  $c$ . All three determinations of  $A_{part}$  are included as well and indicated as  $n_{\pi}(m_i)$  with  $i \in \{cbp, ctrk, ptrk\}$ . The  $\pi^-$ ,  $\pi^+$ , and the sum of both are fitted separately and the results are listed in the tables.

	observable	$a_0(\pi^-)$	$a_0(\pi^+)$	$a_0(\pi^- + \pi^+)$	$a_1(\pi^-)$	$a_1(\pi^+)$	$a_1(\pi^- + \pi^+)$
400 AMeV	$n_\pi(m_{cbp})$	$-0.04602 \pm 0.00607$	$-0.01646 \pm 0.00384$	$-0.06436 \pm 0.00719$	$0.00562 \pm 7e-05$	$0.00283 \pm 4e-05$	$0.00851 \pm 8e-05$
	$n_\pi(m_{ctrk})$	$-0.04546 \pm 0.00656$	$0.01509 \pm 0.0043$	$-0.03742 \pm 0.00787$	$0.00538 \pm 6e-05$	$0.00243 \pm 4e-05$	$0.0079 \pm 7e-05$
	$n_\pi(m_{ptrk})$	$-0.02765 \pm 0.00825$	$0.01865 \pm 0.00558$	$-0.01159 \pm 0.01$	$0.00548 \pm 8e-05$	$0.0026 \pm 5e-05$	$0.00812 \pm 1e-04$
	$n_\pi^c(m_{cbp})$	$-0.05325 \pm 0.00806$	$-0.06618 \pm 0.00383$	$-0.11066 \pm 0.00903$	$0.00766 \pm 9e-05$	$0.00383 \pm 5e-05$	$0.01146 \pm 1e-04$
	$n_\pi^c(m_{ctrk})$	$-0.0549 \pm 0.0095$	$-0.02448 \pm 0.00525$	$-0.08247 \pm 0.01086$	$0.00754 \pm 9e-05$	$0.00341 \pm 5e-05$	$0.011 \pm 1e-04$
	$n_\pi^c(m_{ptrk})$	$-0.00111 \pm 0.00991$	$-0.03461 \pm 0.00511$	$-0.02951 \pm 0.01123$	$0.00738 \pm 1e-04$	$0.00371 \pm 6e-05$	$0.01106 \pm 0.00012$
	$n_\pi^c(m_{cbp})$	$0 \pm 0$	$0 \pm 0$	$0 \pm 0$	$0.00717 \pm 5e-05$	$0.00317 \pm 3e-05$	$0.01044 \pm 6e-05$
	$n_\pi^c(m_{ctrk})$	$0 \pm 0$	$0 \pm 0$	$0 \pm 0$	$0.0071 \pm 5e-05$	$0.00322 \pm 3e-05$	$0.01034 \pm 5e-05$
	$n_\pi^c(m_{ptrk})$	$0 \pm 0$	$0 \pm 0$	$0 \pm 0$	$0.00737 \pm 5e-05$	$0.00338 \pm 3e-05$	$0.01078 \pm 6e-05$
1000 AMeV	$n_\pi(m_{cbp})$	$-0.15076 \pm 0.03303$	$-0.09066 \pm 0.01824$	$-0.24401 \pm 0.03774$	$0.03849 \pm 0.00044$	$0.01883 \pm 0.00023$	$0.05739 \pm 0.0005$
	$n_\pi(m_{ctrk})$	$-0.11094 \pm 0.03458$	$-0.04655 \pm 0.01915$	$-0.16298 \pm 0.03955$	$0.03765 \pm 0.00044$	$0.01822 \pm 0.00023$	$0.05595 \pm 0.00049$
	$n_\pi(m_{ptrk})$	$0.09422 \pm 0.03718$	$0.0403 \pm 0.02056$	$0.13051 \pm 0.04259$	$0.03622 \pm 0.00045$	$0.01758 \pm 0.00024$	$0.05386 \pm 0.00051$
	$n_\pi^c(m_{cbp})$	$-0.36141 \pm 0.04129$	$-0.45087 \pm 0.02112$	$-0.81621 \pm 0.04646$	$0.05031 \pm 0.00058$	$0.02716 \pm 0.00031$	$0.07765 \pm 0.00066$
	$n_\pi^c(m_{ctrk})$	$-0.21116 \pm 0.04599$	$-0.38481 \pm 0.02351$	$-0.60223 \pm 0.05172$	$0.05047 \pm 0.00059$	$0.02714 \pm 0.00032$	$0.07773 \pm 0.00067$
	$n_\pi^c(m_{ptrk})$	$-0.07543 \pm 0.04962$	$-0.36219 \pm 0.02502$	$-0.45186 \pm 0.05565$	$0.04792 \pm 0.0006$	$0.02642 \pm 0.00032$	$0.07458 \pm 0.00068$
	$n_\pi^c(m_{cbp})$	$0 \pm 0$	$0 \pm 0$	$0 \pm 0$	$0.04613 \pm 0.00033$	$0.02153 \pm 0.00017$	$0.06804 \pm 0.00037$
	$n_\pi^c(m_{ctrk})$	$0 \pm 0$	$0 \pm 0$	$0 \pm 0$	$0.04827 \pm 0.00034$	$0.02284 \pm 0.00018$	$0.07135 \pm 0.00038$
	$n_\pi^c(m_{ptrk})$	$0 \pm 0$	$0 \pm 0$	$0 \pm 0$	$0.04716 \pm 0.00033$	$0.02245 \pm 0.00017$	$0.06993 \pm 0.00037$
1500 AMeV	$n_\pi(m_{cbp})$	$0.15016 \pm 0.0388$	$0.1768 \pm 0.02405$	$0.34046 \pm 0.04576$	$0.07235 \pm 0.00065$	$0.04004 \pm 0.00038$	$0.11239 \pm 0.00075$
	$n_\pi(m_{ctrk})$	$-0.03257 \pm 0.03581$	$0.22306 \pm 0.02351$	$0.17412 \pm 0.04293$	$0.07141 \pm 0.00056$	$0.03802 \pm 0.00033$	$0.10967 \pm 0.00065$
	$n_\pi(m_{ptrk})$	$1.07349 \pm 0.0481$	$0.76897 \pm 0.02948$	$1.83912 \pm 0.05642$	$0.06421 \pm 0.00064$	$0.03456 \pm 0.00037$	$0.09885 \pm 0.00074$
	$n_\pi^c(m_{cbp})$	$-0.20499 \pm 0.04094$	$-0.41083 \pm 0.02378$	$-0.59858 \pm 0.04749$	$0.08795 \pm 0.0007$	$0.05527 \pm 0.00043$	$0.14316 \pm 0.00083$
	$n_\pi^c(m_{ctrk})$	$-0.25321 \pm 0.04277$	$-0.33105 \pm 0.02638$	$-0.58849 \pm 0.05022$	$0.08893 \pm 0.00069$	$0.05488 \pm 0.00043$	$0.14393 \pm 0.00082$
	$n_\pi^c(m_{ptrk})$	$0.83331 \pm 0.05651$	$0.11585 \pm 0.03327$	$0.93693 \pm 0.06562$	$0.07955 \pm 0.00078$	$0.05072 \pm 0.00048$	$0.13049 \pm 0.00092$
	$n_\pi^c(m_{cbp})$	$0 \pm 0$	$0 \pm 0$	$0 \pm 0$	$0.08524 \pm 0.00045$	$0.04947 \pm 0.00027$	$0.13514 \pm 0.00053$
	$n_\pi^c(m_{ctrk})$	$0 \pm 0$	$0 \pm 0$	$0 \pm 0$	$0.0858 \pm 0.00044$	$0.05066 \pm 0.00027$	$0.13658 \pm 0.00052$
	$n_\pi^c(m_{ptrk})$	$0 \pm 0$	$0 \pm 0$	$0 \pm 0$	$0.08871 \pm 0.00047$	$0.05208 \pm 0.00029$	$0.14097 \pm 0.00055$

Table D.1: Pion production per  $A_{part}$  of the reaction  $Au + Au$  at 400 AMeV, 1000 AMeV and 1500 AMeV.

	observable	$a_0(\pi^-)$	$a_0(\pi^+)$	$a_0(\pi^- + \pi^+)$	$a_1(\pi^-)$	$a_1(\pi^+)$	$a_1(\pi^- + \pi^+)$
400 AMeV	$n_\pi(m_{cbp})$	$-0.00249 \pm 0.00564$	$0.00604 \pm 0.00465$	$0.00385 \pm 0.0073$	$0.00502 \pm 7e-05$	$0.00361 \pm 6e-05$	$0.00863 \pm 1e-04$
	$n_\pi(m_{ctrk})$	$-0.09567 \pm 0.00475$	$-0.04411 \pm 0.00395$	$-0.14104 \pm 0.00618$	$0.00579 \pm 6e-05$	$0.00392 \pm 5e-05$	$0.00972 \pm 8e-05$
	$n_\pi(m_{ptrk})$	$0.04814 \pm 0.00531$	$0.06836 \pm 0.00432$	$0.11538 \pm 0.00683$	$0.00433 \pm 6e-05$	$0.0027 \pm 5e-05$	$0.00704 \pm 8e-05$
	$n_\pi^c(m_{cbp})$	$0.0225 \pm 0.00731$	$-0.02173 \pm 0.00573$	$0.00099 \pm 0.00935$	$0.0061 \pm 1e-04$	$0.00486 \pm 8e-05$	$0.01097 \pm 0.00012$
	$n_\pi^c(m_{ctrk})$	$-0.11079 \pm 0.00649$	$-0.04736 \pm 0.00499$	$-0.1688 \pm 0.00822$	$0.00757 \pm 8e-05$	$0.0049 \pm 6e-05$	$0.01265 \pm 0.00011$
	$n_\pi^c(m_{ptrk})$	$0.05549 \pm 0.00669$	$0.05575 \pm 0.005$	$0.10845 \pm 0.00833$	$0.00577 \pm 8e-05$	$0.00374 \pm 6e-05$	$0.00957 \pm 1e-04$
	$n_\pi^c(m_{cbp})$	$0 \pm 0$	$0 \pm 0$	$0 \pm 0$	$0.00638 \pm 3e-05$	$0.00459 \pm 3e-05$	$0.01098 \pm 4e-05$
	$n_\pi^c(m_{ctrk})$	$0 \pm 0$	$0 \pm 0$	$0 \pm 0$	$0.00624 \pm 3e-05$	$0.00434 \pm 2e-05$	$0.01063 \pm 4e-05$
	$n_\pi^c(m_{ptrk})$	$0 \pm 0$	$0 \pm 0$	$0 \pm 0$	$0.00639 \pm 3e-05$	$0.00436 \pm 2e-05$	$0.01078 \pm 4e-05$
1000 AMeV	$n_\pi(m_{cbp})$	$0.25376 \pm 0.0271$	$0.34855 \pm 0.02192$	$0.60117 \pm 0.035$	$0.03919 \pm 0.00053$	$0.02636 \pm 0.00041$	$0.06561 \pm 0.00068$
	$n_\pi(m_{ctrk})$	$-0.10281 \pm 0.02293$	$0.06926 \pm 0.01837$	$-0.03946 \pm 0.02946$	$0.04314 \pm 0.00047$	$0.02926 \pm 0.00035$	$0.07254 \pm 0.00059$
	$n_\pi(m_{ptrk})$	$0.40168 \pm 0.03038$	$0.45423 \pm 0.02413$	$0.85323 \pm 0.03874$	$0.03714 \pm 0.00055$	$0.02466 \pm 0.00041$	$0.06186 \pm 0.00069$
	$n_\pi^c(m_{cbp})$	$0.00084 \pm 0.02719$	$0.02785 \pm 0.02224$	$0.03269 \pm 0.03524$	$0.04608 \pm 0.00057$	$0.03443 \pm 0.00046$	$0.08051 \pm 0.00073$
	$n_\pi^c(m_{ctrk})$	$-0.30325 \pm 0.02492$	$-0.2101 \pm 0.01972$	$-0.51411 \pm 0.03181$	$0.05196 \pm 0.00054$	$0.03859 \pm 0.00042$	$0.09058 \pm 0.00069$
	$n_\pi^c(m_{ptrk})$	$0.15251 \pm 0.03147$	$0.10932 \pm 0.02513$	$0.26503 \pm 0.04027$	$0.04465 \pm 0.0006$	$0.03367 \pm 0.00047$	$0.07831 \pm 0.00076$
	$n_\pi^c(m_{cbp})$	$0 \pm 0$	$0 \pm 0$	$0 \pm 0$	$0.0461 \pm 0.00028$	$0.03493 \pm 0.00022$	$0.0811 \pm 0.00036$
	$n_\pi^c(m_{ctrk})$	$0 \pm 0$	$0 \pm 0$	$0 \pm 0$	$0.04632 \pm 0.00028$	$0.03475 \pm 0.00022$	$0.08108 \pm 0.00035$
	$n_\pi^c(m_{ptrk})$	$0 \pm 0$	$0 \pm 0$	$0 \pm 0$	$0.04719 \pm 0.00029$	$0.03549 \pm 0.00023$	$0.08272 \pm 0.00037$
1500 AMeV	$n_\pi(m_{cbp})$	$-0.1265 \pm 0.08165$	$0.07433 \pm 0.07013$	$-0.04784 \pm 0.10782$	$0.07921 \pm 0.00195$	$0.06022 \pm 0.00161$	$0.13944 \pm 0.00254$
	$n_\pi(m_{ctrk})$	$-0.50659 \pm 0.06332$	$-0.2326 \pm 0.05456$	$-0.74023 \pm 0.08365$	$0.08092 \pm 0.00146$	$0.0615 \pm 0.00119$	$0.14246 \pm 0.00189$
	$n_\pi(m_{ptrk})$	$0.02659 \pm 0.08705$	$0.15153 \pm 0.07172$	$0.17575 \pm 0.11287$	$0.07618 \pm 0.00184$	$0.058 \pm 0.00148$	$0.13424 \pm 0.00236$
	$n_\pi^c(m_{cbp})$	$-0.0909 \pm 0.10198$	$-0.19051 \pm 0.08306$	$-0.28242 \pm 0.13178$	$0.09374 \pm 0.00228$	$0.07656 \pm 0.00187$	$0.17046 \pm 0.00296$
	$n_\pi^c(m_{ctrk})$	$-0.43816 \pm 0.08279$	$-0.44737 \pm 0.06759$	$-0.88621 \pm 0.10675$	$0.09894 \pm 0.00186$	$0.08009 \pm 0.00152$	$0.17913 \pm 0.0024$
	$n_\pi^c(m_{ptrk})$	$0.09775 \pm 0.09351$	$-0.10289 \pm 0.07317$	$0.0247 \pm 0.11923$	$0.08986 \pm 0.00207$	$0.07417 \pm 0.00166$	$0.16359 \pm 0.00266$
	$n_\pi^c(m_{cbp})$	$0 \pm 0$	$0 \pm 0$	$0 \pm 0$	$0.09194 \pm 0.00107$	$0.07275 \pm 0.00087$	$0.16485 \pm 0.00138$
	$n_\pi^c(m_{ctrk})$	$0 \pm 0$	$0 \pm 0$	$0 \pm 0$	$0.09057 \pm 0.00098$	$0.07146 \pm 0.00079$	$0.16213 \pm 0.00125$
	$n_\pi^c(m_{ptrk})$	$0 \pm 0$	$0 \pm 0$	$0 \pm 0$	$0.09174 \pm 0.00103$	$0.07214 \pm 0.00083$	$0.16407 \pm 0.00132$

Table D.2: Pion production per  $A_{part}$  of the reaction  $Ru + Ru$  at 400 AMeV, 1000 AMeV and 1500 AMeV.

	observable	$a_0(\pi^-)$	$a_0(\pi^+)$	$a_0(\pi^- + \pi^+)$	$a_1(\pi^-)$	$a_1(\pi^+)$	$a_1(\pi^- + \pi^+)$
400	$n_\pi(m_{ptrk})$	$0.11572 \pm 0.00939$	$0.05402 \pm 0.00529$	$0.17105 \pm 0.01065$	$0.00527 \pm 0.00011$	$0.00211 \pm 6e-05$	$0.00737 \pm 0.00012$
	$n_\pi^c(m_{ptrk})$	$0.01796 \pm 0.01086$	$-0.01549 \pm 0.00598$	$0.00451 \pm 0.01224$	$0.00769 \pm 0.00013$	$0.00341 \pm 7e-05$	$0.01108 \pm 0.00015$
	$n_\pi^c(m_{ptrk})$	$0 \pm 0$	$0 \pm 0$	$0 \pm 0$	$0.00789 \pm 4e-05$	$0.00323 \pm 2e-05$	$0.01113 \pm 4e-05$
1000	$n_\pi(m_{ptrk})$	$0.45542 \pm 0.07317$	$0.32592 \pm 0.04314$	$0.77858 \pm 0.08494$	$0.0385 \pm 0.00095$	$0.01965 \pm 0.00055$	$0.0582 \pm 0.0011$
	$n_\pi^c(m_{ptrk})$	$-0.53946 \pm 0.06811$	$-0.37649 \pm 0.04105$	$-0.91944 \pm 0.07993$	$0.05008 \pm 0.00096$	$0.02873 \pm 0.00058$	$0.0789 \pm 0.00113$
	$n_\pi^c(m_{ptrk})$	$0 \pm 0$	$0 \pm 0$	$0 \pm 0$	$0.04294 \pm 0.00035$	$0.02376 \pm 0.00021$	$0.06674 \pm 0.0004$
1500	$n_\pi(m_{ptrk})$	$0.76445 \pm 0.05009$	$0.70467 \pm 0.03325$	$1.46932 \pm 0.06029$	$0.06628 \pm 0.0007$	$0.03865 \pm 0.00045$	$0.10493 \pm 0.00084$
	$n_\pi^c(m_{ptrk})$	$-0.34869 \pm 0.05021$	$-0.31711 \pm 0.0336$	$-0.66566 \pm 0.06059$	$0.08327 \pm 0.00076$	$0.05481 \pm 0.00051$	$0.1381 \pm 0.00092$
	$n_\pi^c(m_{ptrk})$	$0 \pm 0$	$0 \pm 0$	$0 \pm 0$	$0.07841 \pm 0.00029$	$0.05039 \pm 0.0002$	$0.12882 \pm 0.00035$

**Table D.3:** Pion production per  $A_{part}$  of the reaction  $Zr + Zr$  at 400A MeV, 1000A MeV and 1500A MeV.

	observable	$a_0(\pi^-)$	$a_0(\pi^+)$	$a_0(\pi^- + \pi^+)$	$a_1(\pi^-)$	$a_1(\pi^+)$	$a_1(\pi^- + \pi^+)$
400	$n_\pi(m_{cbp})$	$0.03911 \pm 0.00366$	$0.06352 \pm 0.00383$	$0.10212 \pm 0.0053$	$0.00585 \pm 0.00014$	$0.00561 \pm 0.00014$	$0.01149 \pm 0.0002$
	$n_\pi^c(m_{cbp})$	$0.00769 \pm 0.00404$	$0.00794 \pm 0.00355$	$0.01633 \pm 0.00543$	$0.00772 \pm 0.00015$	$0.0078 \pm 0.00013$	$0.01574 \pm 0.0002$
	$n_\pi^c(m_{cbp})$	$0 \pm 0$	$0 \pm 0$	$0 \pm 0$	$0.00797 \pm 7e-05$	$0.00806 \pm 7e-05$	$0.01627 \pm 1e-04$
1000 AMeV	$n_\pi(m_{cbp})$	$-0.01514 \pm 0.01245$	$0.01613 \pm 0.01281$	$0.0009 \pm 0.01786$	$0.04427 \pm 0.00056$	$0.04575 \pm 0.00057$	$0.09006 \pm 0.0008$
	$n_\pi(m_{ctrk})$	$-0.20924 \pm 0.0155$	$-0.10116 \pm 0.01517$	$-0.29615 \pm 0.02185$	$0.04957 \pm 0.00058$	$0.04738 \pm 0.00056$	$0.09662 \pm 0.00081$
	$n_\pi(m_{ptrk})$	$0.0707 \pm 0.01228$	$0.17526 \pm 0.01237$	$0.24397 \pm 0.01746$	$0.04239 \pm 0.00049$	$0.03928 \pm 0.00048$	$0.08181 \pm 0.00069$
	$n_\pi^c(m_{cbp})$	$-0.16048 \pm 0.01418$	$-0.11049 \pm 0.01449$	$-0.27417 \pm 0.02024$	$0.05376 \pm 0.00059$	$0.05435 \pm 0.0006$	$0.10832 \pm 0.00084$
	$n_\pi^c(m_{ctrk})$	$-0.24185 \pm 0.0189$	$-0.06099 \pm 0.01824$	$-0.31928 \pm 0.02663$	$0.06071 \pm 0.0007$	$0.05578 \pm 0.00066$	$0.11764 \pm 0.00098$
	$n_\pi^c(m_{ptrk})$	$0.03813 \pm 0.01672$	$0.06559 \pm 0.01707$	$0.10375 \pm 0.02406$	$0.0498 \pm 0.00071$	$0.0508 \pm 0.00072$	$0.1006 \pm 0.00102$
	$n_\pi^c(m_{cbp})$	$0 \pm 0$	$0 \pm 0$	$0 \pm 0$	$0.04771 \pm 0.00024$	$0.05023 \pm 0.00025$	$0.09805 \pm 0.00035$
	$n_\pi^c(m_{ctrk})$	$0 \pm 0$	$0 \pm 0$	$0 \pm 0$	$0.05242 \pm 0.00027$	$0.05375 \pm 0.00028$	$0.10686 \pm 0.00039$
	$n_\pi^c(m_{ptrk})$	$0 \pm 0$	$0 \pm 0$	$0 \pm 0$	$0.05129 \pm 0.00028$	$0.05335 \pm 0.00029$	$0.10465 \pm 0.0004$
1500 AMeV	$n_\pi(m_{cbp})$	$-0.26413 \pm 0.01147$	$-0.15998 \pm 0.01247$	$-0.35005 \pm 0.01766$	$0.11588 \pm 0.0011$	$0.10744 \pm 0.00113$	$0.21899 \pm 0.0016$
	$n_\pi(m_{ctrk})$	$0.32516 \pm 0.01884$	$0.43856 \pm 0.01807$	$0.75938 \pm 0.02614$	$0.08371 \pm 0.00095$	$0.07255 \pm 0.00087$	$0.15655 \pm 0.00129$
	$n_\pi(m_{ptrk})$	$0.3839 \pm 0.01884$	$0.4317 \pm 0.01838$	$0.8163 \pm 0.02634$	$0.08491 \pm 0.00114$	$0.07717 \pm 0.00109$	$0.16208 \pm 0.00158$
	$n_\pi^c(m_{cbp})$	$-0.02058 \pm 0.02225$	$-0.05947 \pm 0.02166$	$-0.07938 \pm 0.0311$	$0.1191 \pm 0.00151$	$0.11972 \pm 0.00149$	$0.23889 \pm 0.00212$
	$n_\pi^c(m_{ctrk})$	$0.78014 \pm 0.02791$	$0.85321 \pm 0.02595$	$1.62429 \pm 0.03808$	$0.09721 \pm 0.00129$	$0.0849 \pm 0.00117$	$0.18277 \pm 0.00174$
	$n_\pi^c(m_{ptrk})$	$0.67682 \pm 0.02524$	$0.59919 \pm 0.0238$	$1.27593 \pm 0.03474$	$0.08894 \pm 0.00142$	$0.08712 \pm 0.00136$	$0.17611 \pm 0.00197$
	$n_\pi^c(m_{cbp})$	$0 \pm 0$	$0 \pm 0$	$0 \pm 0$	$0.11786 \pm 0.00069$	$0.11609 \pm 0.00068$	$0.23407 \pm 0.00097$
	$n_\pi^c(m_{ctrk})$	$0 \pm 0$	$0 \pm 0$	$0 \pm 0$	$0.12715 \pm 0.00072$	$0.11649 \pm 0.00066$	$0.24418 \pm 0.00098$
	$n_\pi^c(m_{ptrk})$	$0 \pm 0$	$0 \pm 0$	$0 \pm 0$	$0.12206 \pm 0.0007$	$0.11674 \pm 0.00068$	$0.23884 \pm 0.00098$

Table D.4: Pion production per  $A_{part}$  of the reaction  $Ca + Ca$  at 400 AMeV, 1000 AMeV and 1500 AMeV.



---

## Bibliography

- [Aichelin, 1991] Aichelin, J. (1991). "Quantum" molecular dynamics: A dynamical microscopic n body approach to investigate fragment formation and the nuclear equation of state in heavy ion collisions. *Phys. Rept.*, 202:233–360.
- [Averbeck et al., 1997] Averbeck, R., Doepenschmidt, A., Appenheimer, M., Charbonnier, Y., Diaz, J., Hejny, V., Hlavac, S., Holzmann, R., Kugler, A., Lefevre, F., Loehner, H., Marin, A., Metag, V., Niebur, W., Novotny, R., Ostendorf, R., Pleskac, R., Schubert, A., Schutz, Y., Siemssen, R., Simon, R., Stratmann, R., Stroehel, H., Tlustý, P., Vogt, P., Wagner, V., Weiss, J., Wilschut, H., Wissmann, F., Wolf, A., and Wolf, M. (1997). Production of  $\pi^0$  and eta mesons in carbon-induced relativistic heavy ion collisions. *Z. Phys.*, A359:65–73.
- [Bass, 1993] Bass, S. (1993). Kollektive Effekte von Pionen bei SIS-Energien. Master's thesis, Universität Frankfurt.
- [Bass et al., 1995] Bass, S., Hartnack, C., Stöcker, H., and Greiner, W. (1995). Azimuthal correlations of pions in relativistic heavy-ion collisions at 1 GeV/nucleon. *Phys. Rev. C*, 51(6):3343–3356.
- [Bass et al., ] Bass, S. A., Hartnack, C., and Stöcker, H. Running The IQMD program.
- [Berg et al., 1994] Berg, F., Pfeiffer, M., Schwalb, O., Franke, M., Kuhn, W., Loehner, H., Metag, V., Notheisen, M., Novotny, R., Raschke, A., Ritman, J., Roebig-Landau, M., Simon, R., Sumbera, M., Venema, L., and Wilschut, H. (1994). Transverse momentum distributions of eta mesons in near threshold relativistic heavy ion reactions. *Phys. Rev. Lett.*, 72:977–980.
- [Best et al., 1997] Best, D., Herrmann, N., Hong, B., Kirejczyk, M., Ritman, J., Wiśniewski, K., Zhilin, A., Gobbi, A., Hildenbrand, K., Leifels, Y., Pinkenburg, C., Reisdorf, W., Schüll, D., Sodan, U., Wang, G., Wienold, T., Alard, J., Amouroux, V., Bastid, N., Belyaev, I., Berek, G., Biegansky, J., Cherbachev, R., Coffin, J., Crochet, P., Dupieux, P., Fodor, Z., Genoux-Lubain, A., Goebels,

- G., Guillaume, G., Häfele, E., Jundt, F., Kecskemeti, J., Korchagin, Y., Kotte, R., Kuhn, C., Lebedev, A., Lebedev, A., Legrand, I., Maazouzi, C., Manko, V., Mosner, J., Mohren, S., Moisa, D., Neubert, W., Pelte, D., Petrovici, M., Pras, P., Rami, F., Roy, C., Seres, Z., Sikora, B., Simion, V., Siwek-Wilczyńska, K., Smolyankin, V., Somov, A., Tizniti, L., Trzaska, M., Vasilev, M., Wagner, P., Wohlfarth, D., and Yushmanov, I. (1997).  $K^+$  production in the reaction  $^{58}\text{Ni} + ^{58}\text{Ni}$  at incident energies from 1 AGeV to 2 AGeV. *Nucl. Phys.*, A625:307–324. nucl-ex/9704005.
- [Billoir, 1984] Billoir, P. (1984). TRACK FITTING WITH MULTIPLE SCATTERING: A NEW METHOD. *Nucl. Instr. Meth.*, A225:352.
- [Blättel et al., 1993] Blättel, B., Koch, V., and Mosel, U. (1993). Transport theoretical analysis of relativistic heavy ion collisions. *Rept. Prog. Phys.*, 56:1–62.
- [Blum and Rolandi, 1994] Blum, W. and Rolandi, L. (1994). *Particle Detection with Drift Chambers*. Springer-Verlag.
- [Braun-Munzinger et al., 1999] Braun-Munzinger, P., Heppe, I., and Stachel, J. (1999). Chemical equilibration in  $Pb + Pb$  collisions at the SPS. *Phys. Lett.*, B465:15–20. nucl-th/9903010.
- [Braun-Munzinger et al., 2001] Braun-Munzinger, P., Magestro, D., Redlich, K., and Stachel, J. (2001). Hadron production in  $Au - Au$  collisions at RHIC. *Phys. Lett.*, B518:41–46. hep-ph/0105229.
- [Braun-Munzinger et al., 1984] Braun-Munzinger, P., Paul, P., Ricken, L., Stachel, J., Zhang, P., Young, G., Obenshain, F., and Grosse, E. (1984). Pion production in heavy ion collisions at  $E_{LAB}/A = 35\text{MeV}$ . *Phys. Rev. Lett.*, 52:255–258.
- [Braun-Munzinger and Stachel, 1987] Braun-Munzinger, P. and Stachel, J. (1987). Pion production in heavy ion collisions. *Ann. Rev. Nucl. Part. Sci.*, 37:97–131.
- [Braun-Munzinger et al., 1995] Braun-Munzinger, P., Stachel, J., Wessels, J. P., and Xu, N. (1995). Thermal equilibration and expansion in nucleus-nucleus collisions at the AGS. *Phys. Lett.*, B344:43–48. nucl-th/9410026.
- [Braun-Munzinger et al., 1996] Braun-Munzinger, P., Stachel, J., Wessels, J. P., and Xu, N. (1996). Thermal and hadrochemical equilibration in nucleus-nucleus collisions at the SPS. *Phys. Lett.*, B365:1–6. nucl-th/9508020.
- [Brosch, 2001] Brosch, O. (2001). Phd. thesis in preparation, Universität Mannheim. private communication.

- 
- [Brosch et al., 2000] Brosch, O., Hesser, J., Hinkelbein, C., Kornmesser, K., Kuberka, T., Kugel, A., Männer, R., Singpiel, H., and Vettermann, B. (2000). ATLANTIS, a Hybrid FPGA/RISC Based Re-configurable System. *Springer LNCS*, 1800:890–897. <http://link.springer.de/link/service/series/0558/bibs/1800/18000890.htm>.
- [Brun et al., 1987] Brun, R., Bruyant, F., Maire, M., McPherson, A. C., and Zanarini, P. (1987). GEANT3. (CERN DD/EE/84-1). the simulations are all based on this program.
- [Cassing et al., 1997] Cassing, W., Bratkovskaya, E., Mosel, U., Teis, S., and Sibirtsev, A. (1997). Kaon versus antikaon production at SIS energies. *Nucl. Phys.*, A614:415–432. nucl-th/9609050.
- [Cassing and Bratkovskaya, 1999] Cassing, W. and Bratkovskaya, E. L. (1999). Hadronic and electromagnetic probes of hot and dense nuclear matter. *Phys. Rept.*, 308:65–233.
- [Cavata et al., 1990] Cavata, C., Demoulin, M., Gosset, J., Lemaire, M.-C., L'Hôte, D., J.Poitou, and O.Vallete (1990). Determination of the impact parameter in relativistic nucleus-nucleus collisions. *Phys. Rev. C*, 42(4):1760–1763.
- [Cleymans and Redlich, 1999] Cleymans, J. and Redlich, K. (1999). Chemical and thermal freeze-out parameters from 1 AGeV to 200 AGeV. *Phys. Rev.*, C60:054908 1–9. nucl-th/9903063.
- [Danielewicz, 1995] Danielewicz, P. (1995). Effects of compression and collective expansion on particle emission from central heavy ion reactions. *Phys. Rev.*, C51:716–760.
- [Danielewicz, 2001] Danielewicz, P. (2001). Private communication. BEM Model Calculations.
- [Devimes, 2001] Devimes, A. (2001).  $K^+$  production in heavy ion collisions at 1.5 GeV. PhD thesis, Technische Universität Darmstadt.
- [Eskef et al., 1998] Eskef, M., Pelte, D., Goebels, G., Häfele, E., Herrmann, N., Korolija, M., Leifels, Y., Merlitz, H., Mohren, S., Stockmeier, M., Trzaska, M., Alard, J., Andronic, A., Auerbeck, R., Basrak, Z., Bastid, N., Belyaev, I., Best, D., Buta, A., Caplar, R., Cindro, N., Coffin, J., Crochet, P., Dupieux, P., Dzelalija, M., Fraysse, L., Fodor, Z., Genoux-Lubain, A., Gobbi, A., Hildenbrand, K., Hong, B., Jundt, F., Kecskemeti, J., Kirejczyk, M., Kotte, R., Kutsche, R., Lebedev, A., Manko, V., Mosner, J., Moisa, D., Neubert, W., Plettner,

- C., Pras, P., Rami, F., Ramillien, V., Reisdorf, W., Ritman, J., de Schauenburg, B., Schüll, D., Seres, Z., Sikora, B., Simion, V., Siwek-Wilczyńska, K., Smolyankin, V., Vasilev, M., Wagner, P., Wang, G., Wiśniewski, K., Wohlfarth, D., and Zhilin, A. (1998). Identification of baryon resonances in central heavy-ion collisions at energies between 1 AGeV and 2 AGeV. *Eur. Phys. J.*, A3:335–349. nucl-ex/9809005.
- [Geissel et al., 2000] Geissel, H., Gilg, H., Gillitzer, A., Hayano, R., Hirenzaki, S., Itahashi, K., Iwasaki, M., Kienle, P., Munch, M., Münzenberg, G., Schott, W., Suzuki, K., Tomono, D., Weick, H., Yamazaki, T., and Yoneyama, T. (2000). Observation of well-resolved 1s and 2p  $\pi^-$  states in *Pb* by high resolution (*d*,  $^3\text{He}$ ) spectroscopy. *Nucl. Phys.*, A663:206–209.
- [Gillitzer, 2001] Gillitzer, A. (2001). Deeply bound pionic atoms. Prepared for Hirschegg '01: Structure of Hadrons: 29th International Workshop on Gross Properties of Nuclei and Nuclear Excitations, Hirscheegg, Austria, 14-20 Jan 2001.
- [Gobbi et al., 1993] Gobbi, A., Alard, J., Augustinski, G., Basrak, Z., Bastid, N., Belaev, I., Blaich, T., Boccaccio, P., Bock, R., Boussange, S., Buta, A., Caplar, R., Cerruti, C., Charity, R., Cindro, N., Coffin, J., Crouau, M., Daudon, F., Devin, J., Dupieux, P., Ero, J., Fan, Z., Fayard, C., Fintz, P., Fodor, Z., Fraysse, L., Freifelder, R., Frolov, S., Giminez, E., Grigorian, Y., Guillaume, G., Herrmann, N., Hildenbrand, K., Holbling, S., Hornecker, F., Houari, A., Jeong, S., Jorio, M., Jundt, F., Kecskemeti, J., Koncz, P., Korchagin, Y., Kotte, R., Kramer, M., Kuhn, C., Lebedev, A., Legrand, I., Maguire, C., Manko, V., Marquardt, M., Matulewicz, T., Mayade, S., Mgebrishvili, G., Mosner, J., Moisa, D., Montarou, G., Montbel, I., Morel, P., Neubert, W., Neunlist, R., Ortlepp, G., Pelte, D., Petrovici, M., Rami, F., Reisdorf, W., Saettel, M., Sahuc, E., Savinel, G., Seres, Z., Schüll, D., Sikora, B., Simion, V., Smolyankin, S., Soudan, U., Tanaka, M., Teh, K., Tezkratt, R., Tischler, B., Trzaska, M., Vasilev, M., Vincent, D., Wagner, P., Weinert, J., Wessels, J., Wienold, T., Wilhelmi, Z., Wohlfarth, D., and Zhilin, A. (1993). A highly segmented  $\Delta E$ -time-of-flight wall as forward detector of the  $4\pi$ -system for charged particles at the SIS/ESR accelerator. *Nucl. Instrum. Meth.*, A324:156–176.
- [Gosset et al., 1977] Gosset, J., Gutbrot, H., Meyer, W., Postkanzer, M., Sandoval, A., Stock, R., and Westfall, G. (1977). Central collisions of relativistic heavy ions. *Phys. Rev. C*, 16(2):629–657.
- [Groom et al., 2000] Groom, D. E. et al. (2000). Review of particle physics. *Eur. Phys. J.*, C15:1.

- 
- [Hannuschke et al., 1991] Hannuschke, S., Cassing, W., Mosel, U., and Niita, K. (1991). Microscopic analysis of deeply inelastic heavy-ion collisions. *Nucl. Phys.*, A535:120–136.
- [Harris et al., 1985] Harris, J. W., Bock, R., Brockmann, R., Sandoval, A., Stock, R., Stroebale, H., Odynic, G., Pugh, H., Schroeder, L., Renfordt, R., Schall, D., Bangert, D., Rauch, W., and Wolf, K. (1985). Pion production as a probe of the nuclear matter equation of state. *Phys. Lett.*, B153:377–381.
- [Harris et al., 1987] Harris, J. W., Odyniec, G., Pugh, H., Schroeder, L., Tincknell, M., Rauch, W., Stock, R., Bock, R., Brockmann, R., Sandoval, A., Stroebale, H., Renfordt, R., Schall, D., Bangert, D., Sullivan, J., Wolf, K., Dacal, A., Guerra, C., and Ortiz, M. (1987). Pion production in high-energy nucleus nucleus collisions. *Phys. Rev. Lett.*, 58:463–466.
- [Hartnack, 1993] Hartnack, C. (1993). *Beschreibung von Flußeffecten und Teilchenproduktion in relativistischen Schwerionensößen*. PhD thesis, Universität Frankfurt.
- [Hartnack, 2002] Hartnack, C. (2002). Private communication. Pion in the iQMD model.
- [Hartnack et al., 2001] Hartnack, C., Oeschler, H., and Aichelin, J. (2001). What determines the  $k^-$  multiplicity at energies around 1 AGeV - 2 AGeV. nucl-th/0109016.
- [Hartnack et al., 1998] Hartnack, C., Puri, R. K., Aichelin, J., Bass, J. K. S., Stöcker, H., and Greiner, W. (1998). Modelling the many-body dynamics of heavy ion collisions: Present status and future perspective. *Eur. Phys. J.*, A1:151–169. nucl-th/9811015.
- [Herrmann, 1997] Herrmann, N. (1997). Strangeness Production and Propagation in Relativistic Heavy Ion Collisions. In Petrovici, M., Sandulescu, A., Pelte, D., Stöcker, H., and Randrup, J., editors, *Heavy Ion Physics at Low, Intermediate and Relativistic Energies Using 4 $\pi$  Detectors, Poiana Brasov, Romania, October 7-14, 1996*, pages 332–345. World Scientific.
- [Herrmann et al., 1999] Herrmann, N., Wessels, J., and Wienold, T. (1999). Collective Flow in Heavy-Ion Collisions. *Ann. Rev. Nucl. Part. Sci.*, 49:581–632.
- [Hoffmann, 2001] Hoffmann, J. (2001). SAM3 module preliminary technical data. GSI Darmstadt.
- [Hong, 2001] Hong, B. (2001). Private communication. Comments to  $m_t$ -spectra of pions.

- [Hong et al., 1997] Hong, B., Herrmann, N., Ritman, J., Best, D., Gobbi, A., Hildenbrand, K., Kirejczyk, M., Leifels, Y., Pinkenburg, C., Reisdorf, W., Schüll, D., Sodan, U., Wang, G., Wienold, T., Alard, J., Amouroux, V., Bastid, N., Belyaev, I., Berek, G., Biegansky, J., Buta, A., Coffin, J., Crochet, P., Dona, R., Dupieux, P., Eskef, M., Fintz, P., Fodor, Z., Fraysse, L., Genoux-Lubain, A., Goebels, G., Guillaume, G., Häfele, E., Jundt, F., Kecskemeti, J., Korolija, M., Kotte, R., Kuhn, C., Lebedev, A., Legrand, I., Maazouzi, C., Manko, V., Mosner, J., Mohren, S., Neubert, W., Pelte, D., Petrovici, M., Pras, P., Rami, F., Roy, C., Seres, Z., Sikora, B., Simion, V., Siwek-Wilczyńska, K., Somov, A., Tizniti, L., Trzaska, M., Vasilev, M., Wagner, P., Wohlfarth, D., and Zhilin, A. (1997). Abundance of delta resonances in  $^{58}\text{Ni} + ^{58}\text{Ni}$  collisions between 1 AGeV and 2 AGeV. *Phys. Lett.*, B407:115–120. nucl-ex/9706001.
- [Hüfner and Weidenmüller, 1999] Hüfner, J. and Weidenmüller, H. (1999). 50 Years of the Nuclear Shell Model, Present state and future trends. International Conference, Heidelberg.
- [Karimaki, 1998] Karimaki, V. (1998). Explicit covariance matrix for particle measurement precision. *Nucl. Instrum. Meth.*, A410:284–292.
- [Köpfle, 2001] Köpfle, A. (2001). SSM Documentation 2.0. unpublished.
- [Kutsche, 2000] Kutsche, R. (2000). *Untersuchungen der In-Medium-Eigenschaften von  $K^0$ -Mesonen und  $\Lambda$ -Hyperonen an der Produktionsschwelle*. PhD thesis, Technische Universität Darmstadt.
- [Larionov et al., 2001] Larionov, A. B., Cassing, W., Leupold, S., and Mosel, U. (2001). Quenching of resonance production in heavy-ion collisions at 1 AGeV - 2 AGeV. *Nucl. Phys. A*, 696:747. nucl-th/0103019.
- [Laue et al., 1999] Laue, F., Sturm, C., Böttcher, I., Debowski, M., Forster, A., Grosse, E., Koczoń, P., Kohlmeyer, B., Mang, M., Naumann, L., Oeschler, H., Pühlhofer, F., Schwab, E., Senger, P., Shin, Y., Speer, J., Ströbele, H., Surowka, G., Uhlig, F., Wagner, A., and Walus, W. (1999). Medium effects in kaon and antikaon production in nuclear collisions at subthreshold beam energies. *Phys. Rev. Lett.*, 82:1640–1643. nucl-ex/9901005.
- [Li et al., 1998] Li, B.-A., Ko, C. M., and Bauer, W. (1998). Isospin Physics in Heavy-Ion Collisions at Intermediate Energies. *Int. J. Mod. Phys.*, E7:147–230.
- [Metag, 1997] Metag, V. (1997). Nucleus-Nucleus collisions in the SIS energy regime. Invited talk at 6th International Conference on Nucleus-Nucleus Collisions (NN 97), Gatlinburg USA, TN, 2-6 Jun 1997, GSI-preprint-97-43,1997.

- 
- [Nagamiya et al., 1981] Nagamiya, S., Lemaire, M., Möller, E., Shapiro, S. S. G., and Tanihata, H. S. I. (1981). Production of pions and light fragments at large angles in high-energy nuclear collisions. *Phys. Rev.*, C24:971–1009.
- [Neise et al., 1990] Neise, L., Berenguer, M., Hartnack, C., Peilert, G., Stöcker, H., and Greiner, W. (1990). Quantum molecular dynamics - A Model for Nucleus-Nucleus Collisions from medium to high Energies. *Nuclear Physics*, A519:375c–394c.
- [Pelte, 1998] Pelte, D. (1998). Production of pions in nucleon - nucleus and nucleus - nucleus reactions: The in-medium modification of the  $\Delta(1232)$  resonance. FOPI unpublished.
- [Pelte, 2001] Pelte, D. (2001). Private communication.
- [Pelte et al., 1997a] Pelte, D., Eskef, M., Goebels, G., Häfele, E., Herrmann, N., Korolija, M., Merlitz, H., Mohren, S., Trzaska, M., Alard, J., Amouroux, V., Andronic, A., Basrak, Z., Bastid, N., Belyaev, I., Best, D., Biegansky, J., Buta, A., Caplar, R., Cindro, N., Coffin, J., Crochet, P., Dupieux, P., Dzelalija, M., Ero, J., Fintz, P., Fodor, Z., Genoux-Lubain, A., Gobbi, A., Guillaume, G., Hildenbrand, K., Hong, B., Jundt, F., Kecskemeti, J., Kirejczyk, M., Koncz, P., Korchagin, Y., Kotte, R., Kuhn, C., Lambrecht, D., Lebedev, A., Legrand, I., Liefels, Y., Manko, V., Mosner, J., Moisa, D., Neubert, W., Petrovici, M., Pinkenburg, C., Pras, P., Rami, F., Ramillien, V., Reisdorf, W., Ritman, J., Roy, C., Schüll, D., Seres, Z., Sikora, B., Simion, V., Siwek-Wilczyńska, K., Smolyankin, V., Sodan, U., Vasilev, M., Wagner, P., Wang, G., Wienold, T., Wohlfarth, D., and Zhilin, A. (1997a). Charged pions from *Ni* on *Ni* collisions between 1 AGeV and 2 AGeV. *Z. Phys.*, A359:55–65. nucl-ex/9704009.
- [Pelte et al., 1997b] Pelte, D., Häfele, E., Best, D., Goebels, G., Herrmann, N., Pinkenburg, C., Reisdorf, W., Trzaska, M., Alard, J., Amouroux, V., Andronic, A., Basrak, Z., Bastid, N., Belyaev, I., Biegansky, J., Buta, A., Caplar, R., Cindro, N., Coffin, J., Crochet, P., Dupieux, P., Dzelalija, M., Ero, J., Eskef, M., Fintz, P., Fodor, Z., Genoux-Lubain, A., Gobbi, A., Guillaume, G., Hildenbrand, K., Hong, B., Jundt, F., Kecskemeti, J., Kirejczyk, M., Koncz, P., Korolija, M., Korchagin, Y., Kotte, R., Kuhn, C., Lambrecht, D., Lebedev, A., Legrand, I., Liefels, Y., Manko, V., Merlitz, H., Mosner, J., Mohren, S., Moisa, D., Neubert, W., Petrovici, M., Pras, P., Rami, F., Ramillien, V., Ritman, J., Roy, C., Schüll, D., Seres, Z., Sikora, B., Simion, V., Siwek-Wilczyńska, K., Smolyankin, V., Sodan, U., Vasilev, M., Wagner, P., Wang, G., Wienold, T., Wohlfarth, D., and Zhilin, A. (1997b). Charged pion production in *Au* on *Au* collisions at 1 AGeV. *Z. Phys.*, A357:215–234.

- [Reisdorf, 2001] Reisdorf, W. (2001). Private communication. Pion analysis.
- [Reisdorf and Ritter, 1997] Reisdorf, W. and Ritter, H. (1997). Collective Flow in Heavy-Ion Collisions. *Ann. Rev. Nucl. Part. Sci.*, 47:663–709.
- [Ritman, 1995] Ritman, J. (1995). The fopi detector at sis/gsi. *Nucl. Phys. Proc. Suppl.*, 44:708–715.
- [Ritman et al., 1995] Ritman, J., Herrmann, N., Best, D., Alard, J., Amouroux, V., Bastid, N., Belyaev, I., Berger, L., Biegansky, J., Buta, A., Caplar, R., Cindro, N., Coffin, J., Crochet, P., Dona, R., Dupieux, P., Dzelalija, M., Fintz, P., Fodor, Z., Genoux-Lubain, A., Gobbi, A., Goebels, G., Guillaume, G., Grigorian, Y., Häfele, E., Hildenbrand, K., Holbling, S., Jundt, F., Kecskemeti, J., Kirejczyk, M., Korchagin, Y., Kotte, R., Kuhn, C., Lambrecht, D., Lebedev, A., Lebedev, A., Legrand, I., Leifels, Y., Maazouzi, C., Manko, V., Matulewicz, T., Mosner, J., Mohren, S., Moisa, D., Neubert, W., Pelte, D., Petrovici, M., Pinkenburg, C., Rami, F., Ramillien, V., Reisdorf, W., Roy, C., Schüll, D., Seres, Z., Sikora, B., Simion, V., Siwek-Wilczyńska, K., Smolyankin, V., Sodan, U., Tizniti, L., Trzaska, M., Vasilev, M., Wagner, P., Wang, G., Wienold, T., Wohlfarth, D., and Zhilin, A. (1995). On the transverse momentum distribution of strange hadrons produced in relativistic heavy ion collisions. *Z. Phys.*, A352:355–357. nucl-ex/9506002.
- [Rutherford, 1911] Rutherford, E. (1911). The Scattering of  $a$  and  $b$  Particles by Matter and the Structure of the Atom. *Philosophical Magazine*, Series 6, vol. 21:669–688. <http://dbhs.wvusd.k12.ca.us/Chem-History/Rutherford-1911/Rutherford-1911.html>.
- [Schaffner et al., 1997] Schaffner, J., Bondorf, J., and Mishustin, I. (1997). In-medium kaon production at the mean-field level. *Nucl. Phys.*, A625:325–346. nucl-th/9607058.
- [Schwalb et al., 1994] Schwalb, O., Pfeiffer, M., Berg, F., Franke, M., Kuhn, W., Metag, V., Notheisen, M., Novotny, R., Ritman, J., Roebig-Landau, M., Alard, J., Bastid, N., Brummund, N., Dupieux, P., Gobbi, A., Herrmann, N., Hildenbrand, K., Hlavac, S., Jeong, S., Loehner, H., Montarou, G., Neubert, W., Raschke, A., Simon, R., Sodan, U., Sumbera, M., Teh, K., Venema, L., Wilschut, H., Wessels, J., Wienold, T., and Wohlfahrt, D. (1994). Mass dependence of  $\pi^0$  production in heavy ion collisions at 1 AGeV. *Phys. Lett.*, B321:20–25.
- [Senger and Stroebele, 1999] Senger, P. and Stroebele, H. (1999). Hadronic particle production in nucleus-nucleus collisions. *J. Phys.*, G25:R59–R131. nucl-ex/9810007.

- 
- [Stock, 1986] Stock, R. (1986). Particle production in high energy nucleus-nucleus collisions. *Physics Reports*, 135(5):259–315.
- [Stöcker and Greiner, 1986] Stöcker, H. and Greiner, W. (1986). High-energy heavy ion collisions: Probing the equation of state of highly excited hadronic matter. *Phys. Rept.*, 137:277–392.
- [Stockmeier, 1996] Stockmeier, M. (1996). Phidoo, eine Testkammer für FOPI. Master's thesis, Universität Heidelberg.
- [FOPI Collaboration, 2001] FOPI Collaboration, T. (2001).  $\Xi^-$  Measurements with FOPI. P. Crochet for the FOPI Collaboration at the 24th Meeting of the Experimentausschuß.
- [von Weizsäcker, 1935] von Weizsäcker, C. (1935). *Z. Phys.*, 96:431.
- [Wiśniewski, 2000] Wiśniewski, K. (2000). *Kaon and Antikaon production in Heavy-Ion Collisions for the Reactions Ru + Ru and Ru + Zr at 1.69 AGeV beam kinetic energy*. PhD thesis, Uniwersytet Warszawski.
- [Wiśniewski et al., 2000] Wiśniewski, K., Crochet, P., Herrmann, N., Andronic, A., Auerbeck, R., Devismes, A., Finck, C., Gobbi, A., Hartmann, O., Hildenbrand, K., Koczon, P., Kress, T., Kutsche, R., Leifels, Y., Reisdorf, W., Schüll, D., Alard, J., Barret, V., Basrak, Z., Bastid, N., Belyaev, I., Bendarag, A., Berek, G., Caplar, R., Cindro, N., Dupieux, P., Dzelalija, M., Eskef, M., Fodor, Z., Grishkin, Y., Hong, B., Kecskemeti, J., Kim, Y., Kirejczyk, M., Korolija, M., Kotte, R., Kowalczyk, M., Lebedev, A., Lee, K., Manko, V., Merlitz, H., Mohren, S., Moisa, D., Neubert, W., Nianine, A., Pelte, D., Petrovici, M., Pletner, C., Rami, F., de Schauenburg, B., Seres, Z., Sikora, B., Sim, K., Simion, V., Siwek-Wilczyńska, K., Smolyankin, V., Somov, A., Stockmeier, M., Stoicea, G., Vasilev, M., Wagner, P., Wohlfarth, D., Yang, J., Yushmanov, I., and Zhilin, A. (2000). Direct comparison of phase-space distributions of  $K^-$  and  $K^+$  mesons in heavy-ion collisions at SIS energies: Evidence for in-medium modifications of kaons? *Eur. Phys. J.*, A9:515–519. nucl-ex/0101009.



# Danksagung

An dieser Stelle möchte ich meinen herzlichen Dank an alle ausdrücken, die zum Gelingen dieser Arbeit beigetragen haben. Zuerst meinem Betreuer Prof. Dr. N. Herrmann für dessen ständige Diskussionsbereitschaft und hervorragende Betreuung. Den Herren Prof. Dr. D. Pelte und Dr. W. Reisdorf danke ich für intensive und fruchtbare „Pionendiskussionen“. Frau Dr. Y. Leifels danke ich für die vielen Diskussionen, GEANT und die Computerei betreffend, und für ihr Interesse an den Pionen.

Mein Dank gilt auch der kleinen, aber feinen Arbeitsgruppe in Heidelberg, die aus den Herren M. Merschmeyer, K. Wiśniewski und neuerdings N. Otte besteht. Herr Wiśniewski mußte auch Teile der Arbeit korrekturlesen – vielen Dank dafür. Dem nächsten Spieleabend steht nun nichts mehr im Wege.

Meine Aufenthalte am KFKI Budapest wurden durch die gute Zusammenarbeit mit unseren ungarischen Kollaborationsmitglieder J. Kecskemeti, Z. Seres und Z. Fodor sehr angenehm.

Auch den „GSI'lern“ möchte ich meinen Dank aussprechen. A. Andronic, A. Devismes, T. Kress, O.N. Hartmann, K.D. Hildenbrand und vor allem Herrn A. Gobbi. Eine Entschuldigung an alle, die ich nicht namentlich aufliste. Auch allen Mitgliedern der **FOPI** Kollaboration sei für die hervorragende Zusammenarbeit gedankt.

Nicht zu vergessen meine Leidensgenossen H. Tilsner, J. Slivova und W. Schmitz.

„Mein“ Zimmer am Physikalischen Institut, das durch Fluktuationen von Staatsexamens- und Diplomkandidaten sich immer neu formierte, beherbergte außerdem L. Dietrich, I. Weimann, S. Wende und R. Özel.

Frau Prof. Dr. J. Stachel danke ich für die Übernahme der Zweitkorrektur und den Herren Prof. Dr. J. Hüfner und Prof. Dr. V. Lindenstruth für die Übernahme der Prüfungsteile Theoretische Physik und Hardwareinformatik.

Mein besonderer Dank gilt meiner Frau Silke, die es geschafft hat, mich vor allem in der Endphase zu ertragen und meinen beiden Kindern Lea und Jan, die sich manchmal schon wunderten, von was der Papa nun schon wieder erzählt. Ohne die Unterstützung meiner Familie wäre die Fertigstellung dieser Arbeit nicht möglich gewesen. Auch meinen Eltern möchte ich an dieser Stelle danken.

